UNIVERSITY OF CALIFORNIA
RIVERSIDE

# Synthesis and Characterization of One-, Two- and Three-Dimensional Chalcogenide Nanostructures

A Dissertation submitted in partial satisfaction
of the requirements for the degree of

Doctor of Philosophy

in

Chemical and Environmental Engineering

by

Hyunsung Jung

August 2011

Dissertation Committee:
Dr. Nosang V. Myung, Chairperson
Dr. Robert Haddon
Dr. Christopher Dames

The Dissertation of Hyunsung Jung is approved:

_____

_____

_____

Committee Chairperson

University of California, Riverside

## Acknowledgements

I would like to express my gratitude to all those who gave me the possibility to complete this thesis.

ABSTRACT OF THE DISSERTATION

Synthesis and Characterization of One-, Two- and Three-Dimensional Chalcogenide Nanostructures

by

Hyunsung Jung

Doctor of Philosophy, Graduate Program in Chemical and Environmental Engineering
University of California, Riverside, August 2011
Dr. Nosang V. Myung, Chairperson

The paramount issues of today such as the gathering energy crisis and rise in levels of pollution have largely resulted from our increasingly accelerated industrialization due to technology developments. Ironically, those issues demand the further advanced technology to answer. In addition, the overwhelming rate of data production due to the rapid development of computer technologies require even more improved technologies to overcome our current limits. Nanotechnology has been extensively developed to approach these issues, since engineered materials at the nano-scale level have demonstrated enhanced desirable properties due to their small dimensions. Chalcogenide nanostructures have shown potential for use in thermoelectric and phase change memory devices with potentially high performance.

The overall objective of this work is to engineer nanostructured chalcogenides using various techniques such as electrodeposition and wet-chemical synthesis as cost-effective and simple approaches. The dimension, size, composition and crystal structure

of the chalcogenide materials are controlled to enhance their properties for thermoelectric and phase change memory applications.

The specific research investigations in this work were the following:

1) Electrochemical analysis of $Sb_xTe_{1-x}$ electrodeposits was implemented. Linear sweep voltammetry and quartz crystal microbalance techniques were utilized to study the properties of $Sb_xTe_{1-x}$ depending on agitation and temperature. The mass transport, reduction behavior, surface morphology and crystal structure of $Sb_xTe_{1-x}$ electrodeposits were investigated.
2) $Sb_xTe_{1-x}$ nanocomposites were produced by the separation of the $Sb_2Te_3$ phase and the γ-SbTe phase in the annealed $Sb_xTe_{1-x}$ electrodeposits. The thermoelectric and phase transition properties of $Sb_xTe_{1-x}$ electrodeposits were characterized as a function of temperature and composition. The generated nanocomposites demonstrated a drastically enhanced Seebeck coefficient.
3) $Ag_xTe_{1-x}$ thin films were synthesized by a topochemical transformation reaction of thermally evaporated Te thin films. The thermoelectric properties of the transformed $Ag_xTe_{1-x}$ thin films with tailored compositions were analyzed. In addition, the composition-dependent Seebeck coefficients showed the transition of carrier transport behavior from p-type to n-type.
4) Ternary chalcogenide $Ag_xSb_{1-x}Te_y$ materials were synthesized by a cost-effective and simple cation exchange reaction of thermally evaporated $Sb_xTe_y$ thin films. The composition of ternary $Ag_xSb_{1-x}Te_y$ was controlled by the

reaction time. Temperature- and composition-dependent thermoelectric and phase transition properties of the synthesized films were investigated.

5) Single crystal PbTe nanowires were electrodeposited by a template-direct method. An electrical transport behavior of the electrodeposited PbTe nanowires with modulated electrical contacts was estimated. The improvement of the electrical contact was achieved by a galvanic displacement reaction of Au nanoparticles with PbTe exposed in the opened contact region.
6) Scalable Te nanoribbons with Au electrodes were fabricated by a lithographically patterned nanowire electrodeposition (LPNE) technique. A pulsed potential was applied to control the reduced width of nanoribbons. The dimensions of the nanoribbons were determined by a pattern design, the thickness of e-beam evaporated Ni layer and an electrodeposition time. Ultra-long Te nanoribbons with a length of several cm, a height of 100 nm and a ranged width from about 50 to 200 nm were demonstrated. Electrical properties of Te nanoribbons with different widths were studied. Moreover, the effect of the size of the nanoribbons and the electrical contact types on the $NH_3$ sensing properties of Te nanoribbons on $NH_3$ (g) was analyzed.
7) A combined technique of a LPNE and a galvanic displacement reaction was utilized to synthesize ultra-long $Bi_xTe_{1-x}$ nanoribbons of which the dimensions were controlled in a length of several cm, a height of 100 nm and a ranged width from about 400 nm to 2.5 μm. Composition-dependent

electrical resistivities and FET properties of the $Bi_xTe_{1-x}$ nanoribbons were analyzed. Temperature-dependent thermoelectric properties of a $Bi_{31}Te_{69}$ nanoribbon were investigated.

In this dissertation, antimony telluride ($Sb_xTe_{1-x}$), bismuth telluride ($Bi_xTe_{1-x}$), lead telluride ($Pb_xTe_{1-x}$), tellurium (Te), silver telluride ($Ag_xTe_{1-x}$), silver antimony telluride ($Ag_xSb_{1-x}Te_y$) were synthesized by various techniques such as potentiostatic deposition, pulse plating, topochemical transformation reaction, cation exchange reaction and galvanic displacement reaction. The material properties and electrical/thermoelectric behaviors depending on their dimension, size, composition and crystal structure were investigated.

## TABLE OF CONTENTS

## LIST OF FIGURES

## LIST OF TABLES

# CHAPTER 1

# Introduction: Nanostructured Thermoelectric and Phase Change Memory Devices

## 1.1 Nanostructured Thermoelectrics

### 1.1.1 An Overview of Thermoelectrics

The impending energy crisis has been an increasingly serious issue with the currently accelerated rates of industrialization and economic growth, since the amount of buried fossil fuels has been predicted to be exhausted in the near future [1]. Since approximately 80 % of all energy consumption in the world has been dependent of the supply of fossil fuels, the need for the development of alternative energy resources has been increasing. Among various energy technologies such as solar cells, biomasses and fuel cells, thermoelectrics is one of the potential energy technologies, which is most able to be employed in current industrial infrastructure.

The thermoelectric effects of materials can be described by the combination of Seebeck effects and Peltier effects [2]. The Seebeck effect of thermoelectric materials represents a voltage ($V_{hc}$) generation between each end of the material with temperature gradients ($\Delta T_{hc}$), where the Seebeck voltage is developed by the flow of charge carriers from a hot side to a cold side. Conversely, the temperature gradient can be generated by the applied voltage between each end of a thermoelectric material, which is defined as Peltier effects. Based on Seebeck and Peltier effects, thermoelectric materials can generate voltage between each end of the material due to temperature gradients and vice

versa. The thermoelectric effects can be evaluated by thermoelectric figure-of-merit (ZT) as described in Equation 1.1 [2].

$$ZT = \frac{S^2\sigma}{\kappa}T \qquad \text{Equation 1.1}$$

where S (μV/K), σ (S/m), κ (W/mK) and T (K) are the Seebeck coefficient, electrical conductivity, thermal conductivity and absolute temperature, respectively. The thermal conductivity consists of both thermal conductivities of electrons and phonons ($\kappa=\kappa_e+\kappa_{ph}$). The thermoelectric devices can be utilized as a thermoelectric power generator and as a thermoelectric cooler (Figure 1.1) [2, 3]. The unit cell of a thermoelectric device consists of p-type and n-type semiconductor legs between a hot and a cold junction. As shown in the power generator and the cooler of Figure 1.1, the hole carriers in a p-type semiconductor and the electron carriers in a n-type semiconductor flow from hot junction to cold junction.

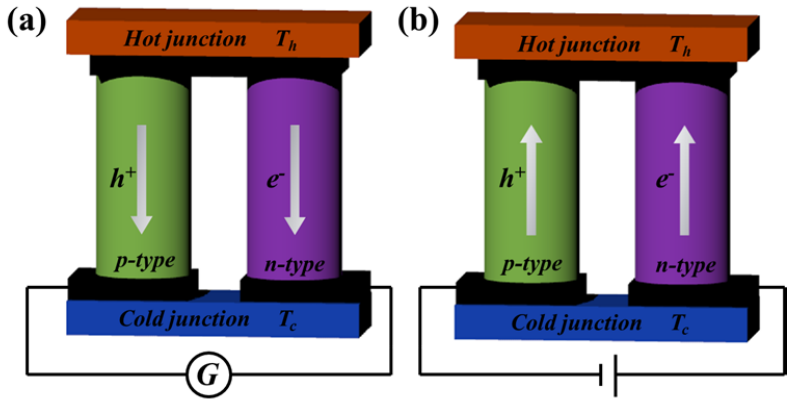


**Figure 1.1**: A schematic diagram of a p-n junctioned unit cell of thermoelectric devices: thermoelectric power generator (a) and thermoelectric cooler (b). The unit cell of thermoelectric devices consists of p-type and n-type semiconducting legs connected electrically with a metal conductor.

The thermoelectric devices consist of the p-n junctioned unit legs connected electrically in series to enhance the thermoelectric effects (i.e. higher current output and larger temperature gradient) (Figure 1.2), since one p-n junctioned thermoelectric unit cell can demonstrate a Seebeck voltage on the order of only microvolt per Kelvin [3]. The degree of the generated electrical current and the temperature gradient in the thermoelectric devices can be determined by thermoelectric figure-of-merit of the thermoelectric materials and the number of thermoelectric unit cells.

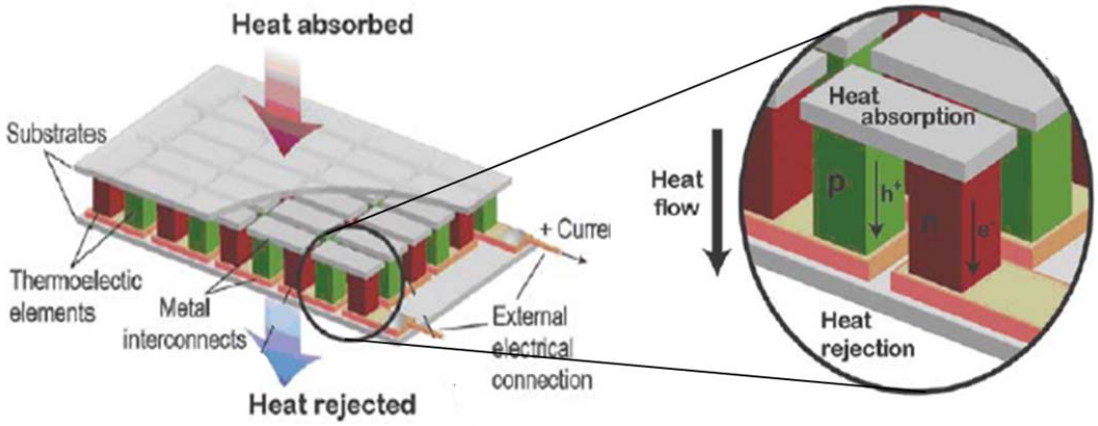


**Figure 1.2**: A schematic diagram of thermoelectric device with p-n junctioned unit legs connected electrically in series [3].

The thermoelectric devices are environmentally friendly solid state devices with zero-emissions. Additionally, a vast scalability and long operating times of thermoelectric devices can be demonstrated, with minimal to no noise pollution and maintenance requirements. Because of their many advantages, solid state thermoelectric devices can be applied in various fields as illustrated in Figure 1.3 [4]. Thermoelectric devices were particularly utilized in space exploration missions (Apollo, Pioneer, Voyager, etc) due to

their key advantages of long operation times and no maintenance [5]. Over 25 years since its launch, Voyager is still operating with assistance from a thermoelectric device which can generate electricity from a radioisotope as a heat source. Moreover, thermoelectric devices have been implemented in military and medical applications, such as a cooler of a personnel garment, an infrared sensor, and diagnostic medical equipment. Additionally, various commercial applications (i.e. integrated circuit coolers and portable refrigerators) have been suggested. Thermoelectric wristwatches have been recently produced, driven by body heat converted into the required electrical power [4]. One of attractive future applications of thermoelectric devices is the harvest of the waste heat from the heat engines of automobiles, since they often have demonstrated an efficiency of less than 30 % [4]. The application of thermoelectric devices to automobile engines can play an important role in mitigating the impact of the current environmental and energy issues.

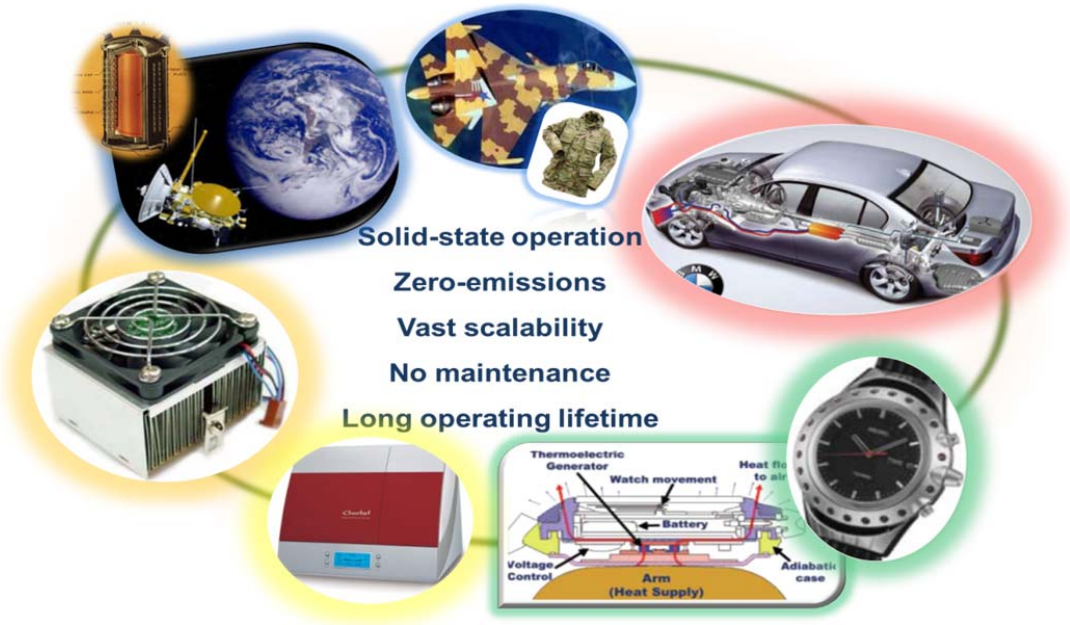


**Figure 1.3**: Applications of thermoelectric devices in various commercial fields [4].

### 1.1.2 Thermoelectric Materials

Thermoelectric materials need to have a high Seebeck coefficient, a high electrical conductivity and a low thermal conductivity to achieve a high thermoelectric figure-of-merit. The achievement of a high thermoelectric figure-of-merit has been restricted by the interdependency of those three parameters (S, σ and κ). The thermal conductivity of a material inversely depends on the electrical properties as described in the Wiedemann-Franz law, as seen in Equation 1.2:

$$\frac{\kappa_e}{\sigma} = LT \qquad \text{Equation 1.2}$$

where L, known as the Lorenz number, is a constant of $2.44 \times 10^{-8}$ $W\Omega/K^2$ for free electrons of a metal and $\kappa_e$ is the thermal conductivity of electron carriers. The Wiedermann-Franz law indicates that the electrical conductivity of a metal is strongly coupled with the thermal conductivity. The optimum thermoelectric material can be determined by a comparison of S, σ and κ depending on the carrier concentration of the material as shown in Figure 1.4, since the Lorenz constant varies with the carrier concentration of the material [3]. The electrical conductivity increases with an increase in carrier concentration, while the Seebeck coefficient decreases, displaying the largest thermoelectric power factor ($S^2\sigma$) at a carrier concentration of around $10^{20}$ $cm^{-3}$. The thermal conductivity also increases with an increase in carrier concentration, consequently, resulting in a maximum thermoelectric figure-of-merit at a carrier concentration of about $4 \times 10^{19}$ $cm^{-3}$. The thermoelectric figure-of-merit can achieve a maximum at lower carrier concentration than the thermoelectric power factor. Figure 1.4 shows that highly doped semiconductors or semiconductors with a narrow band gap

demonstrates high thermoelectric figure-of-merits, based on superior electrical conductivities and Seebeck coefficients, and the poor thermal conductivities of these materials.

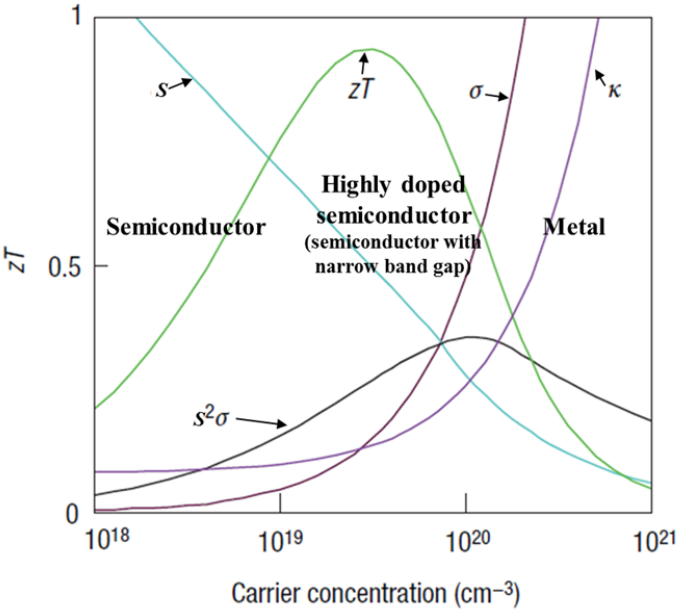


**Figure 1.4**: Optimization of carrier concentration-dependent thermoelectric figure-of-merit (ZT), based on Seebeck coefficient (S), electrical conductivity (σ) and thermal conductivity (κ), varied by the carrier concentration of material [3].

According to theoretical studies, various highly doped semiconductors and narrow band gaped semiconductors have been investigated to create optimum thermoelectric materials. Among various semiconducting materials, chalcogenides with a narrow energy band gap have demonstrated the desired thermoelectric figure-of-merit as shown in Figure 1.5 [2, 3]. Antimony telluride ($Sb_2Te_3$) as a p-type semiconducting material and bismuth telluride ($Bi_2Te_3$) as an n-type semiconducting material have been widely used, because the chalcogenide materials possessed a high thermoelectric figure-of-merit at

near room temperatures. Among various chalcogenide thermoelectric materials with tailored compositions, by far p-type $(Sb_{0.8}Bi_{0.2})_2Te_3$ and n-type $Bi_2(Te_{0.8}Se_{0.2})_3$ bulk alloys of $Bi_2Te_3$ have demonstrated the highest thermoelectric figure-of-merit at near room temperature. The thermoelectric performance of a material can be improved by tuning the composition to achieve an optimum thermoelectric material.

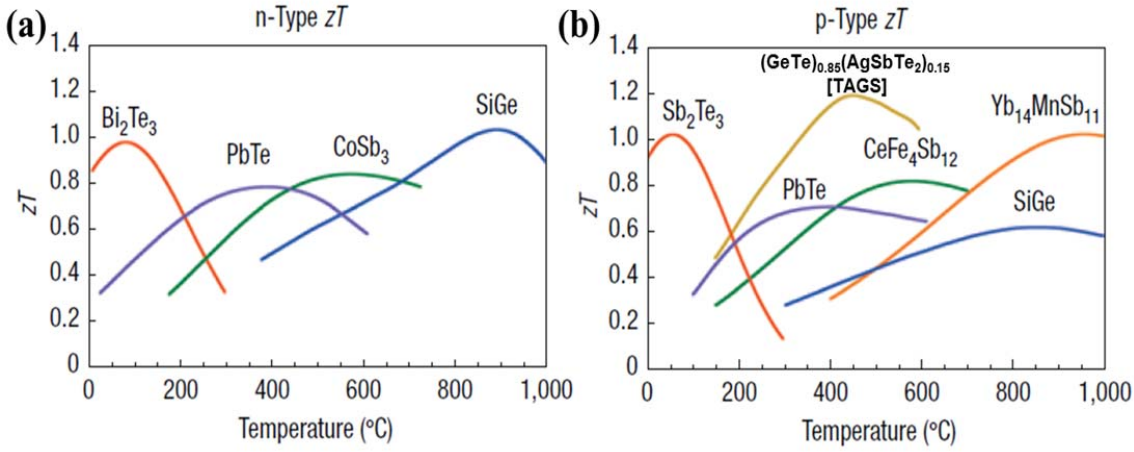


**Figure 1.5**: Thermoelectric performance (figure-of-merit, ZT) of estabilished thermoelectric materials as a function of temperature [2, 3]: n-type materials (a) and p-type materials (b).

### 1.1.3 Fundamental Physics for the Improvement of the Thermoelectric Figure-of-Merit

Despite the critical advantages and various applications of thermoelectric devices, the development of thermoelectric materials had been stagnant with a thermoelectric figure-of-merit value of around 1 for several decades, which had been demonstrated by the bulk thermoelectric chalcogenide materials. The interdependece of the key parameters, -the Seebeck coefficient, the electrical and thermal conductivities-, had impeded the

development of thermoelectrics. However, the research of thermoelectric materials was reinvigorated by the current advance of nanotechnologies as shown in Figure 1.6 [6-10].

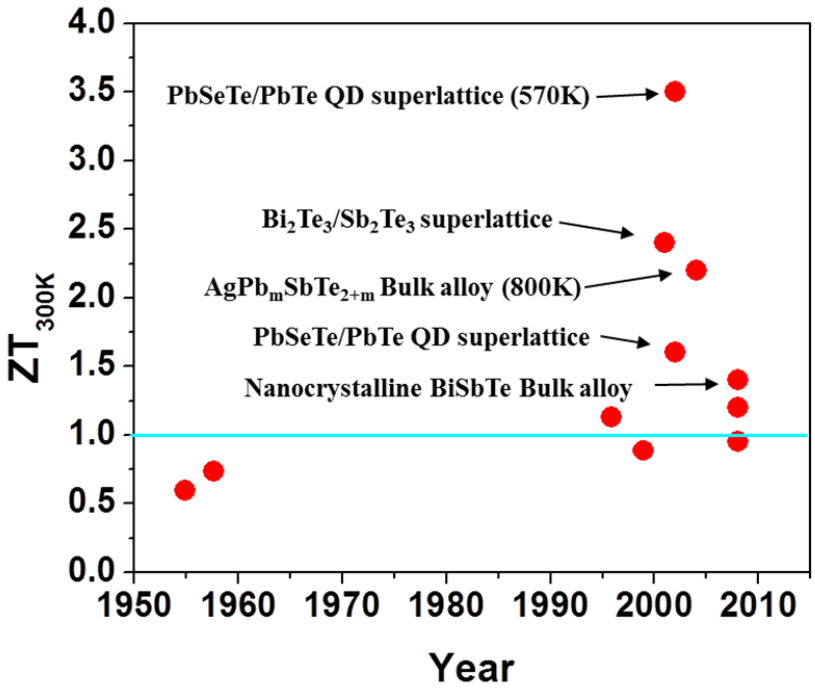


**Figure 1.6**: History of thermoelectric figure-of-merit (ZT), where ZTs were the properties at 300K, except the ZT of $AgPb_mSbTe_{2+m}$ bulk alloys and PbSeTe/PbTe quantum dot superlattices at 800K and 570 K, respectively [6-10].

The enhancement of the thermoelectric figure-of-merit from nanostructured thermoelectric materials can be attributed to the decoupling of the key thermoelectric parameters (S, σ and κ), which can be characterized by following physics:

1) Reduction of the thermal conductivity decoupled with the electrical conductivity and Seebeck coefficient

2) Increase of the electrical conductivity decoupled with the thermal conductivity and Seebeck coefficient
3) Increase of the Seebeck coefficient decoupled with the electrical conductivity and thermal conductivity

The thermal transport can be determined by both the electronic thermal transport due to electrons (or holes) carriers and a lattice thermal transport due to phonons (a quantized lattice vibration). The phonon contribution to the thermal conductivity will be primarily to reduce the thermal conductivity of thermoelectric materials, because the electronic thermal conductivity is restricted by Wiedemann-Franz law. The phonon thermal conductivity can be described by Equation 1.3.

$$\kappa_{ph} = \sum_j \int C_j(\omega) \nu_j^2(\omega) \tau_j(\omega) dx \qquad \text{Equation 1.3}$$

where j is the phonon branches (transverse and longitudinal), C is the heat capacity, ω is the phonon angular velocity, ν is the phonon velocity, τ is a phonon relaxation time, and $x$ is a dimensionless phonon angular frequency ($\hbar\omega/k_BT$), respectively. Among the parameters, the phonon relaxation time is dependent on the size of the material, which can be described by a phonon mean free path ($l$) as shown in Equation 1.4.

$$l = \tau\nu \qquad \text{Equation 1.4}$$

The phonon mean free path can be determined by various scattering factors such as other phonons, electrons, impurities and boundaries. An Umklapp process (phonon-phonon scattering) is a dominant factor in limiting the phonon mean free path of bulk materials at near room temperatures. As a dimension of a material is reduced to a value smaller than

that of the mean free path, the mean free path is limited by other scattering factors, not phonon-phonon scattering. Consequently, the thermal conductivity of materials with decreased dimensions can be lowered by the reduced effective phonon mean free path, which is typically referred to as a classical size effect. The impact of surface boundaries and grain boundaries as dominant scattering factors for the reduction of the thermal conductivity have been investigated [11-13]. The reduction of the thermal conductivity without decreasing the electrical conductivity can be potentially achieved by the reduction of the effective phonon mean free path without decreasing an effective electron mean free path. For decoupling a thermal conductivity with the electrical conductivity, nanostructured thermoelectric materials will be engineered with dimensions smaller than the phonon mean free path and larger than the electron (or hole) mean free path. Additionally, the effective mean free path of phonons can be reduced by a phonon confinement in free standing or embedded thermoelectric materials due to increased scattering [7-9, 14-16].

Improved electrical performance in various electrical circuits has also been a key issue. High electrical conductivity, decoupled with thermal conductivity, has also been an aim to enhance the thermoelectric figure-of-merit in thermoelectric devices. The material properties can be tailored by controlling the size of the materials. Materials with a size comparable with the Bohr radius can demonstrate drastically enhanced electrical properties unlike bulk materials, which is known as a quantum size effect [17, 18]. The variation of electrical properties in nano-scaled materials is achieved by sharp edges and

peaks in a quantized density of electronic states with respect to a Fermi energy level as shown in Figure 1.7 [19].

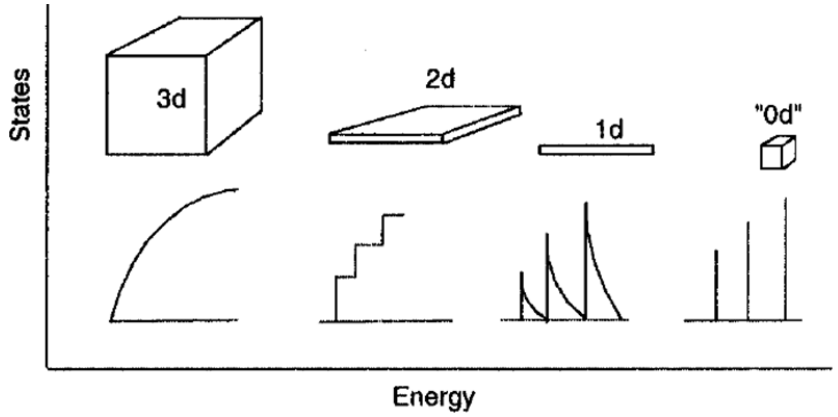


**Figure 1.7**: Density of states of semiconductors with 3-, 2-, 1-, and 0-dimensional structures.

Based on the Drude-Sommerfeld model of electrical conduction, the electrical conductivity is described in Equation 1.5, where n, e and μ are the charge carrier density, carrier charge and electronic mobility, respectively [20]. The electrical conductivity can be defined in terms of relaxation time and effective mass, or by using the degeneracy factor (g), Fermi wave vector ($k_F$) and mean free path ($l$). Consequently, the electrical conductivity can be increased by the modified Fermi energy in the materials with quantized dimensions.

$$\sigma = ne\mu = ne^2 \frac{\tau}{m^*} = g\left(\frac{e^2}{h}\frac{k_F}{3\pi}\right)k_F l \qquad \text{Equation 1.5}$$

Furthermore, the Seebeck coefficient of thermoelectric materials can be tuned by the transformed density of states in the quantized dimensions [21]. The Seebeck coefficient of a degenerated semiconductor is defined in Equation 1.6.

$$S = \frac{8\pi^2 k_B^2 T}{3eh^2} m^* \left(\frac{\pi}{3n}\right)^{2/3} \qquad with \quad g(E) = \frac{\left(m^*\right)^{3/2}\sqrt{2E}}{\hbar^3 \pi^2} \qquad \text{Equation 1.6}$$

where g(E) is a density of state as a function of energy (E).

However, the increase of a thermoelectric figure of merit is typically more dependent on a decrease in the thermal conductivity without deteriorating the electrical properties, and less dependent on an increase in the electrical properties due to quantum confinement. Although both approaches are possible, the fabrication of the thermoelectric devices with a reduced size for quantum confinement is limited. A new wave of the improvement in thermoelectric properties has resulted in a drastic increase of Seebeck coefficients decoupled with electrical conductivity, which has been investigated in engineered heterostructures which can be supported by a charge carrier filtering technique [22-24]. In the case of heterostructures with a thick energy barrier, a thermionic emission of charge carriers over the barrier is limited. Consequently, only charge carriers with high energies can contribute to the electrical conduction due to the filtering of low energy carriers, resulting in enhanced Seebeck coefficients.

### 1.1.4 Nanostructured Thermoelectric Materials

#### 1.1.4.1 Three Dimensional Nanocomposites and Nanocrystalline Bulks

The development of bulk thermoelectric devices is critical for large-scale commercial use, because of the requirement of cost-effective and mass-producible processes. However, bulk thermoelectric materials have shown low thermoelectric properties due to the restriction of the coupled thermoelectric parameters, even though

the performance of thermoelectric bulk materials has been classically developed by the use of heavy elemental compounds of large atomic masses with low sound velocity and highly doped materials for the increased phonon scattering in point defects. Nowadays, enhanced thermoelectric figure-of-merits in bulk thermoelectric materials have been demonstrated by thermoelectric nanocomposites and nanocrystalline bulks [7, 9, 22, 23, 25-29]. The 3-dimensional thermoelectric bulk materials with high thermoelectric figure-of-merits were nanocomposites and nanocrystalline bulk with nanostructures (i.e. nanoparticles and grains) embedded in a host material or heterogeneous nanocomposites with nanoparticles embedded in the matrix of different materials. The enhancement of thermoelectric figure-of-merits in the nanocomposites was mainly achieved by the reducing the part of the thermal conductivity due to increased phonon scatterings in the interface as shown in Figure 1.8 [9], where nanocrystalline bismuth antimony telluride bulk alloys were synthesized by ball milling in an inert gas followed by a hot pressing process.

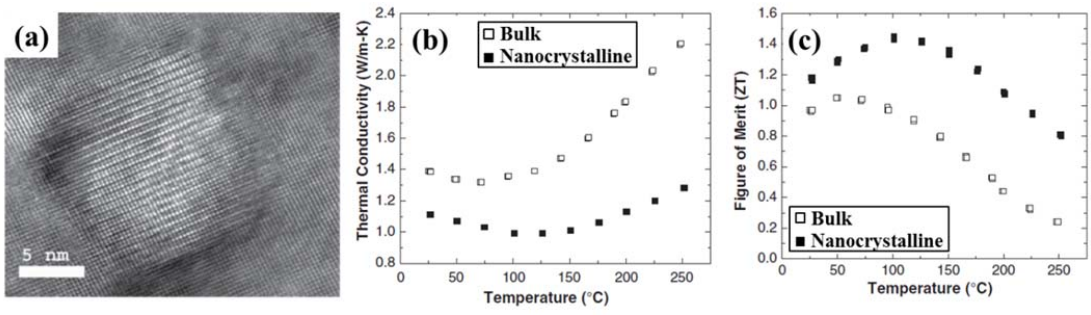


**Figure 1.8**: High resolution TEM image of nanocrystalline bismuth antimony telluride bulk alloys (a), temperature dependent thermal conductivity (b) and temperature dependent thermoelectric figure-of-merit (c) of bulk single crystal and nanocrystalline materials [9].

The thermal conductivity of the nanocrystalline material was reduced by increased phonon scattering at the interface, resulting in an increase in the thermoelectric figure-of-merits. In addition to the improvement of the thermoelectric properties due to the phonon contributor, enhanced Seebeck coefficients in the nanocomposites were reported, which was described by an electrical charge filtering technique.

### 1.1.4.2 Two Dimensional Superlattice Thin Films

The enhancement of the thermoelectric properties in low dimensional materials had been theoretically expected by an increased Seebeck coefficient due to a quantum confinement and a reduced thermal conductivity due to the increased phonon scattering, which was first demonstrated by 2-dimensional quantum well systems. The highest thermoelectric figure-of-merit of 2.4 at 300 K was achieved by 2-dimensional $Bi_2Te_3/Sb_2Te_3$ superlattices as shown in Figure 1.9 [8, 30, 31].

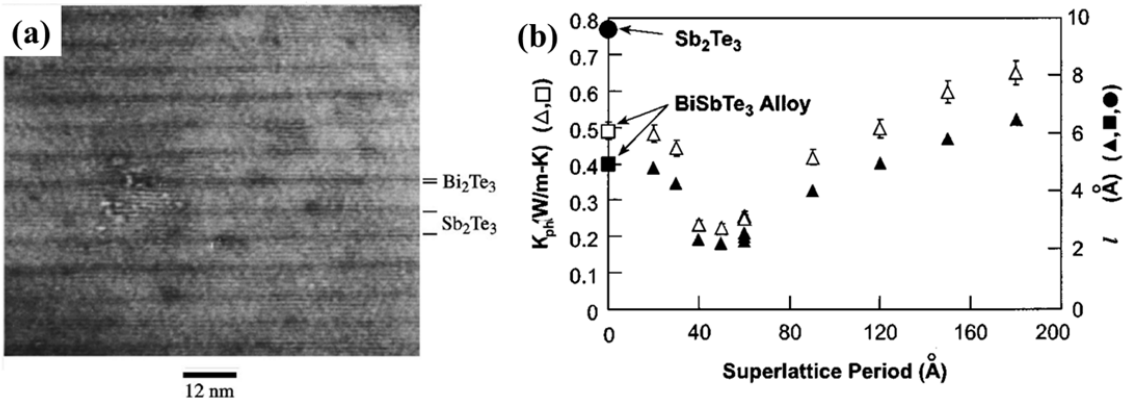


**Figure 1.9**: TEM image of a 10 Å/50 Å $Bi_2Te_3/Sb_2Te_3$ superlattice (a) and measured phonon thermal conductivity ($\kappa_{ph}$) of the superlattice and calculated average phonon mean free path ($l$) as a function of the period in the $Bi_2Te_3/Sb_2Te_3$ superlattice (b) [8, 30, 31]

The p-type $Bi_2Te_3/Sb_2Te_3$ superlattices were deposited by a metal-organic chemical vapor deposition (MOCVD) technique. The thermal conductivity of $Bi_2Te_3/Sb_2Te_3$ superlattices could be reduced by the increased phonon scatterings at the interfaces of alternating layers of $Bi_2Te_3$ and $Sb_2Te_3$ with the thicknesses of several nanometers, which thus demonstrated a greater enhancement of the thermoelectric figure-of-merits than the enhancement achieved by increaseing Seebeck coefficients.

Another proof-of-principle that a low dimensional thermoelectric system could show the improved performance was a 2-dimensional quantum dot superlattice of PbSeTe/PbTe on top of a $BaF_2$ substrate followed by a PbTe buffer layer, which demonstrated a thermoelectric figure-of-merit of 1.6 at 300 K and of 3.5 at 570 K as shown in Figure 1.10 [10, 32, 33].

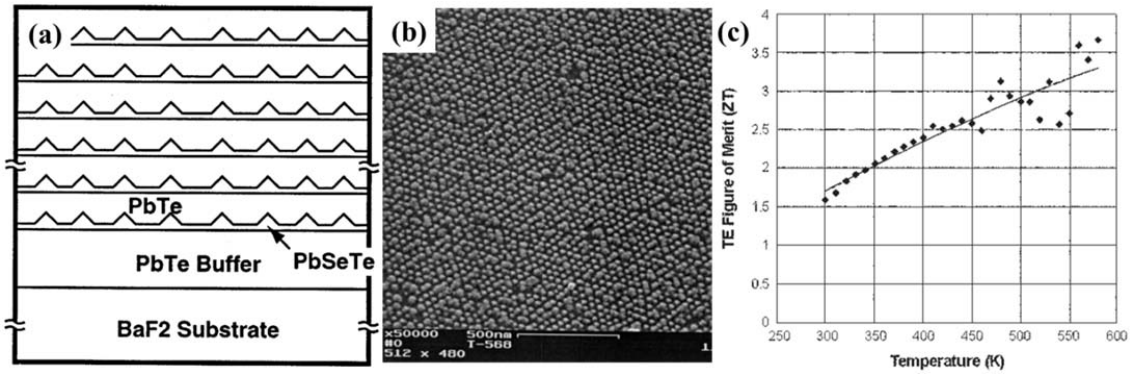


**Figure 1.10**: Schematic diagram (a), SEM image (b) and temperature dependent thermoelectric figure-of-merit (c) of a PbSeTe/PbTe quantum dot superlattice system.

The PbSeTe/PbTe superlattices were prepared by a molecular beam epitaxy (MBE) technique and the quantum dots in the matrix were generated by the lattice mismatch between PbTe and PbSe. The remarkable enhancement of figure-of-merits in the system

was achieved by both an increased thermoelectric power factor ($S^2\sigma$) and decreased thermal conductivity ($\kappa$).

#### 1.1.4.3 One-Dimensional Nanostructures

One dimensional nanostructures are attractive for many applications, since they can function as both devices and the wires that access them. Especially, 1-dimensional thermoelectric nanostructures can possess superior properties over the bulk and the 2-dimensional superlattice as theoretically predicted by Hicks et al [17]. Figure 1.11 shows the calculated thermoelectric figure-of-merits of 1-dimensional $Bi_2Te_3$ nanowires as a function of a diameter, where the x, y and z directions are based on anisotropic properties of $Bi_2Te_3$. The drastically enhanced figure-of-merit of a $Bi_2Te_3$ nanowire with a diameter smaller than 20 Å is predicted by both the increase of the thermoelectric power factor due to a quantum confinement of charge carriers and the decrease of the thermal conductivity due to increased surface scattering.

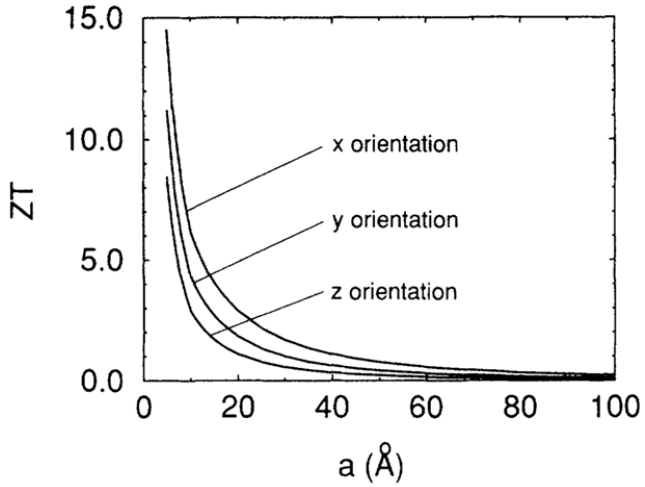


**Figure 1.11**: Thermoelectric figure-of-merits (ZT) of 1-dimensional $Bi_2Te_3$ nanowires fabricated along the x, y and z directions as a function of diameters.

The experimental proof-of-principle of the enhanced thermoelectric properties in 1-dimensional nanostructures was demonstrated by Si nanowires with surface morphologies, varied sizes and doping levels [11, 12]. Figure 1.12 shows the thermal conductivity and thermoelectric figure-of-merits of an arrayed single crystal Si nanowire depending on size and carrier concentrations varied by doping levels as a function of temperature, where boron-doped single crystal Si nanowires were prepared by the superlattice nanowire pattern transfer method [12]. The enhancement of the thermoelectric figure-of-merits resulted from the reduction of the thermal conductivity accompanied by size reduction.

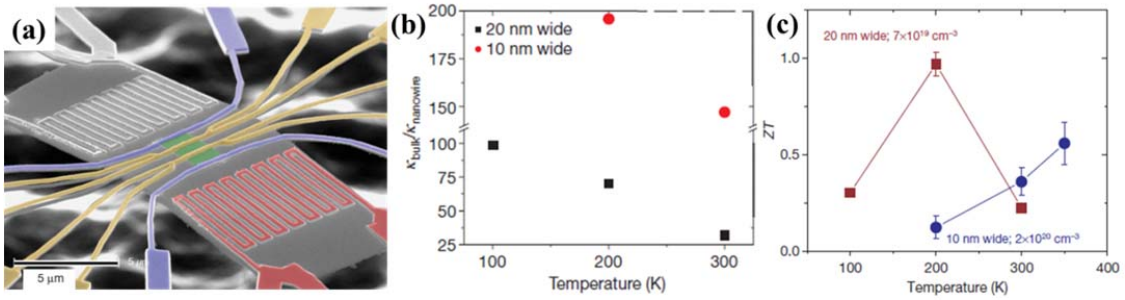


**Figure 1.12**: SEM image of an arrayed Si nanowire device to measure thermoelectric properties (a), temperature dependent thermal conductivity (κ), presented as $\kappa_{bulk}$ / $\kappa_{nanowires}$, of Si nanowires with diameters of 10 and 20 nm (b), and temperature dependent figure-of-merits of Si nanowires with different sizes and carrier concentrations (c) [12].

Moreover, the thermoelectric properties of Si nanowires with a rough surface morphology prepared by electroless etching process of highly doped Si wafers were compared with those of vapor-liquid-solid (VLS)-grown single crystal Si nanowires as shown in Figure 1.13 [11]. Compared to VLS-grown Si nanowires, the rough Si

nanowires demonstrated a remarkable thermoelectric figure-of-merit of 0.6, which was achieved by the reduction of the thermal conductivity due to increased surface phonon scattering.

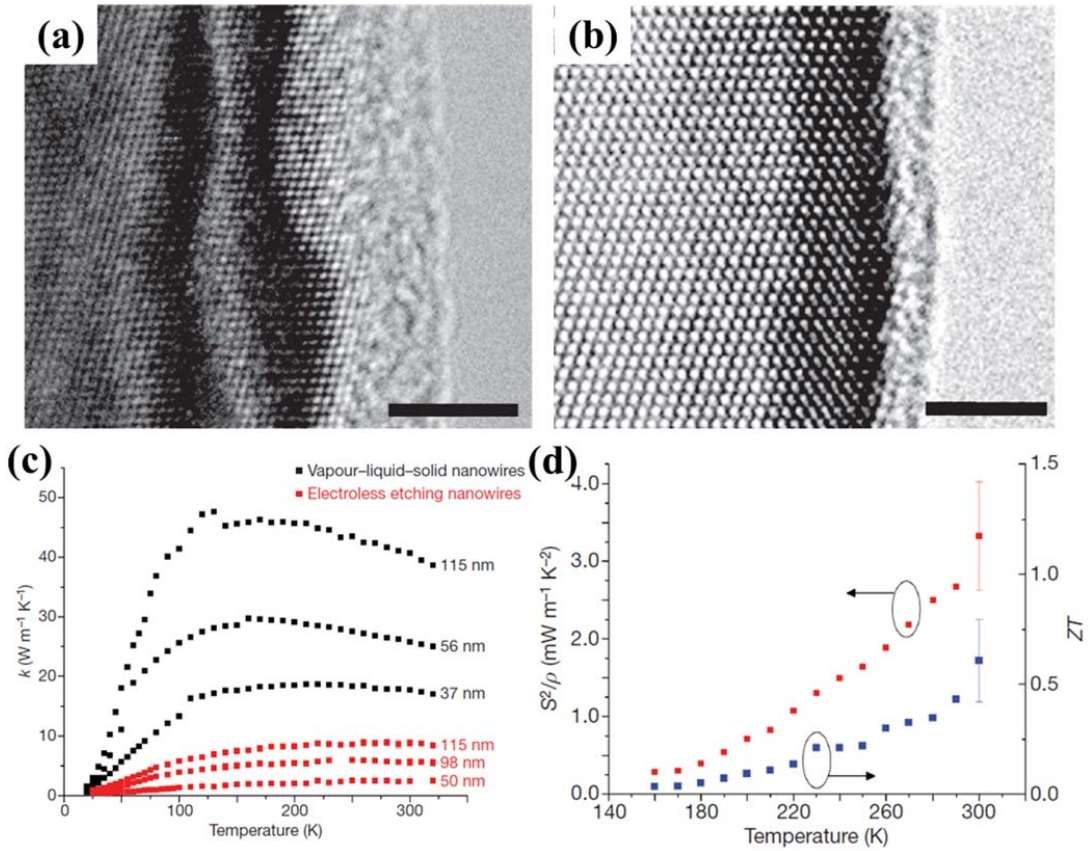


**Figure 1.13**: SEM images of electroless etching Si nanowire (a) and vapor-liquid-solid Si nanowire (b), temperature dependent thermal conductivity of both types of nanowires with different diameters (c) and temperature dependent power factor and figure-of-merit (ZT) of electroless etching Si nanowires with a diameter of 52 nm (d) [11].

## 1.2 Nanostructured Phase Change Memory

### 1.2.1 An Overview of Phase Change Memory

The continuing advance of the multimedia industry and the overwhelming production of data have encouraged the development of high performing computers, which are characterized by fast memory devices with a huge storage capacity. The performance of commercial memory devices has been estimated by the number and the performance of the transistors integrated on a circuit. A long-term trend of a computer technology performance can be described by Moore's law, formulated by Gordon Moore in 1965. Gordon Moore indicated that the number of transistors that could be housed on a given area of silicon doubles every two years. The period was modified to 18 months as illustrated in Figure 1.14.

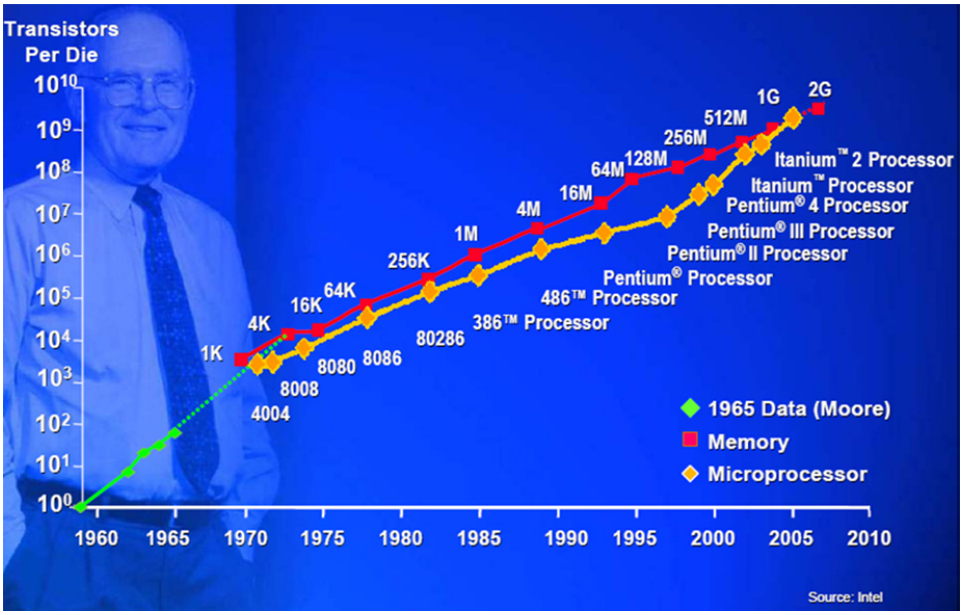


**Figure 1.14**: Schematic graph of the number of transistors integrated on silicon based on Moore's law (Source: Intel).

Even though the trend has been maintained by a size reduction of higher performance transistors with the advances in nanotechnology, the end of Moore's law is imminent. In response to the remarkable growth of current markets for portable devices, the development of non-volatile memory (NVM) devices have been proposed as an alternative memory device for the next generation computer technology. Unlike dynamic random access memory (DRAM), non-volatile memory can retain data even without being powered-on. Various novel non-volatile memory technologies have been explored over the conventional flash memory technologies (i.e. floating gate flash memory, NOR and NAND [34]): ferroelectric random access memory (FeRAM) [35-37], magnetoresistive random access memory (MRAM) [38-40], organic random access memory (PoRAM) [41-43] and phase change memory (PCM) [44-49]. Table 1.1 shows the operation mode and key characteristics of various memory devices. [50]

**Table 1.1**: Characteristics of Various Memory Technologies [50]

| Acronym | Memory Technology | Mode of Operation | Key Characteristics |
|---|---|---|---|
| DRAM | Dynamic random access memory | Charge is stored on a capacitor that is isolated from other memory bits in the array by a transistor. | Charge leakage from the capacitor is replenished by refresh circuitry. Refresh power dissipation increases with memory density. |
| FeRAM | Ferroelectric random access memory | Two directions of remnant polarization in a ferroelectric film represent the two memory states. | A stored datum is read out by detecting the polarization reversal current of a ferroelectric capacitor or the drain current of a ferroelectric gate field-effect transistor. |
| Flash | Floating gate memory | Charge on a floating gate | High fields transfer charge to and |

| | | | |
|---|---|---|---|
| Memory | | modifies the threshold voltage of the underlying transistor. | from the floating gate of a metal oxide semiconductor device, leading to relatively slower writes compared to reads and limited write endurance. |
| MRAM | Magnetoresistive random access memory | Parallel or opposite polarization of two ferromagnetic films on each side of a tunnel barrier produce high- and low-resistance paths. | The vector sum of magnetic fields generated by short pulse currents set the relative magnetization directions. Currents through the bits are used to read the states. |
| ORAM | Organic random access memory | Memory states are set due to the charge trapped in metallic nanoparticles within the organic material. | A nonvolatile memory in which organic layers are either in the high- or low-conductance modes, preset by external bias. |
| **PCM (OUM™)** | **Phase-change memory (Ovonic Unified Memory™)** | **Two solid-state phases having different resistivities represent the two memory states.** | **High reliability depends on the atom-positional switching reproducibility of the two phases.** |
| QDOT | Quantum dot memory | A type of flash memory in which the floating gate is replaced by a number of randomly arranged self-assembled quantum dots. | Scales to small dimensions at which a small number of electrons in the quantum dot can produce a large voltage change in the transistor. |
| SRAM | Static random-access memory | A transistor and its load are latched by a second transistor and load to maintain a memory state. | A fast memory that utilizes more area than DRAM and needs constant power to maintain the memory state. |
| ZRAM | Molecular random access memory | The oxidation state of porphyrin molecules produces charge states analogous to a DRAM capacitor. | Molecular memories can have high charge densities and can be scaled to nanosized dimensions. |

Phase change memory devices are one of most promising candidates for the next generation non-volatile memory devices owing to the improved performance of these devices. Compared to the other non-volatile memory devices, phase change memory demonstrates a large density range on devices from Mbits to Gbits, fast writing times, potential scalability, low power consumption and improved reliability as described in Table 1.2 [51].

**Table 1.2**: Comparison of Various Non-Volatile Memory Devices [51]

| Cell type | Flash | | FeRAM | MRAM | **PCM** |
|---|---|---|---|---|---|
| | NOR 1T | NAND 1T | 1T/1C | 1T/1R | 1T/1R |
| Cell size ($F^2$) | 10 | 5 | 30 - 100 | 10 - 30 | **8 - 10** |
| Endurance write/read | $10^6/\infty$ | 5 | $10^{12}/10^{12}$ | $> 10^{14}/\infty$ | $> 10^{12}/\infty$ |
| Read time (random) | 60 ns | | 80 + 80 ns | 30 ns | 60 ns |
| Write time (byte) | 1 μs | 60 ns/serial | (read + write | 30 ns | **10 ns** |
| Erase time (byte) | 1 s/sector | 200 μs/page | destructive read) | 30 ns | 100 ns |
| Scalability | Fair | 2 ms/block | Poor | Poor | **Good** |
| Scalability limits | Tunnel oxide, HV | | Capacitor | Current density | Litho |
| Multi-bit capacity | Yes | | No | No | **Yes** |
| 3D Potential | No | | No | No | **Yes** |
| Relative Cost x bit | Medium | Low | High | High | **Medium** |
| Maturity | Very high | | Low | Low | Low |

* T: transistor, C: capacitor, R: resistor
F: technology node (e.g., 1F for 90 nm node technology is 90 nm; $1F^2 = (90\ nm)^2$)

A memory application based on the properties of an amorphouse to crystalline phase transition was suggested by S. R. Ovshinsky in 1960s [52]. The phase transition property was first applied to memory devices to store data optically [53]. The optical disc of phase change memory devices was commercialized as a 4.7 GB digital versatile disc random access memory (DVD-RAM) in the late 1990s and various materials for phase change memory devices have been examined since. Recently, phase change memory devices for electrical data storage have been investigated.

The optical and electrical data storage of phase transition materials can be operated by an irradiated laser beam and an applied current, respectively, as shown in Figure 1.15 [46].

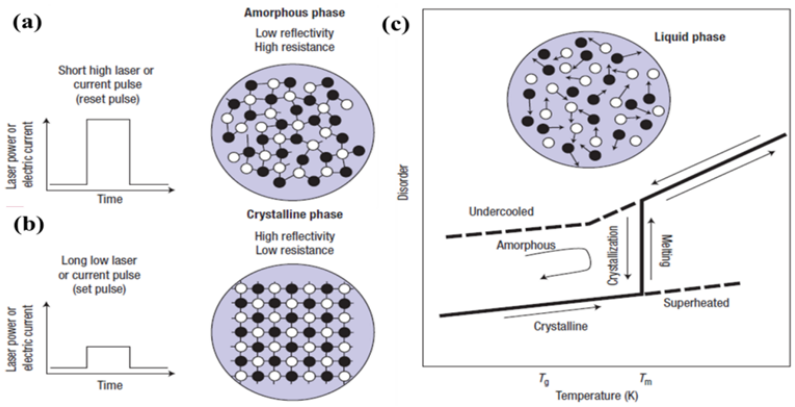


**Figure 1.15**: Rewriteable optical and electrical data storage using phase-change materials. Local heating of the phase-change material above its melting temperature with a short and high intensity laser beam (current pulse) and rapid cooling quenches the liquid-like state into a disordered, amorphous phase (a). Adversely, local heating of the materials with a long and low intensity laser beam (current pulse) at temperatures above the glassy temperature ($T_g$) can revert the material to the energetically favorable crystalline state, erasing the recorded information (b). The crystallinity of materials was controlled by heating and cooling (c) [46].

The function of phase transition materials as a memory device can be utilized by the differences of the refractive index and the electrical resistance between the amorphous (low refractive index and high electrical resistance) and crystalline (high refractive index and low electrical resistance) states. The heating and cooling of materials for phase transitions can be controlled by the intensity and wavelength of the laser beam or by the power and width of the current pulse, where the short high laser (or current pulse) can generate the amorphous state and the long low laser (or current pulse) can create crystalline states. The phase transition from the crystalline to the amorphous state is a recording (reset) step and the transition from the amorphous to the crystalline state is an erasing step (set).

The current pulse is programmed to implement the phase transition in a memory device and the I-V characteristics of a memory device are shown in Figure 1.16 [44]. The SET state in crystallization and the RESET state in amorphization correspond to a stored binary 1 and binary 0 of the memory device, respectively. I-V characteristics indicate that the conductivity in an amorphous state is initially ohmic with increasing voltage, but it begins to grow exponentially in a crystalline state. When a particular threshold voltage ($V_{th}$) is exceeded, the material rapidly switches from the “off” state to the “on” state.

The basic cell structure of phase change memory devices is composed of one transistor and one resistor (1T/1R). The configuration of phase change memory devices has been developed, based on the key considerations of the needed thermal efficiency to operate in low programming currents and maintaining a small volume to achieve high densities.

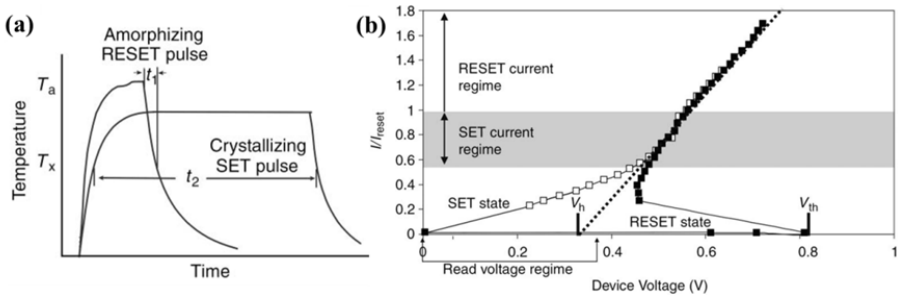


**Figure 1.16**: Schematic of temperature vs. time during current pulse programming (a) and I-V characteristics in both the RESET and SET states; $V_h$ is the holding voltage and $V_{th}$ is the switching threshold voltage [44].

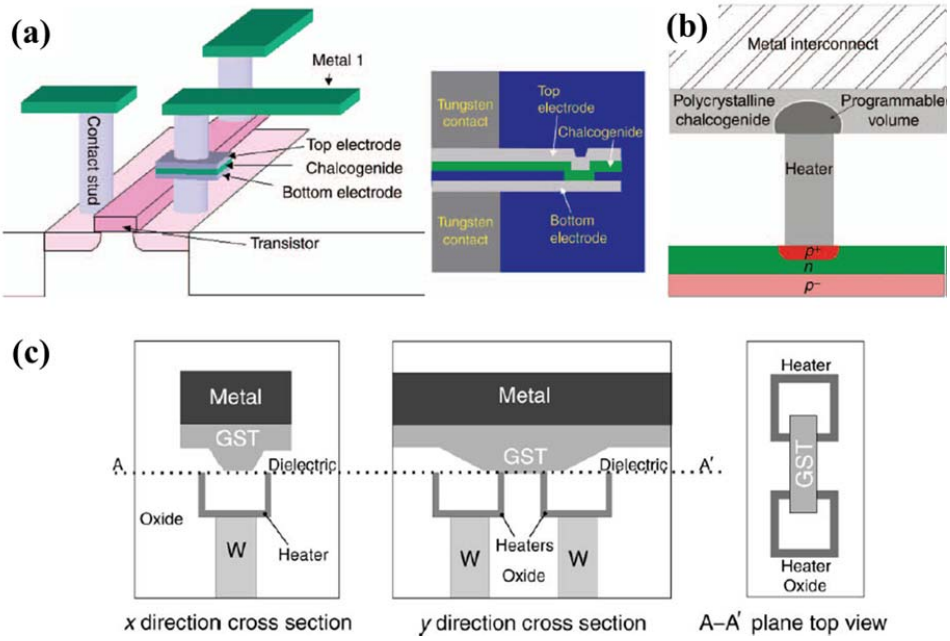


**Figure 1.17**: Schematic diagrams of various phase change memory devices with optimized designs: a lateral offset Ovonic Unified Memory (OUM) structure with complementary metal oxide semiconductor (CMOS) access device (a), a bipolar junctioned transistor (BJT)-selected phase change memory cell (b) and an OUM structure with MOS which has a microtrench design (c) [44, 54]

There are three representative types of commercialized phase change memory devices.

One of them is a lateral offset Ovonic Unified Memory (OUM) structure with a

complementary metal oxide semiconductor (CMOS) access device which was designed to improve the thermal efficiency by Ovonyx/BAE Systems as shown in Figure 1.17 (a) [44, 54]. Another approach was achieved by a bipolar junctioned transistor (BJT)-selected phase change memory cell by Ovonyx/Intel as described in Figure 1.17 (b) [44, 55]. BJT-selected phase change memory could feature a small cell size for high density chips and improve the thermal efficiency. Ovonix/STMicroelectronics developed an OUM structure with MOS which has a microtrench design with a small contact area between a heater and a phase change material as illustrated in Figure 1.17 (c) [44, 56]. Device design has been heavily investigated to improve the performance of phase change memory devices.

### 1.2.2 Phase Transition Materials

Various phase transition materials have been developed by extensive trial-and-error approaches, because the performance of phase change memory devices is limited by the properties of the phase transition material employed. The key parameters of phase transition materials for a memory device application are fast response times on the order of a nanosecond time scale for crystallization/amorphization and a high stability of the amorphous phase against spontaneous crystallization. These requirements have been fulfilled by various semiconductor alloys containing Ge (Ag and In), Sb and Te as shown in the ternary phase diagram of Figure 1.18 [46]. Phase transition materials can be classified into two categories based on their crystallization mechanism: nucleation dominant materials and growth dominant materials. Ge-Sb-Te systems demonstrated

nucleation dominant recrystallization which was limited by the growth rate [57-59]. However, the crystallization of a $Sb_{70}Te_{30}$ system was dominated by the fast growth of the material [59, 60]. $Ge_2Sb_2Te_5$ (GST) and related materials such as GeSbTeN, GeBiSbTe, GeBiTe and GeInSbTe have been investigated for use in commercial phase change memories [61-64]. $Ag_5In_5Sb_{60}Te_{30}$ (AIST) and related doped $Sb_{70}Te_{30}$ alloys have also exhibited high performance in the key properties necessary for use as phase transition materials [65-68].

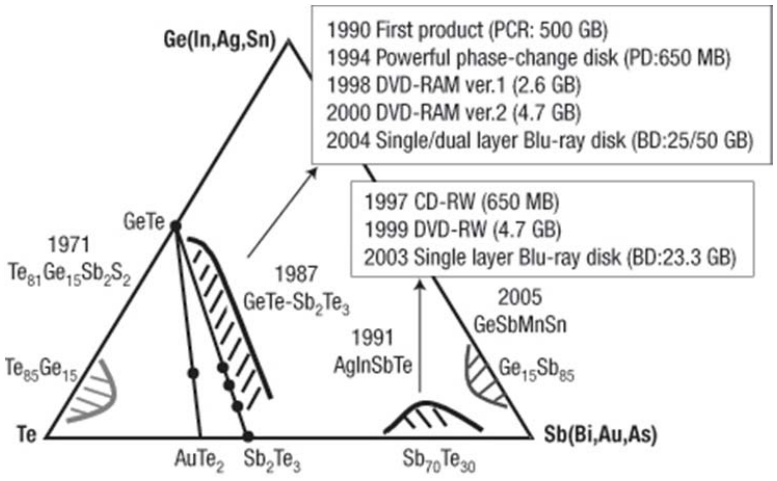


**Figure 1.18**: Ternary phase diagram of phase transition alloys containing Ge (Ag and In), Sb and Te [46].

Figure 1.19 describes why switching in $Ge_2Sb_2Te_5$ phase transition materials is fast and stable [46, 69]. $Ge_2Sb_2Te_5$ showed the crystal structure of a rock-salt-like phase, where Te atoms occupy one sublattice to form a face centered cubic structure, and Ge atoms, Sb atoms and vacancies randomly occupy another sublattice as illustrated in Figure 1.19 (a). In the crystalline state with long-range ordering, Ge atoms occupy

octahedral sites with strong covalent bonds to Te atoms (Figure 1.19 (b)). The amorphization can be carried out by the weakened interaction between the Ge and Te atoms, resulting in umbrella-flips of Ge atoms into their preferred tetrahedral sites as shown in Figure 1.19 (c). The fast and stable phase transition can be achieved by the feasible rupture of covalent bonds and a diffusionless transition.

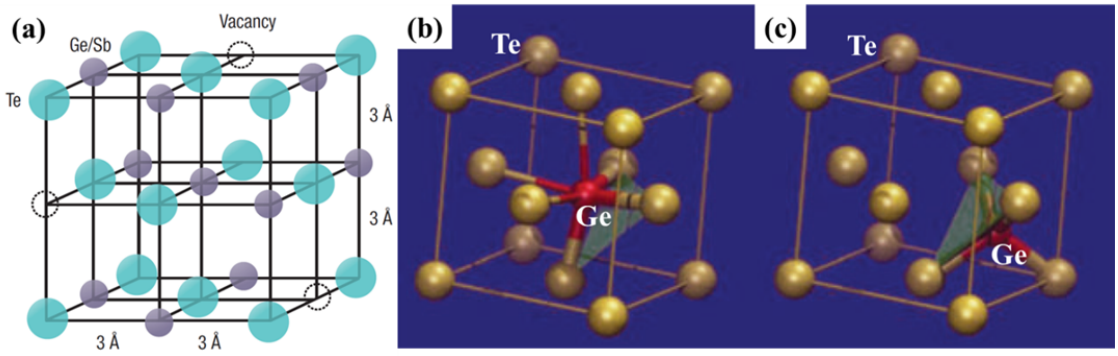


**Figure 1.19**: Crystal structure of $Ge_2Sb_2Te_5$ with the rock-salt-like phase (a), a Ge atom on an octahedral site in crystalline $Ge_2Sb_2Te_5$ (b) and a Ge atom on a tetrahedral site in amorphous $Ge_2Sb_2Te_5$ (c) [46, 69].

### 1.2.3 Improved Performance of Nanostructured Phase Change Memory

Non-volatile phase change memory has been widely investigated for implementation in a potential next generation of non-volatile solid state memory technology. The performance of phase change memory devices has been developed to provide a better trade-off between the scalability and reliability of devices. The competitiveness of a phase change memory device can be achieved by creating fast phase transition speeds, low power consumption and scalability. Table 1.3 shows the required properties of a phase change memory device.

Table 1.3: The required properties of a competitive phase change memory device

| **Required Properties of Phase Change Memory** | **Specification** |
|---|---|
| High speed phase transition | Induced by pulse duration |
| Low power consumption | Threshold voltage |
| Long thermal stability of amorphous state | More than ~10 years ($3 \times 10^8$ s) |
| Large cycle number of reversitble transition | More thant 100,000 cycles with stable composition |
| High chemical stability | High water resistivity |
| Lage resistance contrast between the two states | Natural consequence of the transformation |
| Data storage capacity | Memory cell dimension |

1-Dimensional nanostructured phase change memory has been the subject of considerable recent interest to create a high performance device. The application of 1-dimensional nanostructures to phase change memory devices has indicated the potential for remarkable improvement in high performance devices [45, 70-77]. 1-Dimensional nanostructures with a reduced dimension can be used in high density devices with a small programmable cell volume and the need for low programming currents due to that reduced volume. An additional reduction of programming currents in a 1-dimensional device can be achieved by the utilization of the reduced melting temperature of phase transition materials, since the melting points of materials in the nanoscale are smaller than the bulk values. Figure 1.20 describes the diameter-dependent reduction of the reset current in a GeTe 1-dimensional nanostructure (a) and simulated temperature evolution during the set processes at the center of nanowires with different device lengths (b) [71, 77]. The reset (amorphous to crystalline state) currents were reduced by the decrease of

the nanowire diameter and the generated temperature at the center of nanowire increased with decrease in the length of nanowires.

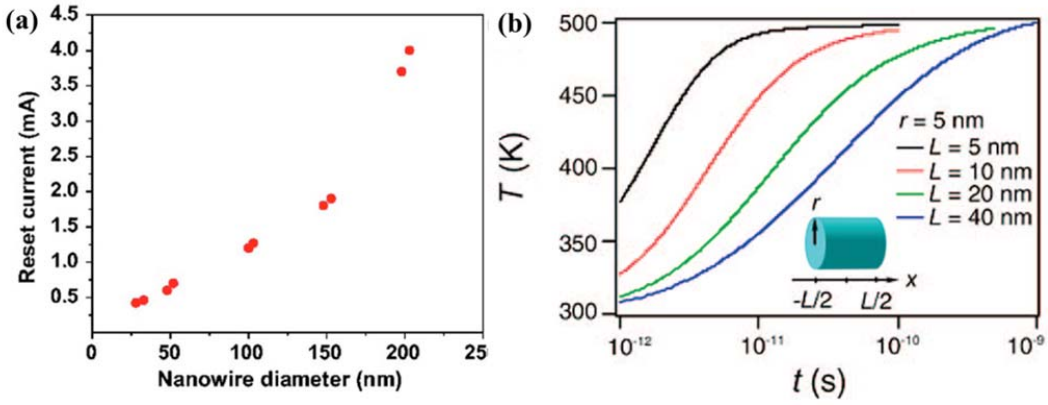


**Figure 1.20**: Size dependent memory switching properties: (a) diameter-dependent reduction of the reset current of a GeTe nanowire and (b) Simulated temperature evolution during the set processes at the center of nanowires with different lengths as a function of time [71, 77].

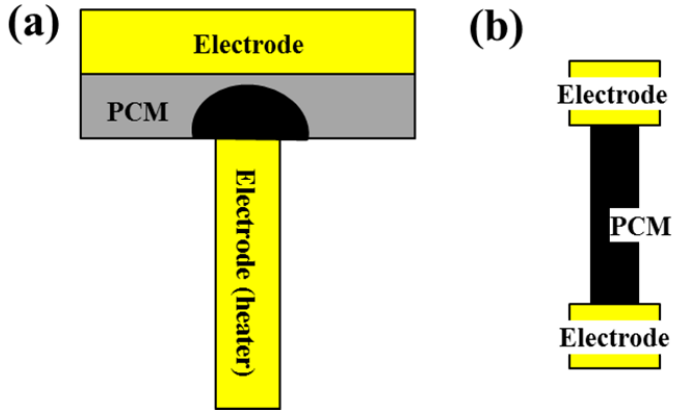


Figure 1.21: Schematic diagrams of phase change memory cells: thin film-based Ovonic Unified Memory (a) and nanowire-based memory cell (b). The relative phase transition area is depicted in black.

Compared to the thin film-based phase change memory devices such as an Ovonic Unified Memory device, 1-dimensional nanostructured phase change memory devices can increase the relative phase transition area of a phase transition material due to the Joule heating of a heater electrode as illustrated in Figure 1.21. This increased transition area can reduce heat loss, resulting in a reduction of the reset programming currents. The success of highly integrated phase change memory devices will be dependent on the development of high performance devices with high yields and cost-effective fabrication techniques. A phase change memory device with high performance has been developed by taking various approaches: using phase transition materials, reducing cell dimensions and creating well-designed memory cells. Table 1.4 lists the key phase change memory characteristics depending on the chosen materials and dimensions.

**Table 1.4**: The properties of phase change memory materials for electrical data storage

| **Phase transition materials** | **Dimension** | **Pulse duration** | **$V_{th}$** | **Cyclic endurance** |
|---|---|---|---|---|
| $Ge_2Sb_2Te_5$ (GST) | | | | |
| [70] Nanowire | ~60 nm x 1μm | 50 ~ 500 ns | 1.8 V | ~ $10^5$ cycles |
| [78] Thin film | 0.5 x 0.5 $\mu m^2$ | 120 ns | 3.0 V | - |
| [71] $Sb_2Te_3$ nanowire | ~0.1 x 1 $\mu m^2$ | 500 ns | 0.75 V | - |
| | ~80 nm x 7 μm | 200 ns | 0.6 V | |
| [79] doped SbTe Thin line | ~25 x 100 $nm^2$ | 100 ns | 1.0 V | ~ $10^7$ cycles |
| [80] Ag doped SbTe | 0.5 x 0.5 $\mu m^2$ | - | 1.8 V (forward) / -1.2 V (reverse) | - |

| | | | | |
|---|---|---|---|---|
| [79] $Sb_2Te_3$/GeTe core shell nanowire | ~ 0.2 x 1 $\mu m^2$ | 100 ns | 1.0 V | - |
| [71, 77] GeTe nanowire | 0.1 x 1 $\mu m^2$<br>30 nm x 1 $\mu m$ | 100 ns<br>300 ns | 0.8 V | - |
| [81] $Ga_2Te_3Sb_5$ thin film | 0.2 x 0.2 $\mu m^2$ | 500 ns | 1.5~0.6 V | ~$10^4$ cycles |

## 1.3 Research Objectives

Chalcogenide materials with the elements of sulfur sub-group such as tellurium and selenium have been widely used in various fields, because of their attractive electrical and optical properties. The applications of chalcogenides to thermoelectric and phase change memory devices have shown a potential to approach to the issues of energy and computer technologies. Recently, the performance of the devices has been improved by the engineered chalcogenide materials with the advanced nanotechnologies. However, the fabrication of nanostructured chalcogenide materials has been performed by the limited and expensive processes.

The overall objective of this work is to develop the novel cost-effective, scalable fabrication techniques of chalcogenide materials with the enhanced properties for the thermoelectric and the electrical phase change memory applications. The synthesis of the nanostructured chacogenide materials was carried out by the development of the chemical and the electrochemical routes. The properties of thermoelectric and phase transition materials were developed by the control of dimension, size and composition. The specific aims of this work were the following:

1) Developing cost-effective and scalable techniques (i.e., potentiostatic deposition, pulse plating, galvanic displacement reaction, topochemical transformation reaction and cation exchange reaction) to synthesize chalcogenide materials.

2) Controlling dimension (i.e., 3-dimensional bulks, 2-dimensional thin films, and 1-dimensional nanowires and nanoribbons), size, and composition of materials by varying various parameters.
3) Investigating thermoelectric properties including electrical resistivity and Seebeck coefficients depending on the properties of the synthesized materials. In addition, FET properties are measured to study the specific carrier transport behavior.
4) Investigating phase transition properties including the transition temperature and the resistivity variation depending on the compositions of the synthesized materials.
5) Understanding the effects of the engineered nanostructures on thermoelectric and phase transition properties for the high performance of the devices.

## 1.4 Thesis Organization

This thesis is organized as follow:

Chapter 2 describes the electrodeposition of three dimensional antimony telluride bulks. The electrochemical analysis is performed with various tools such as rotating disk electrodes and quartz crystal microbalance, and then thermoelectric and phase transition properties is measured as a function of temperatures and compositions. The enhanced properties are estimated by the generated nanocomposite due to a phase separation. Chapter 3 shows that two dimensional binary silver telluride and ternary silver antimony telluride thin films are synthesized by a topochemical transformation reaction of tellurium and a cation exchange reaction of antimony telluride, respectively. The composition-dependent thermoelectric and phase transition properties are investigated. In Chapter 4, one dimensional nanostructure is described. Lead Telluride nanowires are synthesized by a template-direct method, and tellurium, bismuth telluride and antimony telluride nanoribbons are fabricated by the electrodeposition and the galvanic displacement reaction on lithographical patterns. The electrical transport behaviors of the one dimensional nanostructures are analyzed.

## 1.5 References


[1] U. S. E. I. Administration, *Annual energy review 2009,* Department Of Energy, 2010.

[2] D. M. Rowe, *CRC Handbook of Thermoelectrics,* Boca Raton, CRC Press, Inc., 1995.

[3] G. J. Snyder and E. S. Toberer, Complex thermoelectric materials, *Nature Materials,* 2008. 7: p. 105-114

[4] G. J. Snyder, Small Thermoelectric Generators, *The Electrochemical Society Interface,* 2008. 17: p. 54-56

[5] L. A. Fisk, Journey into the Unknown Beyond, *Science,* 2005. 309: p. 2016-2017

[6] A. Majumdar, Thermoelectricity in Semiconductor Nanostructures, *Science,* 2004. 303: p. 777-778

[7] K. F. Hsu, S. Loo, F. Guo, W. Chen, J. S. Dyck, C. Uher, T. Hogan, E. K. Polychroniadis and M. G. Kanatzidis, Cubic $AgPb_mSbTe_{2+m}$: Bulk Thermoelectric Materials with High Figure of Merit, *Science,* 2004. 303: p. 818-821

[8] R. Venkatasubramanian, E. Siivola, T. Colpitts and B. O'Quinn, Thin-film thermoelectric devices with high room-temperature figures of merit, *Nature,* 2001. 413: p. 597-602

[9] B. Poudel, Q. Hao, Y. Ma, Y. Lan, A. Minnich, B. Yu, X. Yan, D. Wang, A. Muto, D. Vashaee, X. Chen, J. Liu, M. S. Dresselhaus, G. Chen and Z. Ren, High-Thermoelectric Performance of Nanostructured Bismuth Antimony Telluride Bulk Alloys, *Science,* 2008. 320: p. 634-638

[10] T. C. Harman, P. J. Taylor, M. P. Walsh and B. E. LaForge, Quantum Dot Superlattice Thermoelectric Materials and Devices, *Science,* 2002. 297: p. 2229-2232

[11] A. I. Hochbaum, R. Chen, R. D. Delgado, W. Liang, E. C. Garnett, M. Najarian, A. Majumdar and P. Yang, Enhanced thermoelectric performance of rough silicon nanowires, *Nature,* 2008. 451: p. 163-167

[12] A. I. Boukai, Y. Bunimovich, J. Tahir-Kheli, J.-K. Yu, W. A. Goddard Iii and J. R. Heath, Silicon nanowires as efficient thermoelectric materials, *Nature,* 2008. 451: p. 168-171

[13] D. M. Rowe and V. S. Shukla, The effect of phonon-grain boundary scattering on the lattice thermal conductivity and thermoelectric conversion efficiency of heavily doped fine-grained, hot-pressed silicon germanium alloy, *Journal of Applied Physics,* 1981. 52: p. 7421-7426

[14] A. Balandin and K. L. Wang, Significant decrease of the lattice thermal conductivity due to phonon confinement in a free-standing semiconductor quantum well, *Physical Review B,* 1998. 58: p. 1544

[15] A. Balandin and K. L. Wang, Effect of phonon confinement on the thermoelectric figure of merit of quantum wells, *Journal of Applied Physics,* 1998. 84: p. 6149-6153

[16] H. Beyer, J. Nurnus, H. Bottner, A. Lambrecht, T. Roch and G. Bauer, PbTe based superlattice structures with high thermoelectric efficiency, *Applied Physics Letters,* 2002. 80: p. 1216-1218

[17] L. D. Hicks and M. S. Dresselhaus, Thermoelectric figure of merit of a one-dimensional conductor, *Physical Review B,* 1993. 47: p. 16631

[18] L. D. Hicks and M. S. Dresselhaus, Effect of quantum-well structures on the thermoelectric figure of merit, *Physical Review B,* 1993. 47: p. 12727

[19] A. P. Alivisatos, Perspectives on the Physical Chemistry of Semiconductor Nanocrystals, *The Journal of Physical Chemistry,* 1996. 100: p. 13226-13239

[20] U. S. Martin Dressel, George Grüner, *Electrodynamics of Solids,* Cambridge, Cambridge University Press, 2002.

[21] J. P. Heremans, V. Jovovic, E. S. Toberer, A. Saramat, K. Kurosaki, A. Charoenphakdee, S. Yamanaka and G. J. Snyder, Enhancement of Thermoelectric Efficiency in PbTe by Distortion of the Electronic Density of States, *Science,* 2008. 321: p. 554-557

[22] J. M. O. Zide, D. Vashaee, Z. X. Bian, G. Zeng, J. E. Bowers, A. Shakouri and A. C. Gossard, Demonstration of electron filtering to increase the Seebeck coefficient in $In_{0.53}Ga_{0.47}As/In_{0.53}Ga_{0.28}Al_{0.19}As$ superlattices, *Physical Review B,* 2006. 74: p. 205335

[23] J. Martin, L. Wang, L. Chen and G. S. Nolas, Enhanced Seebeck coefficient through energy-barrier scattering in PbTe nanocomposites, *Physical Review B,* 2009. 79: p. 115311

[24] D. Vashaee and A. Shakouri, Improved Thermoelectric Power Factor in Metal-Based Superlattices, *Physical Review Letters,* 2004. 92: p. 106103

[25] Y. Ma, Q. Hao, B. Poudel, Y. Lan, B. Yu, D. Wang, G. Chen and Z. Ren, Enhanced Thermoelectric Figure-of-Merit in p-Type Nanostructured Bismuth Antimony Tellurium Alloys Made from Elemental Chunks, *Nano Letters,* 2008. 8: p. 2580-2584

[26] W. Xie, X. Tang, Y. Yan, Q. Zhang and T. M. Tritt, Unique nanostructures and enhanced thermoelectric performance of melt-spun BiSbTe alloys, *Applied Physics Letters,* 2009. 94: p. 102111-3

[27] Y. Q. Cao, X. B. Zhao, T. J. Zhu, X. B. Zhang and J. P. Tu, Syntheses and thermoelectric properties of $Bi_2Te_3/Sb_2Te_3$ bulk nanocomposites with laminated nanostructure, *Applied Physics Letters,* 2008. 92: p. 143106-3

[28] M. S. Dresselhaus, G. Chen, M. Y. Tang, R. G. Yang, H. Lee, D. Z. Wang, Z. F. Ren, J. P. Fleurial and P. Gogna, New Directions for Low-Dimensional Thermoelectric Materials, *Advanced Materials,* 2007. 19: p. 1043-1053

[29] A. J. Minnich, M. S. Dresselhaus, Z. F. Ren and G. Chen, Bulk nanostructured thermoelectric materials: current research and future prospects, *Energy & Environmental Science,* 2009. 2: p. 466-479

[30] R. Venkatasubramanian, T. Colpitts, B. O'Quinn, S. Liu, N. El-Masry and M. Lamvik, Low-temperature organometallic epitaxy and its application to superlattice structures in thermoelectrics, *Applied Physics Letters,* 1999. 75: p. 1104-1106

[31] R. Venkatasubramanian, Lattice thermal conductivity reduction and phonon localizationlike behavior in superlattice structures, *Physical Review B,* 2000. 61: p. 3091

[32] T. Harman, M. Walsh, B. laforge and G. Turner, Nanostructured thermoelectric materials, *Journal of Electronic Materials,* 2005. 34: p. L19-L22

[33] T. Harman, P. Taylor, D. Spears and M. Walsh, Thermoelectric quantum-dot superlattices with high ZT, *Journal of Electronic Materials,* 2000. 29: p. L1-L2

[34] A. Fazio, Flash Memory Scaling, *MRS Bulletin,* 2004. 29: p. 814-817

[35] G. R. Fox, F. Chu and T. Davenport, Current and future ferroelectric nonvolatile memory technology, *Journal of Vacuum Science & Technology B: Microelectronics and Nanometer Structures,* 2001. 19: p. 1967-1971

[36] R. E. Jones, P. D. Maniar, R. Moazzami, P. Zurcher, J. Z. Witowski, Y. T. Lii, P. Chu and S. J. Gillespie, Ferroelectric non-volatile memories for low-voltage, low-power applications, *Thin Solid Films,* 1995. 270: p. 584-588

[37] Y. Arimoto and H. Ishiwara, Current Status of Ferroelectric Random-Access Memory, *MRS Bulletin,* 2004. 29: p. 823-828

[38] S. Tehrani, J. M. Slaughter, M. Deherrera, B. N. Engel, N. D. Rizzo, J. Salter, M. Durlam, R. W. Dave, J. Janesky, B. Butcher, K. Smith and G. Grynkewich, Magnetoresistive random access memory using magnetic tunnel junctions, *Proceedings of the IEEE,* 2003. 91: p. 703-714

[39] G. Grynkewich, J. Akerman, P. Brown, B. Butcher, R. W. Dave, M. DeHerrera, M. Durlam, B. N. Engel, J. Janesky, S. Pietambaram, N. D. Rizzo, J. M. Slaughter,

K. Smith, J. J. Sun and S. Tehrani, Nonvolatile Magnetoresistive Random-Access Memory Based on Magnetic Tunnel Junctions, *MRS Bulletin,* 2004. 29: p. 818-821

[40] S. Tehrani, E. Chen, M. Durlam, M. DeHerrera, J. M. Slaughter, J. Shi and G. Kerszykowski, High density submicron magnetoresistive random access memory (invited), *Journal of Applied Physics,* 1999. 85: p. 5822-5827

[41] Y. Yang, L. Ma and J. Wu, Organic Thin-Film Memory, *MRS Bulletin,* 2004. 29: p. 833-837

[42] R. J. Tseng, J. Huang, J. Ouyang, R. B. Kaner and Yang, Polyaniline Nanofiber/Gold Nanoparticle Nonvolatile Memory, *Nano Letters,* 2005. 5: p. 1077-1080

[43] Y. Yang, J. Ouyang, L. Ma, R. J. H. Tseng and C. W. Chu, Electrical Switching and Bistability in Organic/Polymeric Thin Films and Memory Devices, *Advanced Functional Materials,* 2006. 16: p. 1001-1014

[44] S. Hudgens and B. Johnson, Overview of Phase-Change Chalcogenide Nonvolatile Memory Technology, *MRS Bulletin,* 2004. 29: p. 829-832

[45] M. H. R. Lankhorst, B. W. S. M. M. Ketelaars and R. A. M. Wolters, Low-cost and nanoscale non-volatile memory concept for future silicon chips, *Nat Mater,* 2005. 4: p. 347-352

[46] M. Wuttig and N. Yamada, Phase-change materials for rewriteable data storage, *Nat Mater,* 2007. 6: p. 824-832

[47] A. Pirovano, A. L. Lacaita, A. Benvenuti, F. Pellizzer and R. Bez, Electronic switching in phase-change memories, *Electron Devices, IEEE Transactions on,* 2004. 51: p. 452-459

[48] M. Ohtsu, K. Kobayashi, T. Kawazoe, S. Sangu and T. Yatsui, Nanophotonics: design, fabrication, and operation of nanometric devices using optical near fields, *Selected Topics in Quantum Electronics, IEEE Journal of,* 2002. 8: p. 839-862

[49] T. Ohta, Phase Change Memory and Breakthrough Technologies, *Magnetics, IEEE Transactions on,* 2011. 47: p. 613-619

[50] H. Goronkin and Y. Yang, High-Performance Emerging Solid-State Memory Technologies, *MRS Bulletin,* 2004. 29: p. 805-813

[51] R. Bez and A. Pirovano, Non-volatile memory technologies: emerging concepts and new materials, *Materials Science in Semiconductor Processing,* 2004. 7: p. 349-355

[52] S. R. Ovshinsky, Reversible Electrical Switching Phenomena in Disordered Structures, *Physical Review Letters,* 1968. 21: p. 1450

[53] S. R. O. Takeo Ohta, *Photo-induced Metastability in Amorphous Semiconductors,* Berlin, Wiley-VCH, 2003.

[54] K. H. J. Maimon, L. Burcin, J. Rodgers, and K. Knowles, Integration and circuit demonstration of chalcogenide memory elements with a radiation hardened CMOS technology*, Proc. Non-Volatile Memory Technol. Symp.,* 2002.

[55] M. Gill, T. Lowrey and J. Park, Ovonic unified memory - a high-performance nonvolatile memory technology for stand-alone memory and embedded

applications*, Proc. Solid-State Circuits Conference, 2002. Digest of Technical Papers. ISSCC. 2002 IEEE International,* 2002.

[56] F. Pellizzer, A. Pirovano, F. Ottogalli, M. Magistretti, M. Scaravaggi, P. Zuliani, M. Tosi, A. Benvenuti, P. Besana, S. Cadeo, T. Marangon, R. Morandi, R. Piva, A. Spandre, R. Zonca, A. Modelli, E. Varesi, T. Lowrey, A. Lacaita, G. Casagrande, P. Cappelletti and R. Bez, Novel μtrench phase-change memory cell for embedded and stand-alone non-volatile memory applications*, Proc. VLSI Technology, 2004. Digest of Technical Papers. 2004 Symposium on,* 2004.

[57] S.-H. Lee, Y. Jung and R. Agarwal, Size-Dependent Surface-Induced Heterogeneous Nucleation Driven Phase-Change in $Ge_2Sb_2Te_5$ Nanowires, *Nano Letters,* 2008. 8: p. 3303-3309

[58] B. J. Kooi, W. M. G. Groot and J. T. M. De Hosson, In situ transmission electron microscopy study of the crystallization of $Ge_2Sb_2Te_5$, *Journal of Applied Physics,* 2004. 95: p. 924-932

[59] G. Zhou, H. J. Borg, J. C. N. Rijpers, M. H. R. Lankhorst and J. J. L. Horikx, Crystallization behavior of phase-change materials: comparison between nucleation- and growth-dominated crystallization*, Proc. Optical Data Storage 2000,* 2000.

[60] M. L. Lee, L. P. Shi, Y. T. Tian, C. L. Gan and X. S. Miao, Crystallization behavior of $Sb_{70}Te_{30}$ and $Ag_3In_5Sb_{60}Te_{32}$ chalcogenide materials for optical media applications, *physica status solidi (a),* 2008. 205: p. 340-344

[61] R. Kojima, Nitrogen doping effect on phase change optical disks, *Jpn. J. Appl. Phys. Part 1,* 1998. 37: p. 2098-2103

[62] R. Kojima and N. Yamada, Acceleration of crystallization speed by Sn addition to Ge-Sb-Te phase-change recording material, *Jpn. J. Appl. Phys. Part 1,* 2001. 40: p. 5930-5937

[63] H. Kusada, T. Hosaka and N. Yamada, Effect of excess Sb on GeTe-$Sb_2Te_3$-$Bi_2Te_3$ recording films, *Proc. 18th Symp. PCOS2005,* 2006. p. 32-35

[64] K. Yusu, T. Nakai, S. Ashida, N. Ohmachi, N. Morishita and N. Nakamura, High speed crystallization characteristics of Ge-Sb-Te-Bi materials used for next generation rewritable DVD with blue laser and NA = 0.65*, Proc. Proc. E\PCOS05,* 2005.

[65] M. Horie, N. Nobukuni, K. Kiyono and T. Ohno, High-speed rewritable DVD up to 20 m/s with nucleation-free eutectic phase-change material of Ge($Sb_{70}Te_{30}$)+Sb, *Proc. SPIE,* 2000. 4090: p. 135-143

[66] H. Iwasaki, Completely erasable phase-change optical disc. II. Application of Ag-In-Sb-Te mixed-phase system for rewritable compact disc compatible with CD-velocity and double CD-velocity, *Jpn. J. Appl. Phys. Part 1,* 1993. 32: p. 5241-5247

[67] H. Iwasaki, Y. Ide, M. Harigaya, Y. Kageyama and I. Fujimura, Completely erasable phase-change optical disk, *Jpn. J. Appl. Phys. Part 1,* 1992. 31: p. 461-465

[68] T. Kato, The phase change optical disc with the data recording rate of 140 Mbps, *Jpn. J. Appl. Phys. Part 1,* 2002. 41: p. 1664-1667

[69] A. V. Kolobov, P. Fons, A. I. Frenkel, A. L. Ankudinov, J. Tominaga and T. Uruga, Understanding the phase-change mechanism of rewritable optical media, *Nat Mater,* 2004. 3: p. 703-708

[70] S.-H. Lee, Y. Jung and R. Agarwal, Highly scalable non-volatile and ultra-low-power phase-change nanowire memory, *Nat Nano,* 2007. 2: p. 626-630

[71] D. Yu, S. Brittman, J. S. Lee, A. L. Falk and H. Park, Minimum Voltage for Threshold Switching in Nanoscale Phase-Change Memory, *Nano Letters,* 2008. 8: p. 3429-3433

[72] Y. C. Chen, C. T. Rettner, S. Raoux, G. W. Burr, S. H. Chen, R. M. Shelby, M. Salinga, W. P. Risk, T. D. Happ, G. M. McClelland, M. Breitwisch, A. Schrott, J. B. Philipp, M. H. Lee, R. Cheek, T. Nirschl, M. Lamorey, C. F. Chen, E. Joseph, S. Zaidi, B. Yee, H. L. Lung, R. Bergmann and C. Lam, Ultra-Thin Phase-Change Bridge Memory Device Using GeSb*, Proc. Electron Devices Meeting, 2006. IEDM '06. International,* 2006.

[73] Y. Bin, S. Xuhui, J. Sanghyun, D. B. Janes and M. Meyyappan, Chalcogenide-Nanowire-Based Phase Change Memory, *Nanotechnology, IEEE Transactions on,* 2008. 7: p. 496-502

[74] B. Yu, S. Ju, X. Sun, G. Ng, T. D. Nguyen, M. Meyyappan and D. B. Janes, Indium selenide nanowire phase-change memory, *Applied Physics Letters,* 2007. 91: p. 133119-3

[75] D. Yu, J. Wu, Q. Gu and H. Park, Germanium Telluride Nanowires and Nanohelices with Memory-Switching Behavior, *Journal of the American Chemical Society,* 2006. 128: p. 8148-8149

[76] D. T. Schoen, C. Xie and Y. Cui, Electrical Switching and Phase Transformation in Silver Selenide Nanowires, *Journal of the American Chemical Society,* 2007. 129: p. 4116-4117

[77] S.-H. Lee, D.-K. Ko, Y. Jung and R. Agarwal, Size-dependent phase transition memory switching behavior and low writing currents in GeTe nanowires, *Applied Physics Letters,* 2006. 89: p. 223116-3

[78] C. Woo Yeong, C. Beak-Hyung, C. Byung-Gil, O. Hyung-Rok, K. Sangbeom, K. Ki-Sung, K. Kyung-Hee, K. Du-Eung, K. Choong-Keun, B. Hyun-Geun, H. Youngnam, S. Ahn, K. Gwan-Hyeob, J. Gitae, J. Hongsik and K. Kinam, A 0.18-μm 3.0-V 64-Mb nonvolatile phase-transition random access memory (PRAM), *Solid-State Circuits, IEEE Journal of,* 2005. 40: p. 293-300

[79] J. S. Lee, S. Brittman, D. Yu and H. Park, Vaporr-Liquid-Solid and Vapor-Solid Growth of Phase-Change $Sb_2Te_3$ Nanowires and $Sb_2Te_3$/GeTe Nanowire Heterostructures, *Journal of the American Chemical Society,* 2008. 130: p. 6252-6258

[80] Y. S. Park, S. Y. Lee, S. M. Yoon, S. W. Jung, B. G. Yu, S. J. Lee and S. G. Yoon, Nonvolatile programmable metallization cell memory switching element based on Ag-doped SbTe solid electrolyte, *Applied Physics Letters,* 2007. 91: p. 162107-3

[81] K. Kin-Fu, L. Chain-Ming, C. Ming-Jung, T. Ming-Jinn and C. Tsung-Shune, $Ga_2Te_3Sb_5$ - A Candidate for Fast and Ultralong Retention Phase-Change Memory, *Advanced Materials,* 2009. 21: p. 1695-1699

# CHAPTER 2

# Three Dimensional Antimony Telluride Nanocomposite

## 2.1 Electrochemical Analysis of Antimony Telluride

### 2.1.1 Abstract

Electrochemical quartz crystal microbalance (EQCM) and rotating disk electrode (RDE) techniques were utilized to systematically investigate the electrodeposition of $Sb_xTe_{1-x}$ ($0.1 < X < 0.8$). In addition, the effect of applied potential and agitation were correlated to the material composition, crystal structure, and morphology. Although the composition was independent of the agitation rate, the deposition rate, current efficiency, crystallinity and phase of $Sb_xTe_{1-x}$ were all strongly influenced by it. The deposition rate monotonically increased with increases in the rotation rate because of the faster diffusion rate of $HTeO_2^+$ ions to the cathode. Amorphous $Sb_2Te_3$ was electrodeposited in the absence of agitation, whereas polycrystalline $Sb_2Te_3$ with elemental Sb and Te was co-deposited at a higher agitation independent of the applied deposition potential.

### 2.1.2 Introduction

Antimony telluride ($Sb_2Te_3$) is a narrow band-gap semiconductor (Eg = 0.3 eV) with a rhombohedral crystal structure belonging to the space group $R\bar{3}m$, consisting of alternating layers of Sb and Te perpendicular to the threefold axis. Due to its unique crystal structure and properties, it has many potential applications including a stable ohmic back contact in high efficiency solar cell devices [1, 2], p-type legs for

thermoelectric power generators and coolers operating at near room temperature [3-6] and non-volatile phase change memory devices because of its ability to reversibly transform between amorphous to crystalline states [7-9].

Antimony telluride has been synthesized by many different techniques including thermal evaporation [4, 10], sputtering [1], molecular beam epitaxy (MBE) [3], metal-organic chemical vapor deposition (MOCVD) [6], hydrothermal/solvothermal synthesis [11, 12] and electrodeposition [13-16]. Among them, electrodeposition is an especially attractive method to synthesize $Sb_2Te_3$, since it is able to rapidly deposit films with controlled morphology, dimension, and crystal structure in a cost effective manner at near ambient conditions. Although the electrodeposition of other chalcogenides such as $Bi_2Te_3$, PbTe, CdTe and CdS has been intensively studied [17-27], few works have been reported on $Sb_xTe_{1-x}$ electrodeposits. Leimkühler et al. demonstrated the ability to form $Sb_xTe_{1-x}$ thin films on indium tin oxide (ITO) substrates from acidic chloride baths with $SbCl_3$ and $TeO_2$ as metal ion precursors [13]. Wang et al. electrodeposited $Sb_2Te_3$ thin films on Si and Ag substrates from acidic chloride baths, where they observed the effects of the substrates on the microstructures of the $Sb_xTe_{1-x}$ thin films [16]. Huang et al. electrodeposited $Sb_xTe_{1-x}$ thin films from acidic nitrate baths on physical vapor deposited TiN substrates, where they added sodium citrate to the electrolyte to form Sb-citrate complexes in order to enhance the Sb solubility in aqueous solution [14].

In this work, detailed electroanaltyical studies were performed to understand the deposition mechanism of $Sb_xTe_{1-x}$ from acidic nitrate-tartrate baths. The effect of various deposition conditions (i.e., solution composition, agitation, applied potential, operating

temperature) on the deposition rate, current efficiency, material composition, morphology, and crystal structure were systematically investigated. The electroactive species and the electrochemical interaction between them were investigated using EQCM. Rotating disk electrodes were employed to investigate the mass transfer effects. The crystal structures and morphologies of the electrodeposited $Sb_xTe_{1-x}$ films were analyzed by X-ray diffraction (XRD) patterns and scanning electron microscopy (SEM).

### 2.1.3 Experimental

The electrolytes were prepared by separately dissolving $TeO_2$ (99.9995%, Alfa Aesar, Inc.) in concentrated nitric acid and $Sb_2O_3$ (99.9%, Fisher sci.) in L-tartaric acid (99.9%, Fisher sci.) solutions. Once the oxides were completely dissolved, the solutions were mixed to prepare electrolytes consisting of 0.01 M $HTeO_2^+$, 0.02 M $SbO^+$, 0.5 M L-tartaric acid and 1 M $HNO_3$. The solution pH was approximately 0.08.

All of the experiments were carried out in a 100 ml electrochemical cell with a three electrode configuration with an Ag/AgCl (sat. KCl) electrode and a platinum-coated electrode as the reference and counter electrodes, respectively. A quartz crystal microbalance (QCM) (RQCM, MAXTEX, Inc.) in conjunction with linear sweep voltammetry (LSV) was used to investigate the electroanalytic studies of SbxTe1-x electrodeposition using polished Au coated quartz crystals (MAXTEX, Inc.) as the working electrodes in the absence of stirring. The operating temperature was varied from 23$^o$C to 50$^o$C. The scan rate was fixed at 1 mV/sec.

Commercial Au micro electrodes (0.2 cm in diameter, CH Instruments) and in-house fabricated Au-coated copper macro electrodes (1.27 cm in diameter) were used as rotating disk electrodes to determine the mass transfer effects. In addition, $Sb_xTe_{1-x}$ films were potentiostatically deposited on Au rotating disk electrodes to analyze the current efficiency and morphology / crystallinity. The mass of each element (i.e. Sb and Te) in the films was determined by atomic absorption spectroscopy (AAS) (AAnalyst 800, Perkin Elmer). The current efficiencies and average partial current densities of $H_2$, Te, and Sb were calculated based on the reported procedure [14, 28]. For example, the current efficiency was determined using equation 2.1, where the mass of each element (i.e. Sb and Te) was determined using atomic absorption spectroscopy (AAS).

$$Current\ Efficiency = \frac{Actual\ mass\ of\ deposits}{Theoretical\ mass\ calculated\ from\ Faraday's\ law} \times 100(\%) \qquad \text{Equation 2.1}$$

The average partial current densities of the elements (i.e., Te and Sb) were determined from the deposited mass using equation 2.2;

$$i_{Te} = massTe^* n^* F / (MW_{Te} ^*A^* t) \qquad \text{Equation 2.2}$$

where $i_{Te}$ is the average partial current density of Te, massTe is the deposited mass of tellurium, n is the number of electron (n = 4 for Te electrodeposition), F is the Faraday constant, A is the deposited area, and t is the deposition time. The average partial current

density of $H_2$ evolution was estimated by subtracting the average partial current densities of the elements from the total average applied current density (Equation 2.3);

$$i_{H2} = i_{Tot} - i_{Te} - i_{Sb} \qquad \text{Equation 2.3}$$

where $i_{H2}$ is the average partial current density of $H_2$, $i_{Tot}$ is the average total current density, and $i_{Sb}$ is the partial current density of Sb. The film composition of the rotating disk electrodes was also confirmed by energy dispersive spectroscopy (EDS). XRD (X-ray diffractometer (D8 Advanced Diffractometer, Bruker) and SEM (XL30-FEG, Phillips) were utilized to determine the crystal structure and the morphology of the films, respectively.

### 2.1.4 Results and Discussion

$Sb_2Te_3$, like other chalcogenide compounds (i.e. $Bi_2Te_3$ and PbTe), is usually electrodeposited under diffusion control [14, 17-20] due to the low solubility of $HTeO_2^+$ ions in the aqueous solutions. To increase the solubility of $HTeO_2^+$, the pH of the electrolytes was kept low (pH of 0.08). In addition, a complexing agent such as L-tartaric acid was added to solubilize the $SbO^+$ ions. Figure 2.1 shows the electrochemical quartz crystal microbalance (EQCM) responses during the linear sweep voltammetry (LSV). To determine the deposition potential and deposition rate of the individual elements, three different electrolytes ((A) 0.01 M $HTeO_2^+$, 0.5 M L-$C_4H_6O_6$, and 1 M $HNO_3$, (B) 0.02 M $SbO^+$, 0.5 M L-$C_4H_6O_6$, and 1 M $HNO_3$, (C) 0.01 M $HTeO_2^+$, 0.02 M $SbO^+$, 0.5 M L-

$C_4H_6O_6$, and 1 M $HNO_3$) were studied in the absence of agitation. The EQCM-based deposition rate was calculated from the frequency change in the quartz crystal using equation 2.4, where $C_f$, $\Delta f$, and $\Delta m$ are the sensitivity factor of the crystal, frequency change and change in mass per unit area, respectively.

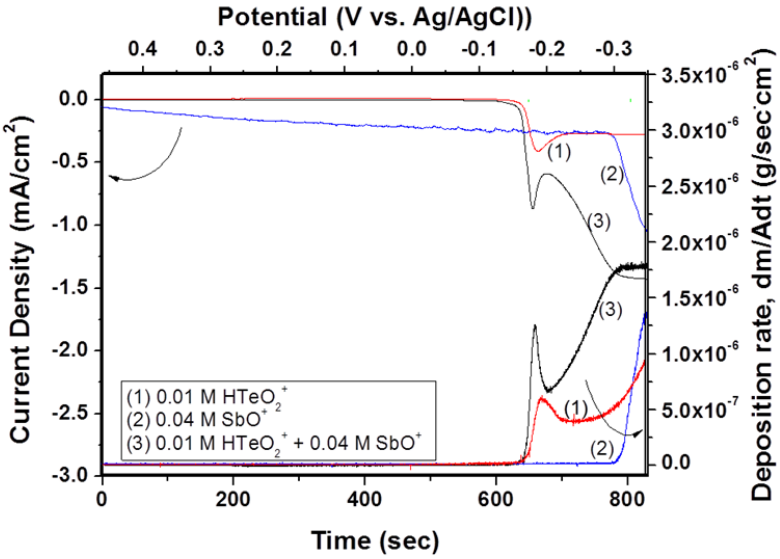


**Figure 2.1**: Deposition rate of electroactive species and current density during linear sweep voltammetry using an electrochemical quartz crystal microbalance system: Solution A (red): 0.01 M $HTeO_2^+$, 0.5 M L-tartaric acid and 1M $HNO_3$, Solution B (blue): 0.04 M $SbO^+$, 0.5 M L-tartaric acid and 1M $HNO_3$, Solution C (black): 0.01 M $HTeO_2^+$, 0.04 M $SbO^+$, 0.5 M L-tartaric acid and 1M $HNO_3$. The scan rate and operating temperature were fixed at 1 mV/s and 23$^o$C, respectively.

$$\Delta f = -C_f \times \Delta m \qquad \text{Equation 2.4}$$

As shown in Figure 2.1, the reduction current wave and the increase in frequency of the quartz crystal starting from -0.17 V (vs. Ag/AgCl) in solution A indicated that Te is overpotentially electrodeposited (OPD), which can be described by equation 2.5:

$$HTeO_2^+ + 3H^+ + 4e^- \rightarrow 2H_2O + Te$$
$$E^0 = 0.353 - 0.0443\,pH + 0.0148\log(HTeO_2^+) \quad (vs.NHE)$$ Equation 2.5

Similarly, the reduction current wave and the increase in frequency of the quartz crystal starting from -0.3 V (vs. Ag/AgCl) in solution B indicated that Sb is OPD, which can be described by equation 2.6:

$$SbO^+ + 2H^+ + 3e^- \rightarrow Sb + H_2O$$
$$E^0 = 0.212 - 0.0394\,pH + 0.0197\log(SbO^+) \quad (vs.NHE)$$ Equation 2.6

The electrodeposition of elemental Te and Sb thin films from solutions A and B, respectively, were confirmed by AAS analysis.

Underpotential deposition (UPD) of Sb on OPD Te was observed by comparing the LSVs from solutions A and C. Since solution C contains both $HTeO_2^+$ and $SbO^+$, whereas solution A contains only $HTeO^+$, the difference in current densities between the LSVs at the applied potential ranged from -0.17 to -0.3 V vs Ag/AgCl can be attributed to the UPD deposition of Sb on Te to form $Sb_2Te_3$ (Equation 2.7).

$$2SbO^+ + 3Te + 4H^+ + 6e^- \rightarrow Sb_2Te_3 + 2H_2O \quad [UPD]$$ Equation 2.7

Unlike the OPD of Sb, the UPD of Sb on Te can occur at lower applied potentials than the OPD of Sb because of the negative Gibbs free energy of $Sb_2Te_3$ formation ($\Delta G_f$ = -

57.5 KJ/mol) (Equation 2.7), where the $Sb_2Te_3$ intermetallic compound is formed by alternating depositions of Te and Sb layers [29, 30]. The overall electrochemical reaction of $Sb_2Te_3$ formation is described in equation 2.8.

$$2SbO^+ + 3HTeO_2^+ + 13H^+ + 18e^- \rightarrow Sb_2Te_3 + 8H_2O$$ Equation 2.8

To investigate the effects of mass transfer and deposition potential on the reaction kinetics and film composition, rotating disk electrodes were employed. As shown in Figure 2.2 (a), the LSVs as a function of agitation speed show an increase in limiting current density with increasing agitation speed from 0 to 5000 rpm, which indicates that the diffusion rate of the electroactive species increases with increases in the agitation speed. The mass transfer limited electrodeposition of $Bi_2Te_3$, PbTe, and $Sb_2Te_3$ has been reported by others where the diffusion has been limited by $HTeO_2^+$ [13, 14, 18]. Linear variation of the limiting current densities as a function of the square root of the rotation rates confirmed that the reaction is limited by mass transfer (Figure 2.2 (b)). In addition, the diffusion coefficient of $HTeO_2^+$ was calculated to be approx. $3.1 \times 10^{-6}$ $cm^2/sec$ from the fitted slope where the kinematic viscosity of the solution was assumed to be equal to water. The computed diffusion coefficient was lower compared to literature data which might be from an incorrect assumption [18, 19]. Since the kinematic viscosity of the solution is expected to be greater than that of pure water due to the presence of tartaric acid, the calculated result underestimated the diffusion coefficient of $HTeO_2^+$.

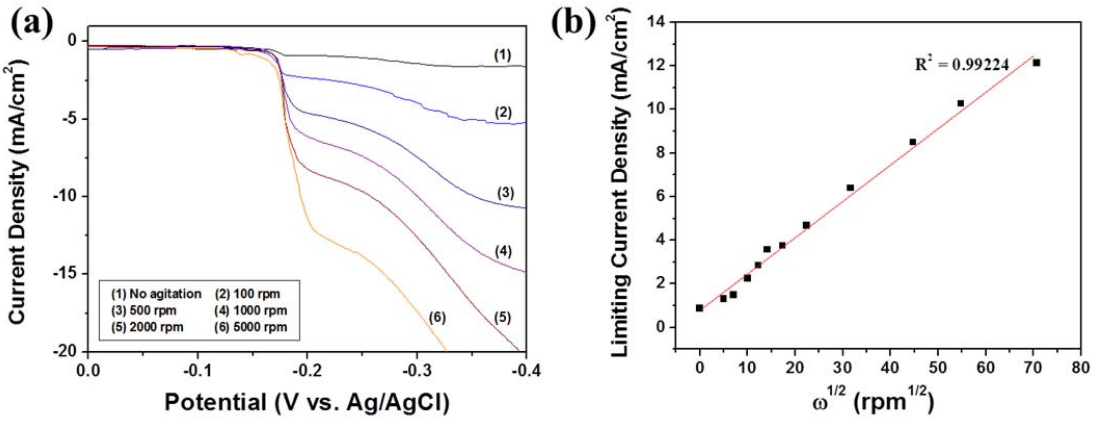


**Figure 2.2:** LSV curves as a function of agitation speed (a) and the limiting current density versus square root of agitation rate (b). The electrolyte consisted of 0.01 M $HTeO_2^+$, 0.02 M $SbO^+$, 0.5 M L-tartaric acid and 1M $HNO_3$. The scan rate and operating temperature were fixed at 1 mV/s and 23$^o$C, respectively.

The applied potential dependence of $Sb_xTe_{1-x}$ film composition (a), current efficiency (b) and the average partial current densities of Te (c), Sb (d), and $H_2$ (e) at different agitation rates are shown in Figure 2.3. As shown in Figure 2.3 (a), Te-rich $Sb_2Te_3$ thin films were electrodeposited at E > -0.17 V vs. Ag/AgCl whereas Sb-rich $Sb_2Te_3$ were obtained when E < -0.20 V vs. Ag/AgCl. The detailed deposition mechanism can be understood from the partial current densities. As shown in Figure 2.3 (c), the average Te partial current density increased with increases in the agitation at a given applied potential and reached a limiting current density at approx. E = -0.20 V vs. Ag/AgCl. The average Sb partial current density also increased with increased agitation at a given applied potential and monotonically increased with increased applied potential up to E = -0.35 V vs. Ag/AgCl at a given agitation rate, whereas the average partial current of $H_2$ was mainly dependent on the applied potential (Figure 2.3 (e)). The

increase in the average partial current densities of Te and Sb as a function of agitation at a low applied cathodic potential range (E > -0.17 V vs. Ag/AgCl) can be explained by an enhanced diffusion rate of $HTeO_2^+$ ions to the cathode due to a reduction of the diffusion boundary layer and by a proportional increase in the UPD of Sb on Te. Unlike Te deposition, which reached a limiting current density, the average Sb partial current density continued to increase at a high applied cathodic potential (E< -0.30 V vs. Ag/AgCl) because of the OPD of Sb in addition to the UPD of Sb, which agrees with the EQCM and LSV results. As shown in Figure 1, the UPD of Sb on Te to form $Sb_2Te_3$ is dominant when the applied potential is between -0.17 V to -0.3 V (vs. Ag/AgCl). As the deposition potential become more cathodic (E< -0.3 V vs. Ag/AgCl), the OPD of Sb started to occur in addition to the UPD of Sb. Thus, the Sb content increased monotonically with decreases in the applied potential. The enhancement of the current efficiency as a function of agitation can be explained by the significant increases in the deposition rates of Te and Sb compared to the $H_2$ gas evolution (Figure 2.3 (b)).

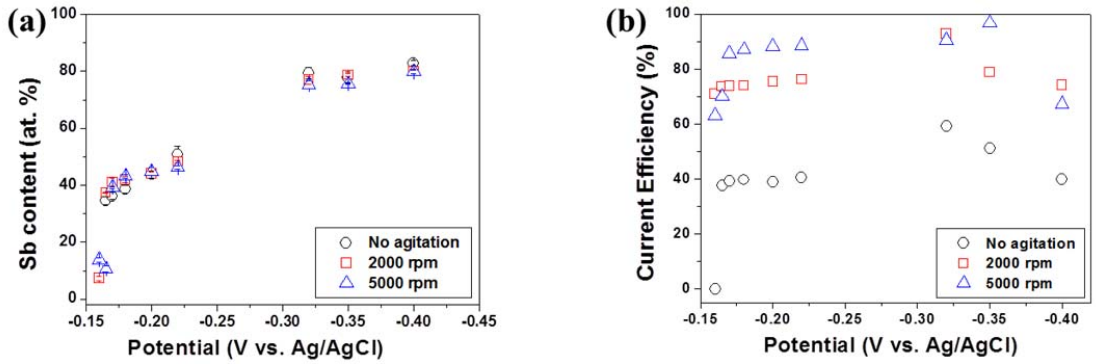

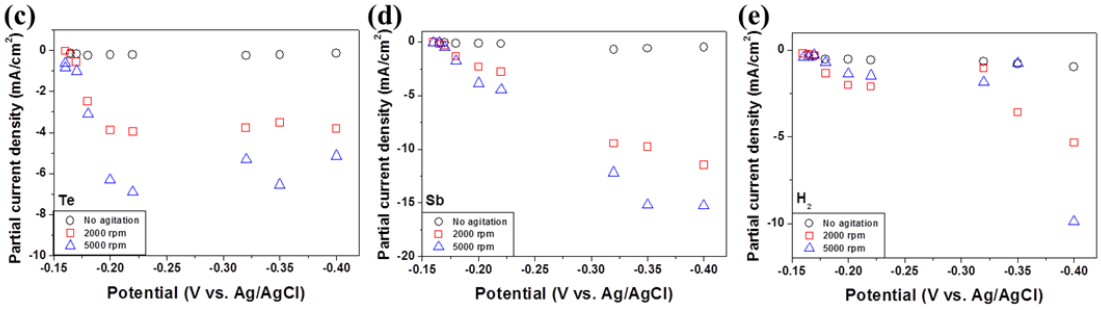


**Figure 2.3**: The applied potential dependent chemical composition (a), current efficiency (b), partial current density of Te (c), Sb (d) and $H_2$ (e) at different agitation speed. The electrolyte consisted of 0.01 M $HTeO_2^+$, 0.02 M $SbO^+$, 0.5 M L-tartaric acid and 1M $HNO_3$. The scan rate and operating temperature were fixed at 1 mV/s and 23°C, respectively. The average film thickness was fixed to be 1 micron.

The effect of the operating temperature on the electrodeposition of $Sb_xTe_{1-x}$ was investigated using linear sweep voltammograms at a fixed rotation rate of 5000 rpm (Figure 2.4 (a)). The reduction potential shifted towards a more anodic potential with an increase in the temperature, which can be explained by the Butler–Volmer equation [31]. The increase of the limiting current density is also expected because of larger diffusion coefficients for metal ions at high temperatures [18, 32]. The temperature dependent film composition followed the LSV curves (Figure 2.4 (b)). The temperature dependent current efficiencies and the average partial current densities of Te, Sb, and $H_2$ show similar trends with respect to the agitation effects except for the anodic shift in the deposition potential with an increase in temperature (Figure 2.4 (a)). In general, the current efficiency is expected to increase with elevations in temperature, but our data shows that the current efficiency at 50°C was slightly lower than those at 4°C and 23°C, which might be attributed to the chemical dissolution of the films during electrodeposition.

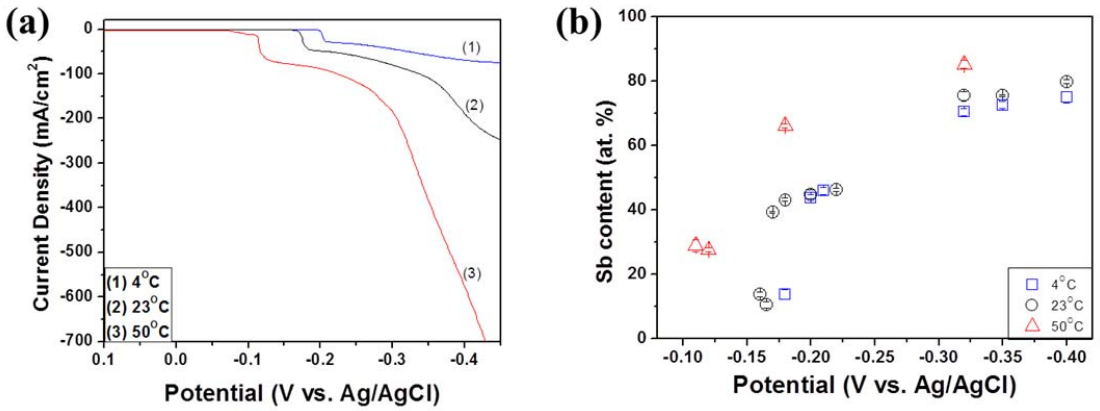


**Figure 2.4:** Temperature dependent LSV curves (a) and film composition (b). The electrolyte consisted of 0.01 M $HTeO_2^+$, 0.02 M $SbO^+$, 0.5 M L-tartaric acid and 1M $HNO_3$. The scan rate, the rotation speed and the average film thickness were fixed at 1mV/s, 5000 rpm and 1 μm, respectively.

Although the $Sb_xTe_{1-x}$ film composition was independent of the agitation speed, the crystal structure of the films can be varied depending on the agitation speed since the nucleation and growth of films are strongly dependent on reaction kinetics, which can be tailored by the agitation speed. Figure 2.5 shows the film morphologies of the deposits as a function of the agitation rate at fixed potentials of -0.17 V (a, b, c) and -0.32 V (d, e, f) vs. Ag/AgCl. At a fixed deposition potential of -0.17 V vs. Ag/AgCl, the film composition was nearly stoichiometric (Sb content of 37 ± 2 at. %), where the morphology shifted from nodular/granular to smooth and dense film as the agitation rate increased. At the deposition potential of -0.32 V vs. Ag/AgCl, Sb-rich thin films (77 ± 2 at. %) were electrodeposited and showed a cauliflower-like structure where the overall structure size increased with increased agitation speed. The agitation rate dependent crystal structures of the $Sb_xTe_{1-x}$ thin films were investigated using X-ray diffraction

patterns (Figure 2.6). Independent of the film composition, $Sb_xTe_{1-x}$ thin films deposited in the absence of agitation were amorphous. However, the crystallinity of the $Sb_xTe_{1-x}$ thin films improved with increases in the agitation speed, which is observed by the formation of sharp diffraction peaks. The crystallized films also show inclusions of elemental Sb and Te. In addition, the peak position of the (1 0 10) plane was also shifted with the increase in Sb content (inset of Figure 2.6) as demonstrated by Leimkühler *et al.*[13]. These observations clearly indicated that the crystal structure of $Sb_2Te_3$ thin films can be tuned by controlling the agitation rate.

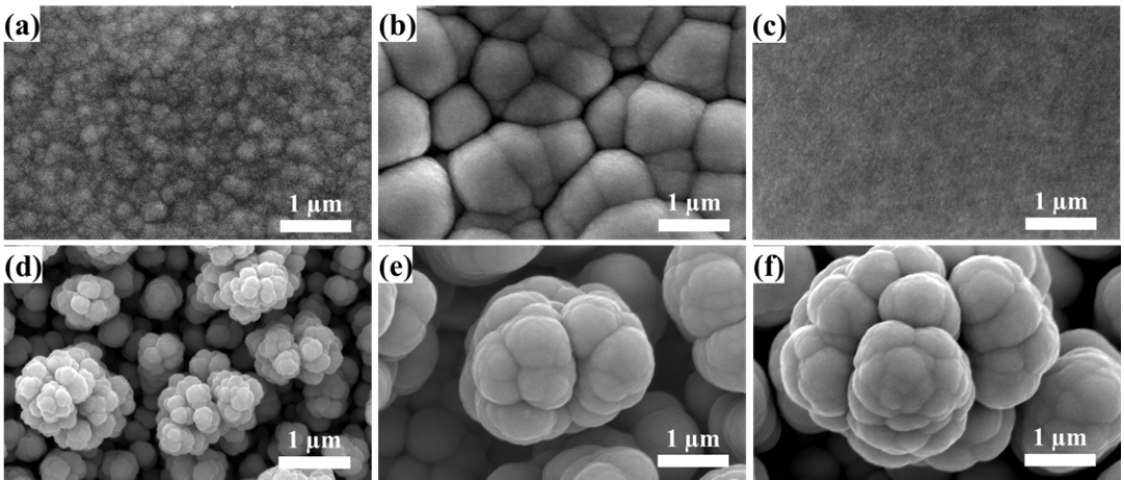


**Figure 2.5:** SEM images of $Sb_xTe_{1-x}$ electrodeposits at different potentials and agitations. The films deposited at -0.17 V vs Ag/AgCl (a,b,c) and at -0.32 V vs. Ag/AgCl (d,e,f): Unstirred (a,b), 2000 rpm (b, e) and 5000 rpm (c, f). The electrolyte consisted of 0.01 M $HTeO_2^+$, 0.02 M $SbO^+$, 0.5 M L-tartaric acid and 1M $HNO_3$. The scan rate, the bath temperature and the average film thickness were fixed at 1mV/s, 23 $^oC$ and 1 µm, respectively.

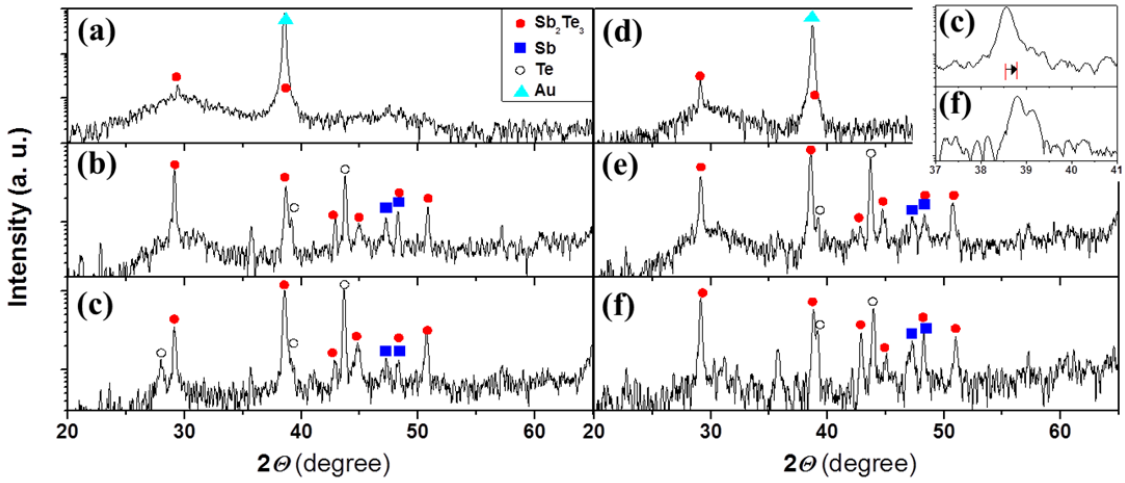


**Figure 2.6:** X-ray diffraction patterns of $Sb_xTe_{1-x}$ electrodeposits at different potentials and agitations. The films deposited at -0.17 V vs Ag/AgCl (a, b, c) and at -0.32 V vs. Ag/AgCl (d, e, f): Unstirred (a, d), 2000 rpm (b, e) and 5000 rpm (c, f). The electrolyte consisted of 0.01 M $HTeO_2^+$, 0.02 M $SbO^+$, 0.5 M L-tartaric acid and 1M $HNO_3$. The scan rate was fixed at 1 mV/s. The average film thickness was fixed to be 1 micron. Inset: the peak shift of (1 0 10) plane of $Sb_2Te_3$ thin films electrodeposited with 5000 rpm at -0.17 V and -0.32 V vs. Ag/AgCl. The deposition temperature was fixed at 23°C.

### 2.1.5 Conclusions

Various electroanaltyical techniques were utilized to determine the deposition mechanism of $Sb_xTe_{1-x}$ thin films at different deposition conditions. Moreover, the morphologies and crystal structures of the films were analyzed by SEM and XRD. At low cathodic potentials (-0.17 to -0.3 V vs. Ag/AgCl), the electrodeposition of Sb is predominately governed by underpotential deposition. As the deposition potential became more negative (E < -0.3 V vs. Ag/AgCl), Sb is deposited by both underpotential and overpotential deposition. The current efficiency was enhanced by increasing the agitation speed because of a greater diffusion rate of $HTeO_2^+$. Due to the chemical dissolution of $Sb_xTe_{1-x}$ thin films during deposition, lower current efficiencies were observed with

increases in operating temperature. In addition, the crystal structure of electrodeposited $Sb_xTe_{1-x}$ was "tailored" from amorphous to polycrystalline films by controlling the deposition rate.

### 2.1.6 References


[1] N. Romeo, A. Bosio, R. Tedeschi, A. Romeo, and V. Canevari, *Sol. Energy Mater. and Sol. Cells* 58 (1999) 209.

[2] A. E. Abken and O. J. Bartelt, *Thin Solid Films* 403-404 (2002) 216.

[3] Y. Kim, A. DiVenere, G. K. L. Wong, J. B. Ketterson, S. Cho, and J. R. Meyer, *J. Appl. Phys*. 91 (2002) 715.

[4] V. D. Das and N. Soundararajan, *J. Appl. Phys*. 65 (1989) 2332.

[5] F. Xiao, B. Yoo, K.-H. Lee, and N. V. Myung, *Nanotechnology* 18 (2007) 335203.

[6] A. Giani, A. Boulouz, F. Pascal-Delannoy, A. Foucaran, A. Boyer, B. Aboulfarah, and A. Mzerd, *J. Mater. Sci. Lett*. 18 (1999) 541.

[7] M. Wuttig and N. Yamada, *Nature Mater.* 6 (2007) 824.

[8] M. H. R. Lankhorst, B. W. S. M. M. Ketelaars, and R. A. M. Wolters, *Nature Mater*. 4 (2005) 347.

[9] S.-H. Lee, Y. Jung, and R. Agarwal, *Nature Nanotech*. 2 (2007) 626.

[10] H. Zou, D. M. Rowe, and G. Min, *J. Vac. Sci. & Technol*. A 19 (2001) 899.

[11] W. Shi, J. Yu, H. Wang, and H. Zhang, *J. Am. Chem. Soc*. 128 (2006) 16490.

[12] W. Wang, B. Poudel, J. Yang, D. Z. Wang, and Z. F. Ren, *J. Am. Chem. Soc*. 127 (2005) 13792.

[13] G. Leimkuhler, I. Kerkamm, and R. Reineke-Koch, *J. Electrochem. Soc*. 149 (2002) C474.

[14] Q. Huang, A. J. Kellock, and S. Raoux, *J. Electrochem. Soc*. 155 (2008) D104.

[15] K. Park, F. Xiao, B. Y. Yoo, Y. Rheem, and N. V. Myung, *J. Alloys & Comp*. 485 (2009) 362.

[16] C. Wang, Q. Wang, L. Chen, X. Xu, and Q. Yao, *Electrochem. & Solid-State Lett*. 9 (2006) C147.

[17] B. Y. Yoo, C. K. Huang, J. R. Lim, J. Herman, M. A. Ryan, J. P. Fleurial, and N. V. Myung, *Electrochim. Acta* 50 (2005) 4371.

[18] F. Xiao, B. Yoo, M. A. Ryan, K.-H. Lee, and N. V. Myung, *Electrochim. Acta* 52 (2006) 1101.

[19] A. Saraby-Reintjes, L. M. Peter, M. E. Özsan, S. Dennison, and S. Webster, *J. Electrochem. Soc*., 140 (1993) 2880

[20] M. C. Kum, B. Y. Yoo, Y. W. Rheem, K. N. Bozhilov, W. Chen, A. Mulchandani, and N. V. Myung, *Nanotechnology* 19 (2008) 325711.

[21] M. S. Martin-Gonzalez, A. L. Prieto, R. Gronsky, T. Sands, and A. M. Stacy, *J. Electrochem. Soc.* 149 (2002) C546.

[22] M. Takahashi, Y. Muramatsu, T. Suzuki, S. Sato, M. Watanabe, K. Wakita, and T. Uchida, *J. Electrochem. Soc.* 150 (2003) C169.

[23] L. Beaunier, H. Cachet, R. Cortes, and M. Froment, *J. Electroanal. Chem*. 532 (2002) 215.

[24] M. P. R. Panicker, M. Knaster, and F. A. Kroger, *J. Electrochem. Soc.* 125 (1978) 566.

[25] A. W. Zhao, G. W. Meng, L. D. Zhang, T. Gao, S. H. Sun, and Y. T. Pang, *Appl. Phys. A* 76 (2003) 537.

[26] D. Xu, Y. Xu, D. Chen, G. Guo, L. Gui, and Y. Tang, *Chem. Phys. Lett.* 325 (2000) 340.

[27] C. Lepiller, P. Cowache, J. F. Guillemoles, N. Gibson, E. san, and D. Lincot, *Thin Solid Films* 361-362 (2000) 118.

[28] C. Fan and D. L. Piron, *Electrochim. Acta* 41 (1996) 1713

[29] A. Saraby-Reintjes, L. M. Peter, M. E. Özsan, S. Dennison, and S. Webster, *J. Electrochem. Soc*., 140 (1993) 2880

[30] D. M. Rowe, *CRC Handbook of Thermoelectrics*. CRC Press, Inc.: Boca Raton, 1995

[31] M. Saitou, S. Oshiro, and S. Asadul Hossain, *J. Appl. Electrochem*. 38 (2008) 309.

[32] Q. Zhang, Y. Hua, T. Dong, and D. Zhou, *J. Appl. Electrochem*. 39 (2009) 1207.

## 2.2 Thermoelectric Properties of Electrodeposited Antimony Telluride Nanocomposites

### 2.2.1 Abstract

Temperature dependent thermoelectric properties (electrical resistivity (ρ), Seebeck coefficient (S) and power factor ($S^2\sigma$)) of antimony telluride ($Sb_xTe_{1-x}$) electrodeposits were investigated to optimize the properties by tailored morphology, composition and crystallinity of films, where the variation of thermoelectric properties was analyzed with the transition from amorphous to crystal phase of $Sb_xTe_{1-x}$ electrodeposits. Thermoelectric power factor of $Sb_xTe_{1-x}$ electrodeposits increased in the films with low electrical resistivity due to dense morphology. Seebeck coefficient of materials is a critical factor to improve thermoelectric property in the limit of interdependence between electrical conductivity and thermal conductivity. $Sb_xTe_{1-x}$ electrodeposits with the crystallinity tailored by different annealing temperature showed an abnormally enhanced Seebeck coefficient of 335μV/K, which was demonstrated by the nanocrystalline composite generated in annealing process. The electrodeposited $Sb_xTe_{1-x}$ nanocomposites demonstrated high thermoelectric power factor which result from even low electrical conductivity, compared to thermoelectric properties of single bulk crystal film. $Sb_xTe_{1-x}$ films with the improved thermoelectric properties were synthesized by a cost-effective and mass-productive electrodeposition technique.

### 2.2.2 Introduction

An energy crisis has been seriously concerned due to the current usage and high potential shortage of fossil fuel near in the future. Many researches have been implemented to utilize alternative resources. Thermoelectric power generator has been investigated, since it can generate electricity by harvesting wasted heat energy. However, thermoelectric devices have been applied to the limited fields due to their low efficiency. The improvement of the device efficiency has been restrained by stagnant properties (ZT~1) of thermoelectric materials. The properties were evaluated by thermoelectric figure of merit, $ZT= S^2\sigma T/k$, where S, σ, T and k are Seebeck coefficient, electrical conductivity, absolute temperature and thermal conductivity, respectively. Even though high Seebeck coefficient, high electrical conductivity and low thermal conductivity have been required to improve material properties as described in the equation, the improvement of thermoelectric properties has been limited by the interdependence of factors: electrical conductivity is linearly proportional to thermal conductivity (Wiedemann-Franz Law) and inversely proportional to Seebeck coefficient. Nowadays, the development of thermoelectric devices is invigorated to overcome the limit by advanced nanotechnologies. Enhanced thermoelectric properties of low dimensional materials were theoretically expected by classical and quantum mechanical size effect [1, 2]. Few thermoelectric materials such as nanowires [3, 4] and superlattices [5, 6] has demonstrated high figure of merits. Another approach to improve thermoelectric properties has been carried out by the development of thermoelectric nanocomposites [7, 8], since nanocomposites can be produced in cost-effective and mass-productive procedures compared to single crystal. Bed Poudel, et al. demonstrated ZT of 1.2 with

nanostructured bismuth antimony telluride bulk alloys of polycrystallinity [7]. However, the enhancement of thermoelectric properties in the demonstrated materials was mainly attributed to the reduced thermal conductivity due to the increased phonon scattering.

Antimony telluride chalcogenide semiconductors with narrow band gap of 0.3 eV has been of great interest owing to their potential applications as p-type materials for thermoelectric devices operating at near room temperature [9-12] and reversible phase transition materials for non-volatile phase change memory devices [13-15]. Especially, the reversible phase transition property of $Sb_xTe_{1-x}$ at low temperature below 373K is an inspiring subject in a view of thermoelectric property. However, few systematic studies on thermoelectric properties of antimony telluride depending on material crystallinity have been reported [16-19]. Temperature dependent thermoelectric properties of polycrystalline $Sb_2Te_3$ in wide temperature range and amorphous $Sb_2Te_3$ at low temperature without phase transition were investigated respectively. Even though V. Damordara Das, et al. observed the phase transition from amorphous to crystal structure of $Sb_2Te_3$ during the measurement of temperature dependent thermoelectric properties, thermoelectric properties of annealed polycrystalline $Sb_2Te_3$ depending on film thickness were investigated [20].

This work investigated temperature dependent electrical resistivity, Seebeck coefficient and power factor of $Sb_xTe_{1-x}$ electrodeposits. During a thermal cycle for measurement, amorphous $Sb_xTe_{1-x}$ electrodeposits displayed phase transition to crystalline. The thermoelectric properties of $Sb_xTe_{1-x}$ electrodeposits were determined by the tailored film compositions and morphologies. Seebeck coefficients of annealed

$Sb_xTe_{1-x}$ films were investigated depending on crystallinity tailored by annealing temperature. Drastically increased Seebeck coefficients of annealed $Sb_xTe_{1-x}$ electrodeposits were attributed to nanocomposites produced by annealing.

### 2.2.3 Experimental

The electrolytes were prepared by separately dissolving $TeO_2$ (99.9995%, Alfa Aesar, Inc.) in concentrated nitric acid and $Sb_2O_3$ (99.9%, Fisher sci.) in L-tartaric acid (99.9%, Fisher sci.) solution. Once the oxides were completely dissolved, the solutions were mixed to make electrolytes consisting of 0.01 M $HTeO_2^+$, 0.02 M $SbO^+$, 0.5 M L-tartaric acid and 1 M $HNO_3$. The solution pH was approximately 0.08.

All electrodepositions were carried out in 300 ml electrochemical cell with three electrode configuration using an Ag/AgCl (sat. KCl) reference electrode and platinum-coated titanium strip as a counter electrode. Glass slides as a substrate were polished to increase mechanical adhesion by an abrasive paper (Buehler, Grit 320/P400). $Sb_2Te_3$ seed layer with 150±52 nm thickness was thermally evaporated on the polished glass slides to produce an electrical contact for electrodeposition where $Sb_2Te_3$ (Alfa Aesar, 99.999%) were utilized as a source material. The thermally evaporated $Sb_2Te_3$ seed layer was annealed to improve electrical conductivity at 473 K for 1 hour in 5% $H_2/N_2$ (g). $Sb_xTe_{1-x}$ was potentiostatically deposited on thermally evaporated $Sb_2Te_3$ seed layer / glass slide at room temperature under parallel agitation of 1 Hz where the applied potentials were ranged from -0.20 V to -0.40 V (vs. Ag/AgCl).

Thermoelectric properties including electrical resistivity and Seebeck coefficient were measured using custom-made apparatus. The schematic diagram of the apparatus was illustrated in Figure 2.8 (a). In-plane electrical resistivity was measured by typical four point probes method, where inside two probes of them consist of T-type thermocouple microprobes (Physitemp Instrument Inc. 0.33mm). The distance between probes was fixed at 2 mm. Seebeck coefficients were determined by alternatively measured variation of voltage and temperature gradient between two thermocouple probes with nanovolt-meter (Keithley, 2182A) and multi-meter (Keithley, 2010) combined with a switching system (NI, USB-6008 DAQ). The temperature of the films was controlled by the heating band on the one end of the sample holder using DC power supply (Hewlett Packard, 6655A).

The film composition of $Sb_xTe_{1-x}$ electrodeposits was analyzed by energy dispersive spectroscopy (EDAX, Phoenix). XRD (X-ray diffractometer (D8 Advanced Diffractometer, Bruker), SEM (XL30-FEG, Phillips) and TEM (JEM-2100F, JEOL) were utilized to determine crystal structure and morphology of films, respectively.

### 2.2.4 Results and Discussion

Electrodeposition of antimony telluride on metallic substrates has been widely studied to investigate deposit conditions and physicochemical properties [21-24]. However, the measurement of thermoelectric properties requires the $Sb_xTe_{1-x}$ electrodeposits on an insulating substrate, since charge carriers should be transported in the channel of $Sb_xTe_{1-x}$, not a metallic substrate. Polished glass slides were then utilized

as a substrate of $Sb_xTe_{1-x}$ electrodeposits. Thin $Sb_2Te_3$ seed layer with thickness of 150±52 nm was thermally evaporated onto polished glass substrates, providing electrical contact as well as conductive surface for electrodeposition of $Sb_xTe_{1-x}$. $Sb_xTe_{1-x}$ films with 4300±1200 nm thickness were potentiostatically deposited at the applied potentials ranging from -0.2 V to -0.4 V (vs. Ag/AgCl) on $Sb_2Te_3$ seed layer / glass slide as a working electrode. SEM images in Figure 2.7 show the morphologies of $Sb_xTe_{1-x}$ electrodeposits where film compositions and morphologies were tailored by the applied potentials. Sb content of $Sb_xTe_{1-x}$ electrodeposits increased with more negative cathodic potential as analyzed in the previous work of chapter 2.2, while the morphologies of films were varied from dense films to nodular/granular films with the increased Sb content.

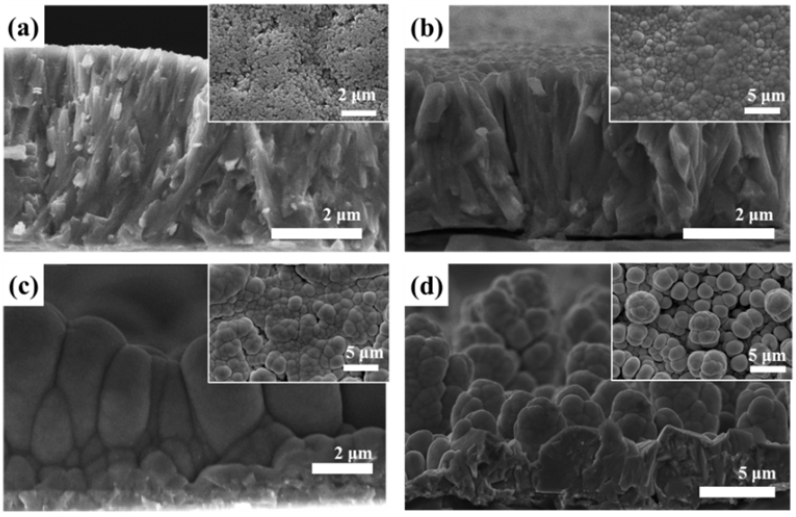


**Figure 2.7**: SEM images of $Sb_xTe_y$ electrodeposits with different film composition: Te (a), $Sb_{27}Te_{73}$ (b), $Sb_{39}Te_{61}$ (c) and $Sb_{50}Te_{50}$ (d) (inset: top views).

Thermoelectric properties of $Sb_xTe_{1-x}$ electrodeposits were measured along both ascending and descending temperature range using custom-made apparatus as displayed

in Figure 2.8 (a-b). Average temperatures of properties were estimated from plateau of temperature at fixed heater power (Figure 2.8 (c)). Seebeck coefficients were obtained from the variation ratio of voltage to temperature gradient at the plateau of temperature as shown in Figure 2.8 (d). Figure 2.9 shows temperature dependent electrical resistivity, Seebeck coefficients and power factors of $Sb_{26}Te_{74}$, $Sb_{39}Te_{61}$ and $Sb_{50}Te_{50}$ electrodeposits. Electrical resistivity of $Sb_xTe_{1-x}$ electrodeposits displayed drastic decrease during a thermal cycle due to the transition from amorphous to crystalline phase, and the crystallized $Sb_xTe_{1-x}$ electrodeposits did not display reversible transition from crystalline to amorphous phase without supercooling process. Temperature dependent electrical resistivity of $Sb_xTe_{1-x}$ electrodeposit described typical semiconducting behavior, and thermal activation energy was obtained from Arrhenius plot (Figure 2.10).

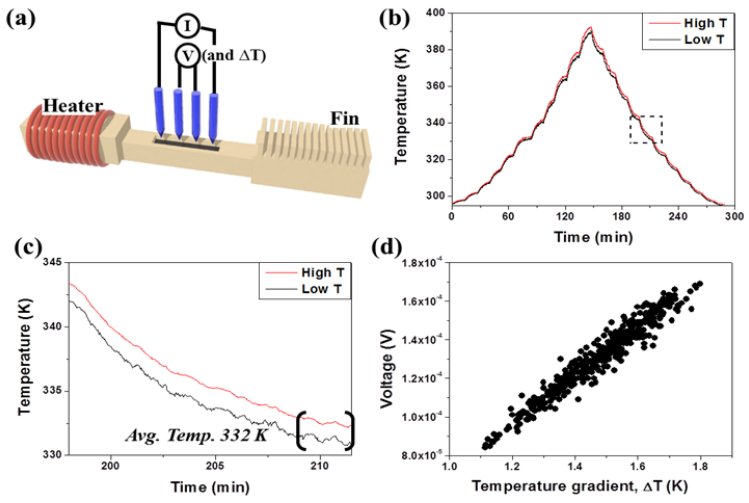


**Figure 2.8**: A schematic diagram of measurement system (a), the temperature in two thermocouples on $Sb_xTe_{1-x}$ films in the gradually heated and cooled aluminum substrate (b), the magnified plot of rectangular part of (b); Average temperature were obtained from plateau of temperature (c), and voltage versus temperature gradients between two thermocouple probes; Seebeck coefficients were estimated from the slope (d).

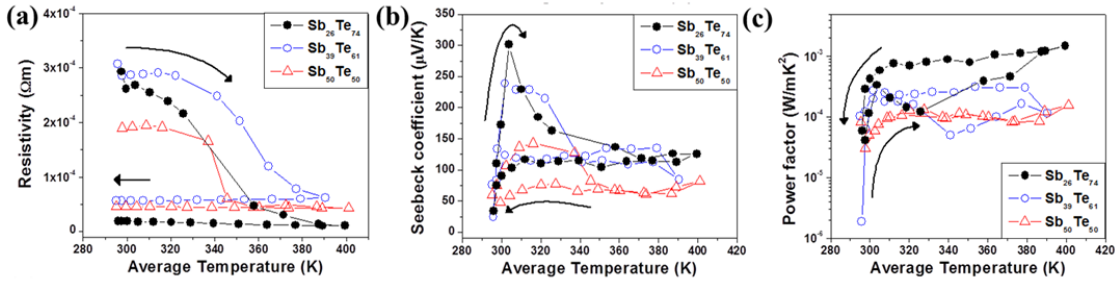


**Figure 2.9**: Temperature dependent electrical resistivity (a), Seebeck coefficient (b) and power factor (c) of $Sb_{26}Te_{74}$, $Sb_{39}Te_{61}$ and $Sb_{50}Te_{50}$ electrodeposits during a thermal cycle.

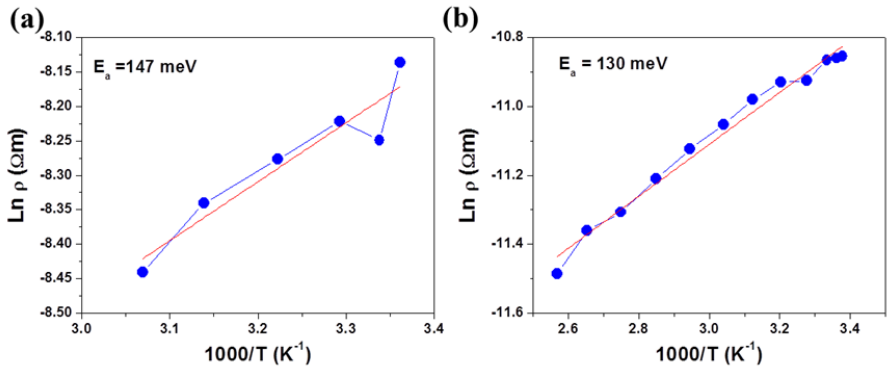


**Figure 2.10**: Temperature dependent electrical resistivity of as-deposited amorphous $Sb_{39}Te_{61}$ film (a) and polycrystal $Sb_{39}Te_{61}$ film after a thermal cycle (b); the thermal activation energies were calculated by Arrhenius plot.

The thermal activation energy of amorphous $Sb_{26}Te_{74}$ electrodeposit before phase transition was 147 meV, smaller than thermal activation energy (284 meV) of amorphous $Sb_2Te_3$ analyzed in the temperature range from 185 K to 295 K [19]. The thermal activation energy of 131 meV after phase transition by a thermal cycle was larger than the thermal activation energy of approximately 60 meV reported by V. D. Das *et al.* [20]. Seebeck coefficients of $Sb_xTe_{1-x}$ electrodeposits show abrupt increase and gradual decrease during heating, and steady decrease during cooling. The abnormal variation of Seebeck coefficient may be attributed to the variation of crystal structure. Power factors

of $S^2\rho$ were plotted based on the measurement of electrical resistivity and Seebeck coefficient. XRD patterns in Figure 2.11 correspond with the thermoelectric properties' analysis of $Sb_xTe_{1-x}$ electrodeposits. XRD pattern of as-deposited $Sb_{39}Te_{61}$ indicated amorphous structure, and the crystal structure was changed from amorphous to crystalline phase after a thermal cycle. Temperature dependent thermoelectric properties of annealed $Sb_2Te_3$ seed layer was described in Figure 2.12, where the annealed film didn't displayed the phase transition.

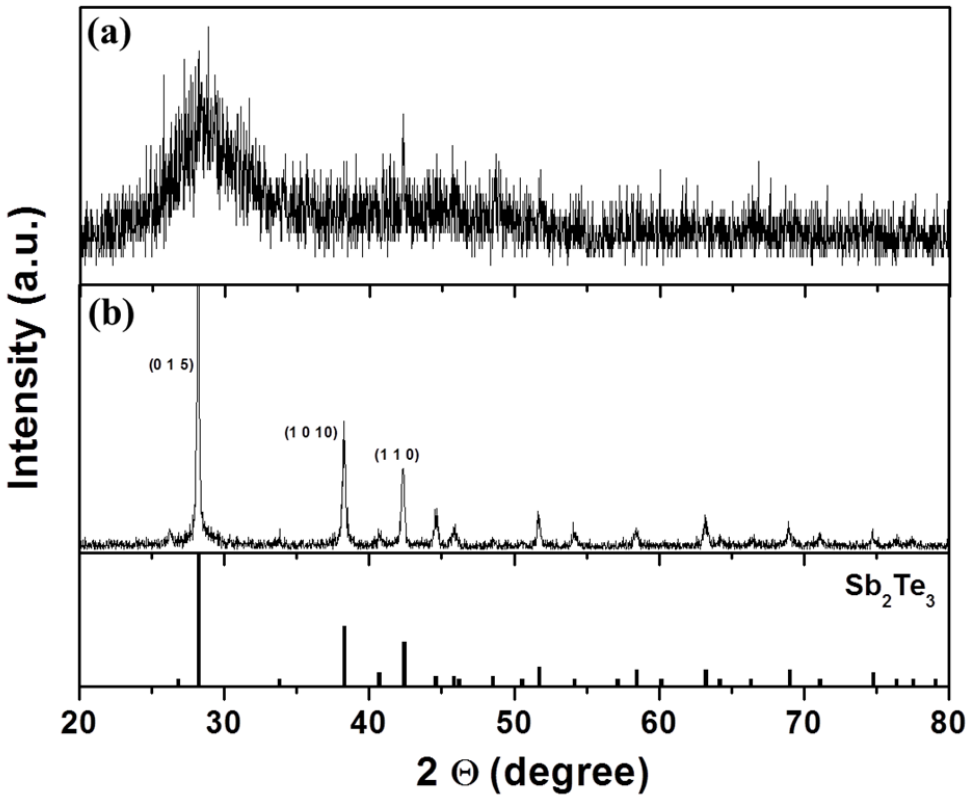


**Figure 2.11**: XRD patterns of $Sb_{39}Te_{61}$ electrodeposits: as-deposited (a) and after thermal cycled film (b). The maximum temperature was fixed at 391 K.

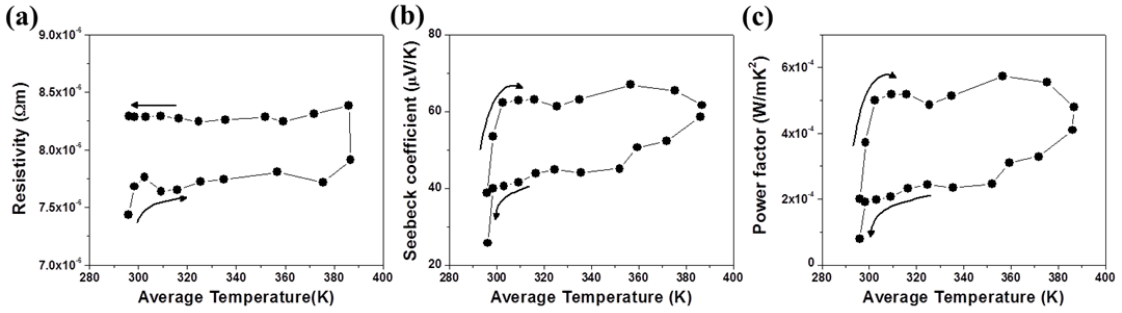


**Figure 2.12**: Temperature dependent thermoelectric properties of an annealed $Sb_2Te_3$ seed layer. Thermal evaporated $Sb_2Te_3$ deposit was annealed at 473 K for 1 hour in 5 % $H_2/N_2$ (g): electrical resistivity (a), Seebeck coefficient (b) and power factor (c).

Figure 2.13 described film composition dependent thermoelectric properties at 298 K and 373 K. Electrical resistivity of polycrystalline $Sb_xTe_{1-x}$ films after a thermal cycle was reduced rather than the resistivity of as-deposited $Sb_xTe_{1-x}$ films due to the improved crystallinity. A polycrystalline $Sb_{26}Te_{74}$ film demonstrated the lowest resistivity, which was expected by smooth and dense morphology compared to nodular/granular structures in $Sb_xTe_{1-x}$ films with high Sb contents. Among polycrystalline $Sb_xTe_{1-x}$ films measured at 298 K, a polycrystalline $Sb_{39}Te_{61}$ film with almost stoichiometric composition displayed a highest Seebeck coefficient. Based on the measured electrical resistivity and Seebeck coefficient, the calculated power factor indicated a highest value in a polycrystalline $Sb_{26}Te_{74}$ film with low electrical resistivity. The polycrystalline $Sb_xTe_{1-x}$ films after a thermal cycle were annealed to improve the crystallinity at 473 K for 1 hour in 5 % $H_2/N_2$ (g). The annealed $Sb_xTe_{1-x}$ films with the improved crystallinity showed the reduced electrical resistivity resulting in increased power factors. Temperature dependent thermoelectric properties of as-deposited and annealed $Sb_{50}Te_{50}$ film for a thermal cycle were compared in Figure 2.14.

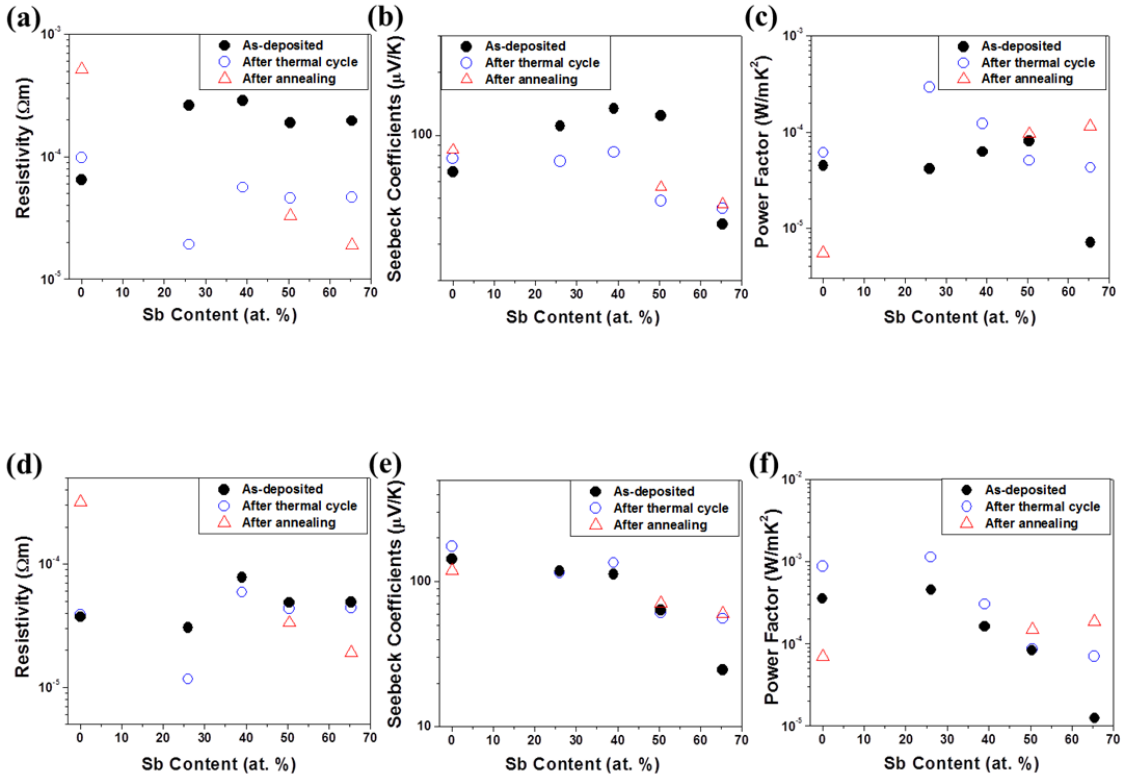


**Figure 2.13**: Film composition dependent thermoelectric properties of $Sb_xTe_{1-x}$ thin films at room temperature and 373 K: resistivity (a), Seebeck coefficient (b) and power factor (c) at room temperature, and resistivity (d), Seebeck coefficient (e) and power factor (f) at 373 K.

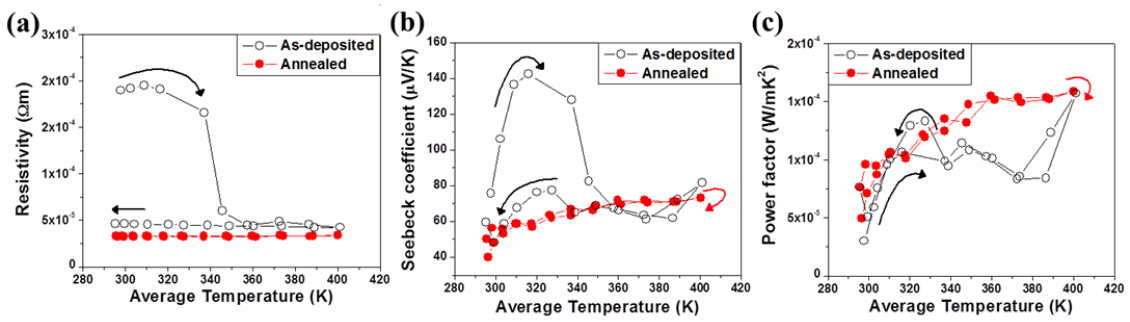


**Figure 2.14**: Comparison of thermoelectric properties of as-deposited and annealed $Sb_{50}Te_{50}$ thin film: The annealing was performed at 473 K for 1hr in 5% $H_2/N_2$ (g): electrical resistivity (a), Seebeck coefficient (b) and power factor (c).

Phase transition temperature and ratio of resistivity variation of $Sb_xTe_{1-x}$ electrodeposits were investigated as a function of film composition as shown in Figure 2.15, which were important factors to evaluate phase transition properties for a memory device application [13-15]. Even though the material composition of $Sb_7Te_3$ is known to show low transition temperature and high ratio of resistivity variation, $Sb_{26}Te_{74}$ electrodeposit demonstrated high ratio of resistivity variation in first thermal cycle. The smooth and dense morphology of $Sb_{26}Te_{74}$ electrodeposit may attribute to the property due to effective thermal conduction. However, the morphology and crystallinity of materials cannot be critical factors of memory device performance with the reversible phase transition during repeated thermal cycles, since the ratio of resistivity variation can be changed by sequent thermal cycles. Low transition temperature was demonstrated in $Sb_{65}Te_{35}$ electrodeposit which of composition is almost similar with $Sb_7Te_3$.

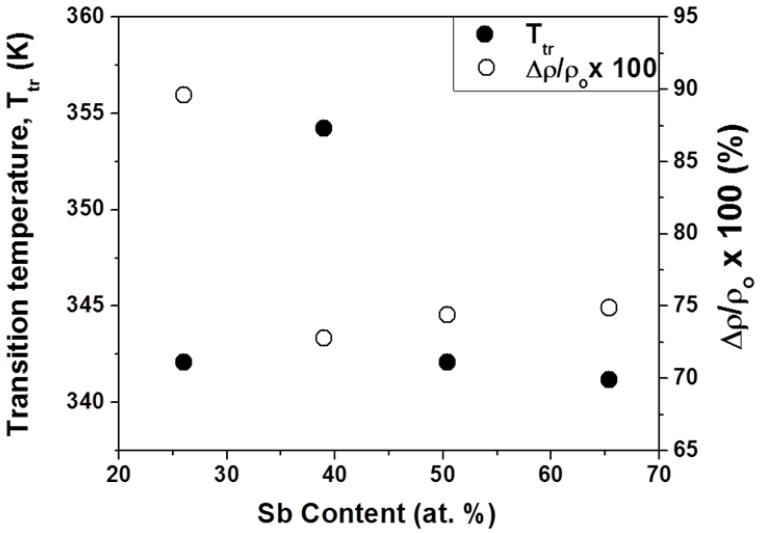


**Figure 2.15**: Chemical composition dependent phase transition temperature and resistivity variation ratio due to phase transition of $Sb_xTe_{1-x}$ thin films.

In addition, annealing effects of $Sb_{42}Te_{58}$ electrodeposits on thermoelectric properties were investigated by XRD analysis as shown in Figure 2.16. $Sb_xTe_{1-x}$ films was heated up on a measurement apparatus in order to directly compare to temperature dependent thermoelectric properties during a thermal cycle. The XRD pattern of a $Sb_{42}Te_{58}$ film annealed at 380 K was correctly accorded with a $Sb_2Te_3$ pattern (JCPDS #150874). The varied crystallinity of a $Sb_{42}Te_{58}$ film depending on annealing temperature was corresponded with the variation of electrical resistivity. As the annealing temperature increased, the peaks were developed by the crystallization of an amorphous $Sb_{42}Te_{58}$ film. Significantly, a peak of γ-SbTe in amorphous $Sb_{42}Te_{58}$ electrodeposit was developed during annealing at low temperature of 330 K and 350 K, which described the two different phases in a matrix. The phase separation of $Sb_{42}Te_{58}$ can be expected by phase diagram. The grain size of the $Sb_{42}Te_{58}$ film was characterized by analysis of (1 1 0) plane using Scherrer equation [25]. Texture coefficients (TC) were calculated to estimate the degree of preferred orientation using Harris method [26]. The grain size and texture coefficient of the $Sb_{42}Te_{58}$ film were described as a function of annealing temperature in Table 2.1. The peaks began to develop from the $Sb_{42}Te_{58}$ film annealed at 330 K, and the increased grain size was shown in $Sb_{42}Te_{58}$ film annealed at 380 K. Based on TC of the $Sb_{43}Te_{57}$ film, the crystallized film had the preferred orientation of (1 1 0) plane.

The phase separation of rhombohedral $Sb_2Te_3$ and γ-SbTe was shown in the $Sb_{42}Te_{58}$ electrodeposit annealed at 351 K. The TEM analysis of the $Sb_{42}Te_{58}$ electrodeposit scratched out from the film in Figure 2.17 illustrates the antimony telluride nanocomposite formed by the phase separation. The analyzed d-spacing of lattice planes

indicated the $Sb_2Te_3$ phase and γ-SbTe phase, which agrees with the XRD analysis of the annealed film. The amorphous phase of the $Sb_2Te_3$ electrodeposit remained after the annealing process as shown in the High resolution TEM (HRTEM) images. The crystalline γ-SbTe phase was embedded in the crystalline and amorphous $Sb_2Te_3$. HRTEM images confirm the embedded γ-SbTe and $Sb_2Te_3$ nanocrystalline of about 3 to 20 nm with high crystallinity.

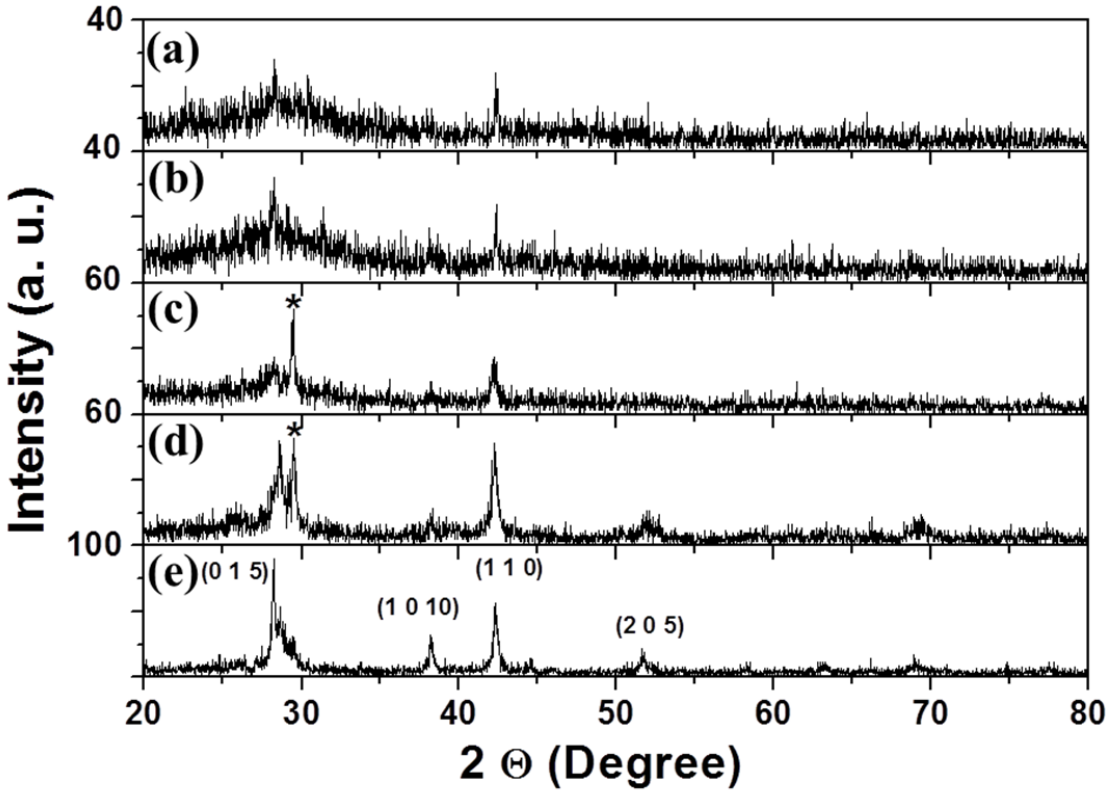


**Figure 2.16**: XRD patterns of $Sb_{42}Te_{58}$ electrodeposits at different annealing temperatures: 297 K (a), 311 K (b), 330 K (c), 351 K (d) and 380 K (e), The peak marked with an asterisk depicts (1 0 2) plane of Sb. A film was annealed for a thermal cycle on the measurement stage in air.

**Table 2.1**: Grain size and texture coefficient of $Sb_{42}Te_{58}$ electrodeposit depending annealing temperature by the analysis of XRD patterns.

| Annealing temperature | 297 K | 311 K | 330 K | 351 K | 380 K |
|---|---|---|---|---|---|
| FWHM (radian) | Amorphous | | 0.0079 | 0.0079 | 0.0058 |
| Grain size (nm) $SbTe_{(1\,1\,0)}$ | | | 19 | 19 | 25 |
| $TC_{(0\,1\,5)}$ | | | 0.42 | 0.51 | 0.68 |
| $TC_{(1\,0\,10)}$ | | | 0.75 | 0.51 | 0.69 |
| $TC_{(1\,1\,0)}$ | | | 1.83 | 1.98 | 1.63 |

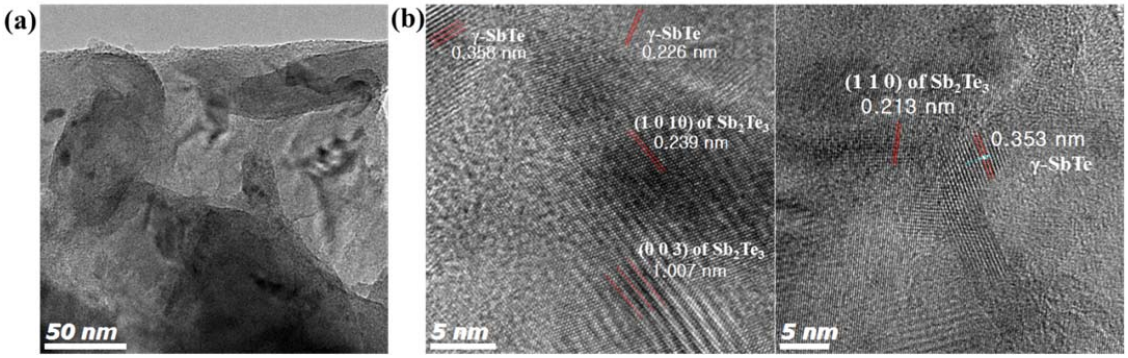


**Figure 2.17**: Brigh field TEM image (a) and HRTEM images (b) of the $Sb_{42}Te_{58}$ electrodeposit annealed at 351 K. The d-spacing of lattice planes was identified to the rhombohedral $Sb_2Te_3$ phase and γ-SbTe phase.

Thermoelectric properties of a $Sb_{42}Te_{58}$ film annealed at different temperature were investigated as shown in Figure 2.18. Electrical resistivity decreased with increasing annealing temperature, which results from the crystallization of a $Sb_{42}Te_{58}$ electrodeposit as shown in XRD analysis. The polycrystalline $Sb_{42}Te_{58}$ film demonstrated

approximately 2 orders larger electrical resistivity than single crystalline bulk $Sb_{33}Te_{67}$ due to more defects and increased surface boundary scattering [27]. However, the $Sb_{42}Te_{58}$ electrodeposit exhibited high Seebeck coefficients compared to single crystalline bulk $Sb_{33}Te_{67}$. Seebeck coefficients of the $Sb_{42}Te_{58}$ electrodeposit were increased with increasing annealing temperature, and especially, the film annealed at 351 K demonstrated a significantly enhanced Seebeck coefficient of 335μV/K. The Seebeck coefficient of $Sb_{42}Te_{58}$ electrodeposit annealed at 376 K was decreased. The drastically enhanced Seebeck coefficient corresponded with the inclusions of γ-SbTe phase in the $Sb_{42}Te_{58}$ electrodeposit as described in XRD and TEM analysis, which can be attributed to electron filtering effect [28-30] with high energy electrons for thermionic emission and Kondo effect [31-33] with sharp density of state. The enhanced Seebeck coefficient was decreased by dissolution of γ-SbTe phase in the developed crystallinity of $Sb_2Te_3$ at 376 K, corresponding with the reduction of γ-SbTe peak in XRD pattern. High thermoelectric power factor of $Sb_xTe_{1-x}$ films with tailored crystallinity can be realized by the drastic increase of Seebeck coefficients accompanied with a relatively modest increase in electrical resistivity. Additionally, the reduced thermal conductivity of the annealed $Sb_xTe_{1-x}$ nanocomposites can be anticipated by the increased phonon scattering at the interface of γ-SbTe and $Sb_2Te_3$. Nanocomposites with abnormally enhanced Seebeck coefficients can be utilized in the practical fabrication for commercial thermoelectric devices, instead of less practical single crystal.

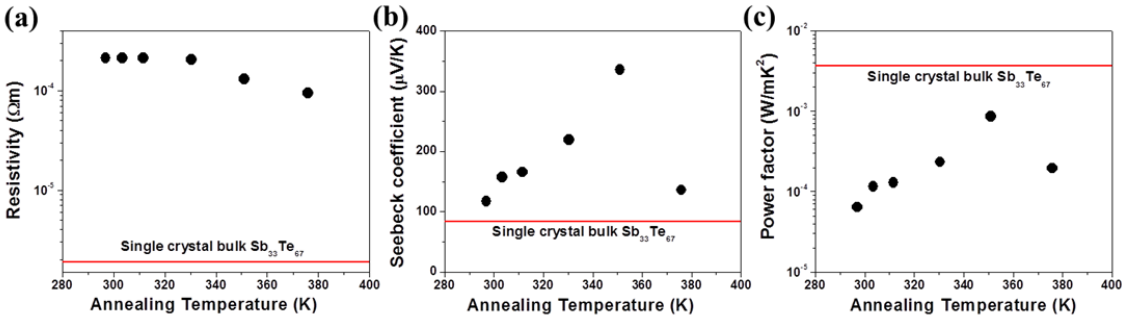


**Figure 2.18:** Annealing temperature dependent thermoelectric properties of $Sb_{42}Te_{58}$ thin film at room temperature: electrical resistivity (a), Seebeck coefficient (b) and power factor (c). A film was annealed for thermal cycle on the measurement stage in the air (Solid lines display the thermoelectric properties of bulk single crystal $Sb_{33}Te_{67}$ [27].

### 2.2.5 Conclusions

In conclusion, $Sb_xTe_{1-x}$ electrodeposits with high thermoelectric properties were synthesized by a cost-effective and mass-productive electrodeposition technique. Temperature dependent thermoelectric properties of $Sb_xTe_{1-x}$ electrodeposits with tailored morphology and composition were investigated. Improved thermoelectric properties were demonstrated in $Sb_xTe_{1-x}$ films with smooth and dense morphologies rather than films with nodular/granular morphologies, since the electrical conductivities were improved by the reduced electron scattering. Phase transition properties from amorphism to polycrystallinity were corresponded with electrical properties in a thermal cycle for measurement. The thermal activation energies of amorphous and polycrystal $Sb_xTe_{1-x}$ films were 147 meV and 130 meV, respectively, which were obtained from temperature dependent electrical resistivity. Moreover, the crystallinity of $Sb_xTe_{1-x}$ electrodeposits was controlled by annealing temperature. The $Sb_xTe_{1-x}$ electrodeposits annealed at 330 K and 351 K indicated a nanocomposite structure with inclusions of γ-SbTe phase in the

$Sb_xTe_{1-x}$ matrix. Consequently, the $Sb_xTe_{1-x}$ nanocomposites including γ-SbTe inclusions demonstrated drastically enhanced Seebeck coefficients.

### 2.2.6 References


[1] G. Chen, M. S. Dresselhaus, G. Dresselhaus, J.-P. Fleurial and T. Caillat, Recent developments in thermoelectric materials, *International Materials Reviews,* 2003. **48**: p. 45-66

[2] M. S. Dresselhaus, G. Chen, M. Y. Tang, R. Yang, H. Lee, D. Wang, Z. Ren, J.-P. Fleurial and P. Gogna, New Directions for Low-Dimensional Thermoelectric Materials, *Advanced Materials,* 2007. **19**: p. 1043-1053

[3] A. I. Hochbaum, R. Chen, R. D. Delgado, W. Liang, E. C. Garnett, M. Najarian, A. Majumdar and P. Yang, Enhanced thermoelectric performance of rough silicon nanowires, *Nature,* 2008. **451**: p. 163-167

[4] A. I. Boukai, Y. Bunimovich, J. Tahir-Kheli, J.-K. Yu, W. A. Goddard Iii and J. R. Heath, Silicon nanowires as efficient thermoelectric materials, *Nature,* 2008. **451**: p. 168-171

[5] T. C. Harman, P. J. Taylor, M. P. Walsh and B. E. LaForge, Quantum Dot Superlattice Thermoelectric Materials and Devices, *Science,* 2002. **297**: p. 2229-2232

[6] R. Venkatasubramanian, E. Siivola, T. Colpitts and B. O'Quinn, Thin-film thermoelectric devices with high room-temperature figures of merit, *Nature,* 2001. **413**: p. 597-602

[7] B. Poudel, Q. Hao, Y. Ma, Y. Lan, A. Minnich, B. Yu, X. Yan, D. Wang, A. Muto, D. Vashaee, X. Chen, J. Liu, M. S. Dresselhaus, G. Chen and Z. Ren, High-Thermoelectric Performance of Nanostructured Bismuth Antimony Telluride Bulk Alloys, *Science,* 2008. **320**: p. 634-638

[8] M. S. Dresselhaus, G. Chen, M. Y. Tang, R. G. Yang, H. Lee, D. Z. Wang, Z. F. Ren, J. P. Fleurial and P. Gogna, New Directions for Low-Dimensional Thermoelectric Materials, *Advanced Materials,* 2007. **19**: p. 1043-1053

[9] H. Zou, D. M. Rowe and S. G. K. Williams, Peltier effect in a co-evaporated $Sb_2Te_3$(P)-$Bi_2Te_3$(N) thin film thermocouple, *Thin Solid Films,* 2002. **408**: p. 270-274

[10] G. J. Snyder, J. R. Lim, C.-K. Huang and J.-P. Fleurial, Thermoelectric microdevice fabricated by a MEMS-like electrochemical process, *Nat Mater,* 2003. **2**: p. 528-531

[11] F. Xiao, B. Yoo, K.-H. Lee and N. V. Myung, Electro-transport studies of electrodeposited $(Bi_{1-x}Sb_x)_2Te_3$ nanowires, *Nanotechnology,* 2007. **18**: p. 335203

[12] A. Giani, A. Boulouz, F. Pascal-Delannoy, A. Foucaran, A. Boyer, B. Aboulfarah and A. Mzerd, Electrical and Thermoelectrical Properties of $Sb_2Te_3$ Prepared by the Metal-Organic Chemical Vapor Deposition Technique, *Journal of Materials Science Letters,* 1999. **18**: p. 541-543

[13] M. Wuttig and N. Yamada, Phase-change materials for rewriteable data storage, *Nat Mater,* 2007. **6**: p. 824-832

[14] M. H. R. Lankhorst, B. W. S. M. M. Ketelaars and R. A. M. Wolters, Low-cost and nanoscale non-volatile memory concept for future silicon chips, *Nat Mater,* 2005. **4**: p. 347-352

[15] S.-H. Lee, Y. Jung and R. Agarwal, Highly scalable non-volatile and ultra-low-power phase-change nanowire memory, *Nat Nano,* 2007. **2**: p. 626-630

[16] M. M. Ibrahim, M. M. Wakkad, E. K. Shokr and H. A. Abd El-Ghani, Electrical properties of antimony telluride, *Applied Physics A: Materials Science & Processing,* 1991. **52**: p. 237-241

[17] Y. Kim, A. DiVenere, G. K. L. Wong, J. B. Ketterson, S. Cho and J. R. Meyer, Structural and thermoelectric transport properties of $Sb_2Te_3$ thin films grown by molecular beam epitaxy, *Journal of Applied Physics,* 2002. **91**: p. 715-718

[18] H. Zou, D. M. Rowe and G. Min, Preparation and characterization of p-type $Sb_2Te_3$ and n-type $Bi_2Te_3$ thin films grown by coevaporation, *Journal of Vacuum Science & Technology A: Vacuum, Surfaces, and Films,* 2001. **19**: p. 899-903

[19] S. A. Baily and D. Emin, Transport properties of amorphous antimony telluride, *Physical Review B (Condensed Matter and Materials Physics),* 2006. **73**: p. 165211-8

[20] V. D. Das and N. Soundararajan, Thermoelectric power and electrical resistivity of crystalline antimony telluride ($Sb_2Te_3$) thin films: Temperature and size effects, *Journal of Applied Physics,* 1989. **65**: p. 2332-2341

[21] G. Leimkuhler, I. Kerkamm and R. Reineke-Koch, Electrodeposition of Antimony Telluride, *Journal of The Electrochemical Society,* 2002. **149**: p. C474-C478

[22] Q. Huang, A. J. Kellock and S. Raoux, Electrodeposition of SbTe Phase-Change Alloys, *Journal of The Electrochemical Society,* 2008. **155**: p. D104-D109

[23] K. Park, F. Xiao, B. Y. Yoo, Y. Rheem and N. V. Myung, Electrochemical deposition of thermoelectric $Sb_xTe_y$ thin films and nanowires, *Journal of Alloys and Compounds,* 2009. **485**: p. 362-366

[24] C. Wang, Q. Wang, L. Chen, X. Xu and Q. Yao, Electrodeposition of $Sb_2Te_3$ Films on Si(100) and Ag Substrates, *Electrochemical and Solid-State Letters,* 2006. **9**: p. C147-C149

[25] A. L. Patterson, The Scherrer Formula for X-Ray Particle Size Determination, *Physical Review,* 1939. **56**: p. 978

[26] C. S. Barrett and T. B. Massalski, *Structure of Metals: Crystallographic Methods, Principles, and Data,* Pergamon Oxford, 1980.

[27] D. M. Rowe, *CRC Handbook of Thermoelectrics,* Boca Raton, CRC Press, Inc., 1995.

[28] J. Martin, L. Wang, L. Chen and G. S. Nolas, Enhanced Seebeck coefficient through energy-barrier scattering in PbTe nanocomposites, *Physical Review B,* 2009. **79**: p. 115311

[29] J. M. O. Zide, D. Vashaee, Z. X. Bian, G. Zeng, J. E. Bowers, A. Shakouri and A. C. Gossard, Demonstration of electron filtering to increase the Seebeck coefficient

in $In_{0.53}Ga_{0.47}As/In_{0.53}Ga_{0.28}Al_{0.19}As$ superlattices, *Physical Review B,* 2006. **74**: p. 205335

[30] D. Vashaee and A. Shakouri, Improved Thermoelectric Power Factor in Metal-Based Superlattices, *Physical Review Letters,* 2004. **92**: p. 106103

[31] J. Zhou and R. Yang, Thermoelectric transport in strongly correlated quantum dot nanocomposites, *Physical Review B,* 2010. **82**: p. 075324

[32] C. Grenzebach, F. B. Anders, G. Czycholl and T. Pruschke, Transport properties of heavy-fermion systems, *Physical Review B,* 2006. **74**: p. 195119

[33] H. Schweitzer and G. Czycholl, Resistivity and thermopower of heavy-fermion systems, *Physical Review Letters,* 1991. **67**: p. 3724

# CHAPTER 3

# Two Dimensional Silver Telluride and Silver Antimony Telluride Thin Films

## 3.1 Silver Telluride by Topochemical Reaction of Tellurium

### 3.1.1 Abstract

A systematic study of the composition-dependent electrical properties of silver telluride ($Ag_xTe_{1-x}$) thin films was conducted. The $Ag_xTe_{1-x}$ thin films were synthesized by a topochemical transformation reaction of thermal evaporated tellurium (Te) thin films, where the film compositions were controlled by the reaction time. We investigated the composition-dependent electrical properties of $Ag_xTe_{1-x}$ thin films with the thickness of 200 ± 27 nm as a function of temperature. The electrical properties of the $Ag_xTe_{1-x}$ thin films indicated the transition from p-type to n-type semiconducting behavior was dependent on the film composition. The electrical resistivity (ρ) and Seebeck coefficients (S) of p-type Te-rich $Ag_{2-x}Te$ and n-type Ag-rich $Ag_{2+x}Te$ thin films were investigated.

### 3.1.2 Introduction

Considerable attention has been paid to chalcogenide semiconductors (i.e. $Ag_2Te$, $Ag_2Se$, $Bi_2Te_3$, $Sb_2Te_3$, CdTe, PbTe and GeTe) due to their potential applications for various electronic, optical, magnetic and thermoelectric devices. Especially, $Ag_2Te$ has shown attractive properties such as a structural phase transition between β-$Ag_2Te$ and α-$Ag_2Te$ [1-4], huge magnetoresistance [5-7], and high Seebeck coefficients [3, 4, 8-11].

The structural phase transition between the monoclinic phase (β-$Ag_2Te$) at low temperature and the face-centered cubic phase (α-$Ag_2Te$) at high temperature over 423K has been reversibly demonstrated. The electrical transport properties of $Ag_2Te$ were dependent on the structural phase [1-4]. The monoclinic β-$Ag_2Te$ with a narrow energy band gap demonstrated high mobility and low lattice thermal conductivity, and the electrical transport of face-centered cubic α-$Ag_2Te$ was dominated by the superionic conduction of Ag cations through Te anions sublattice [12-15]. Thickness-dependent Seebeck coefficients of $Ag_2Te$ thin films have been investigated, where a Seebeck coefficient of - 110μV/K in the film thickness of 41 nm at ~300K was demonstrated [9]. Seebeck coefficients of -130μV/K and - 80μV/K at ~300K for $Ag_2Te$ nanowires have also been reported [1, 3]. Based on the magnetic field-dependent magnetothermopower, the Seebeck coefficients of -200μV/K at 300K and +470μV/K at 100 K, respectively, were observed under the magnetic field of 7 T, where the carrier type of the $Ag_2Te$ semiconductor was changed [11].

The synthesis of $Ag_2Te$ materials has typically been conducted by an elemental reaction of silver and tellurium at a high temperature in evacuated tubes [2, 5, 6, 9], by an aqueous reaction of metal-salts solutions [16] and by mechanical alloying of silver and tellurium powders [17]. Recently, a solution-phase synthesis of $Ag_2Te$ has been investigated as a cost-effective and simple technique [1, 3, 18-21]. $Ag_2Te$ has been prepared by hydrothermal techniques with reducing agents such as hydrazine at high temperatures [1, 18-20]. Another approach is a topochemical transformation of chalcogen, which provides a rapid and simple process to be able to synthesize metal-chalcogen

compounds at room temperature with the structure preservation of an origin chalcogen material [3, 21]. The topochemical transformation of $Ag_2Te$ was implemented by the lattice matching between hexagonal tellurium and monoclinic β-$Ag_2Te$.

The charge carrier type of $Ag_2Te$ can be determined by Ag dopants. However, no systematic study has been carried out on the composition-dependent electrical properties of $Ag_2Te$. In this work, we synthesized $Ag_2Te$ thin films using a topochemical transformation of thermal evaporated Te thin films, and their film compositions were controlled by the reaction time. The electrical properties of $Ag_xTe_{1-x}$ thin films with different compositions were investigated as a function of temperature.

### 3.1.3 Experimental

Glass slides, used as a substrate were polished by an abrasive paper (Buehler, Grit 320/P400) and then were well cleaned by sonication in isopropyl alcohol. Tellurium (TED PELLA, 99.999%) was evaporated from a tungsten filament on the polished glass slide in an evaporation unit (Dentor Vacuum, DV-502). A working pressure of $8x10^{-6}$ torr was maintained throughout the evaporation process. The film thickness of 212±78 nm was analyzed by a profilometer (Veeco, Dektak 8). For the topochemical transformation reaction, a solution was prepared by dissolving 2.50 mmol $AgNO_3$ (Fisher Sci. >99.7%) in 50 mL distilled water. The thermal evaporated Te films on the polished glass slide were dipped into the prepared 50 mM $AgNO_3$ solutions under a controlled reaction time which was varied from 1 min to 720 min.

The open circuit potentials to study the degree of reaction were measured in a three-electrode configuration using the thermally evaporated Te films as a working electrode, and platinum-coated titanium stripes as reference and counter electrodes. The crystal structures of the composition-dependent films were investigated by X-ray diffraction patterns (Rigaku, D/Max-2500/PC). The morphologies and compositions of the films were analyzed by SEM (Philips, XL30-FEG) and energy dispersive spectroscopy (Phoenix, EDAX). The electrical properties of the synthesized films were measured using a custom-made apparatus as described in Chaper 2.2. In-plane electrical resistivity was measured by the typical four point probes method, where the inside of two probes consisted of T-type thermocouple microprobes (Physitemp Instrument Inc. 0.33mm). The distance between the probes was fixed at 2 mm. Seebeck coefficients were determined by the alternatively measured variation of voltage and temperature gradient between two thermocouple probes with a nanovolt-meter (Keithley, 2182A) and a multi-meter (Keithley, 2010) combined with a switching system (NI, USB-6008 DAQ). The film temperature was controlled by the heating band on one end of the sample holder using a DC power supply (Hewlett Packard, 6655A).

### 3.1.4 Results and Discussion

A topochemical transformation reaction for the synthesis of nanostructured materials has been receiving attention due to the preservation of the original chalcogen structure in a simple and cost-effective manner [3, 21]. The topochemical transformation reaction was achieved by the conformity of the crystal structures between a reactant

material and a product material. The lattice of Te with a hexagonal crystal structure was reported to be matched with $Ag_2Te$ with a monoclinic crystal structure accompanied by the lateral volume expansion [21]. Figure 3.1 shows a composition variation and an open circuit potential of $Ag_2Te$ thin films depending on the reaction times of the topochemical transformation of thermal evaporated Te thin films with a thickness of 212±78 nm. The reaction time was varied from 1 min to 720 min with increases in Ag content in $Ag_xTe_{1-x}$. Ag content in $Ag_xTe_{1-x}$ gradually increased and then abruptly enhanced from 60 min. The silver telluride ($Ag_2Te$) films with a near-stoichiometric composition were spontaneously synthesized after 120 min by the thermodynamically favorable topochemical reaction. The open circuit potential of the Te films deposited on glass slides was measured in 50 mM $AgNO_3$ to monitor the topochemical transformation reaction. A platinum-coated titanium stripe was employed as a reference electrode to avoid the precipitation of silver salts during the open-circuit potential measurement. As expected, the open circuit potential of the films was changed with the increased Ag dopants of Te films.

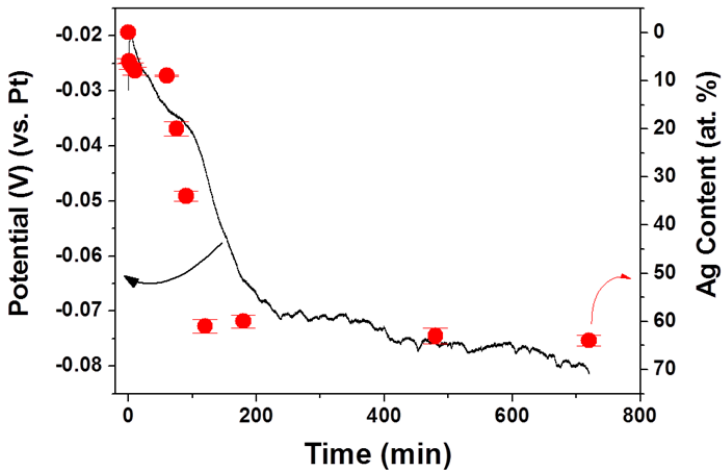


**Figure 3.1**: Open circuit potential and film composition depending on reaction time of an as-deposited Te thin film.

X-ray diffraction patterns of the films with tailored compositions were analyzed as shown in Figure 3.2. An as-deposited Te thin film indicated the diffraction pattern of a hexagonal crystal structure. The $Ag_9Te_{91}$ film transformed for 60 min showed the developed (3 1 2) plane of hexagonal $Ag_5Te_3$ (JCPDS #47-1350) in the diffraction pattern of Te (JCPDS #36-1452), as expected in a phase diagram of a silver-tellurium system [22]. In the diffraction patterns of the Te-rich $Ag_{20}Te_{60}$ and $Ag_{34}Te_{66}$ thin films transformed for 75 min and 90 min, the peaks of Te disappeared and the peaks of hexagonal $Ag_5Te_3$ were mainly developed. The peaks of monoclinic β-$Ag_2Te$ (JPDS #34-0142) began to develop. Near stoichiometric $Ag_{61}Te_{39}$ and $Ag_{64}Te_{36}$ thin films illustrated the well-developed peaks of monoclinic β-$Ag_2Te$ with a peak of (3 1 2) plane in $Ag_5Te_3$. To describe the conformity of crystal structures in the topochemical transformation, the variation of x-ray diffraction patterns showed the varied crystal structures depending on the topochemical reaction time. Te-rich thin films maintained the hexagonal crystal structure from Te to $Ag_5Te_3$ with different lattice parameters. The monoclinic crystal structure of near stoichiometric films was varied from the hexagonal crystal structure of $Ag_5Te_3$ based on the lattice conformity, as Unyoung Jeong, et al. indicated the direct conformity between hexagonal Te and monoclinic $Ag_2Te$ of one-dimensional nanostructures [21]. The variation of crystal structure depending on the film compositions was described in the topochemical reactions.

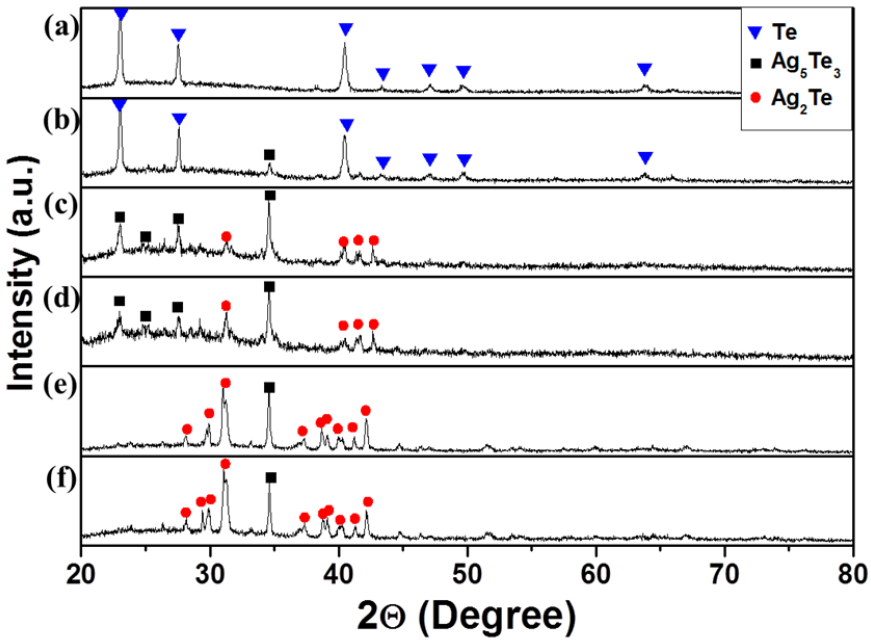


**Figure 3.2**: X ray diffraction patterns of topochemically transformed films: as-deposited Te (a), $Ag_9Te_{91}$ reacted for 60min (b), $Ag_{20}Te_{80}$ reacted for 75 min (c), $Ag_{34}Te_{66}$ reacted for 90 min (d), $Ag_{61}Te_{39}$ reacted for 120 min (e) and $Ag_{64}Te_{36}$ reacted for 720 min (f).

The morphologies of a thermal evaporated Te thin film and the topochemically reacted $Ag_xTe_{1-x}$ thin films as a function of reaction time are shown in Figure 3.3, which clearly described the reaction progress. The as-deposited Te film with a relatively dense and smooth morphology was transformed to the $Ag_6Te_{94}$ film with the partial wool-like morphology on the surface by dipping it in the $AgNO_3$ solution for 1 min. As the Ag content increased with reaction time, the number of balls of wool on the surface increases. After the reaction time of 120 min, the converted surface of a stoichiometric $Ag_{61}Te_{39}$ film was completely changed to the porous wool-like morphology with grain boundaries. After 720 min, the dense wool-like surface of the $Ag_{64}Te_{36}$ film without grain boundary

was synthesized, but a lateral volume expansion due to the transformation from Te to $Ag_2Te$ produced cracks in the film.

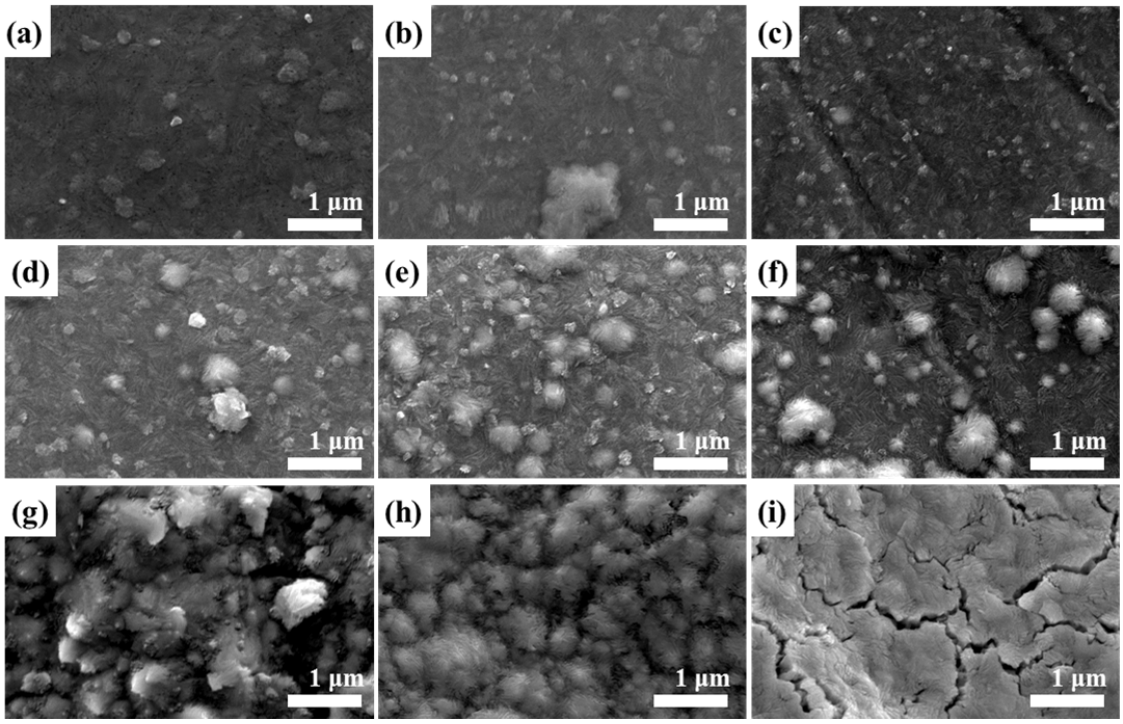


**Figure 3.3**: The surface morphologies $Ag_xTe_{1-x}$ thin films synthesized by topochemical transformation as a function of the reaction time: as-deposited Te (a), $Ag_6Te_{94}$ for 1 min (b), $Ag_7Te_{93}$ for 5 min (c), $Ag_8Te_{92}$ for 10 min (d), $Ag_9Te_{91}$ for 60 min (e), $Ag_{20}Te_{80}$ for 75 min (f), $Ag_{34}Te_{66}$ for 90 min (g), $Ag_{61}Te_{39}$ for 120 min (h) and $Ag_{64}Te_{36}$ for 720 min (i).

Glass slides were used as a substrate of the thermally evaporate Te films, because an insulating substrate such as a glass slide is required for the in-plane measurement of Seebeck coefficients. In addition, the glass slide substrates were polished to enhance the mechanical adhesion, because topochemically transformed $Ag_xTe_{1-x}$ films can be peeled off by the stress due to the lateral volume expansion of the films. Figure 3.4 describes the

in-plane electrical resistivity (ρ), Seebeck coefficients (S) and power factors ($S^2/\rho$) of a thermally evaporated Te film as a function of temperature during a heating / cooling cycle in air. Temperature-dependent electrical resistivity of the as-deposited Te film showed a typical degenerated semiconducting behavior. The resistivity of the Te film decreased with increases in temperature. Compared to the electrical resistivity of an as-deposited Te thin film in a heating step, the Te thin film, annealed at the temperature of less than 373K, showed increased resistivity, which might be attributed to the oxidation of the surface [23]. The Seebeck coefficients of the as-deposited Te film demonstrated p-type transport behavior. The temperature-dependent Seebeck coefficient was linearly proportional to the increase in temperature, where the Seebeck coefficient of 207μV/K at 300K increased to 323μV/K at 370K. The calculated power factor of the as-deposited Te film increased with increased temperature in complement to the trends of temperature-dependent electrical conductivity and Seebeck coefficients.

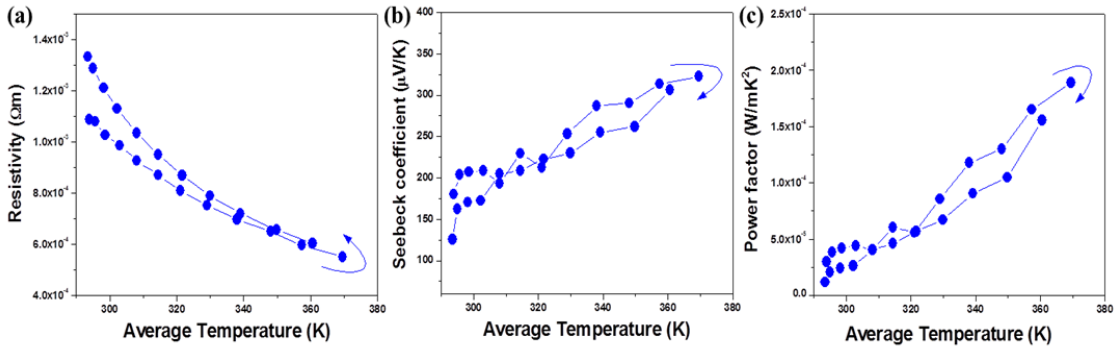


**Figure 3.4**: The temperature-dependent electrical resistivity (a), Seebeck coefficient (b) and power factor (c) of as-deposited Te thin film with the thickness of 212±78nm. The measurement was implemented for the thermal cycle of heating/cooling steps.

The temperature-dependent electrical resistivity, Seebeck coefficients and power factors of a topochemically transformed $Ag_{64}Te_{36}$ thin film with a near-stoichiometric composition are illustrated in Figure 3.5. The electrical resistivity decreased with increases in temperature showing a typical semiconducting behavior, and the film annealed in the heating step showed increased electrical resistivity due to the surface oxidation. In contrast with Te and Te-rich $Ag_xTe_{1-x}$ thin films of a p-type transport behavior, the negative Seebeck coefficients of the Ag-rich $Ag_{64}Te_{36}$ thin film indicated n-type transport behavior. Temperature-dependent Seebeck coefficients of the $Ag_{64}Te_{36}$ thin film increased with increases in temperature. A high Seebeck coefficient of -87μV/K at 365K was achieved in the annealed $Ag_{64}Te_{36}$ thin film. The temperature-dependent power factors corresponded with temperature-dependent Seebeck coefficients. Unfortunately, the electrical properties for a phase transition from β-$Ag_2Te$ to α-$Ag_2Te$ cannot be observed, because the maximum temperature of the films was less than a typical phase transition temperature of 323K.

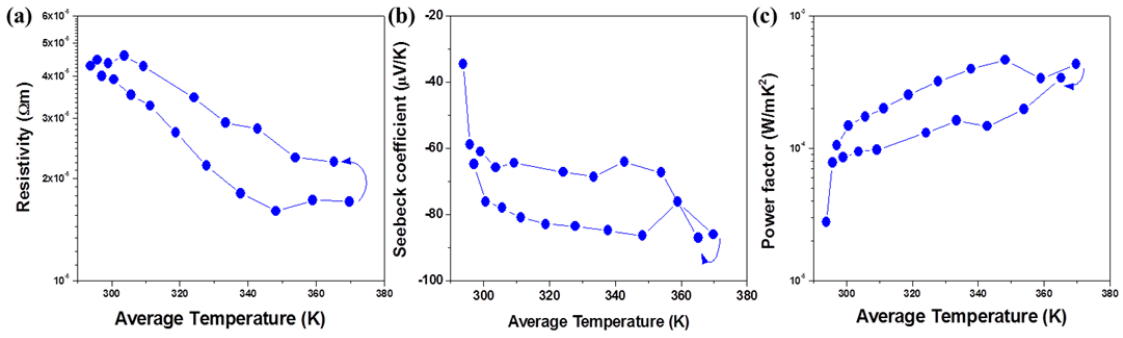


**Figure 3.5**: The temperature-dependent electrical resistivity (a), Seebeck coefficient (b) and power factor (c) of the $Ag_{64}Te_{36}$ thin film during the thermal cycle. The film was prepared by the topochemical reaction of the as-deposited Te thin film for 720 min.

The electrical resistivity, Seebeck coefficients and power factors of the films with the varied Ag content depending on the reaction time were analyzed as shown in Figure 3.6. The electrical resistivity increased with increase of Ag content in the Te thin films, and abruptly decreased in the composition of near-stoichiometric $Ag_{64}Te_{36}$. The Ag dopants in the Te lattice with hexagonal crystal structure can generate both crystal defects and charge carriers, resulting in the reduction of mobility and the enhancement of carrier concentration. Even though the substituted $Ag^{+}$ ions to the hexagonal Te lattice can increase carrier concentrations, the Ag vacancies mainly increased the hole carrier concentration in the p-type Te chalcogenides [24, 25]. The transport behavior dominated by the reduced mobility, not the increased carrier concentration was shown in Te-rich $Ag_xTe_{1-x}$ thin films. However, the monoclinic β-$Ag_2Te$ with a near-stoichiometric composition showed enhanced electrical conductivity due to the intrinsic high mobility of β-$Ag_2Te$ materials with a narrow energy band gap in the range of several tens of meV [2, 8, 14, 15]. The Seebeck coefficient was inversely proportional to the charge carrier concentration [26, 27]. Even though the Te-rich $Ag_9Te_{91}$ thin film demonstrated higher Seebeck coefficients than the as-deposited Te thin film, the Seebeck coefficients of Te-rich $Ag_xTe_{1-x}$ films decreased with increases in the Ag content, which might be attributed to the increased carrier concentration of the film. The negative Seebeck coefficient of -65μV/K in the Ag-rich $Ag_{64}Te_{36}$ thin film of a near-stoichiometric composition showed the transition of a charge carrier type from holes to n-type electrons.

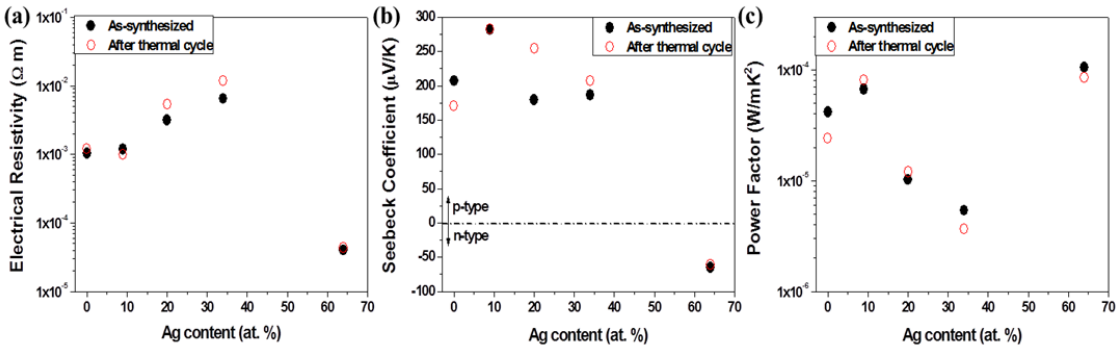


**Figure 3.6**: The composition-dependent electrical resistivity (a), Seebeck coefficient (b) and power factor (c) of the as-deposited Te thin film, the as-transformed $Ag_xTe_{1-x}$ thin films and the thermal cycled $Ag_xTe_{1-x}$ thin film. The properties of near room temperature were displayed.

### 3.1.5 Conclusions

In conclusion, the silver telluride ($Ag_xTe_{1-x}$) thin films with tailored compositions were synthesized by the topochemical transformation reaction of thermal evaporated Te thin films as an economic and feasible technique. The temperature-dependent electrical properties including the electrical resistivity, Seebeck coefficient and power factor of the prepared films were systematically measured for the thermal cycle of heating/cooling steps using a custom-made apparatus. The Seebeck coefficients and power factors of the films were linearly proportional to increase in temperature. In addition, an as-deposited Te thin film, Te-rich $Ag_xTe_{1-x}$ thin films and a near-stoichiometric $Ag_{64}Te_{36}$ thin film demonstrated distinctive properties depending on the film composition. The electrical resistivity of the Te film increased with increase of Ag dopants, and near-stoichiometric $Ag_{64}Te_{36}$ thin film showed the abruptly decreased resistivity with about two orders of magnitude less than the Te-rich $Ag_{34}Te_{66}$ thin film. The Seebeck coefficients of the films

demonstrated the transition of the charge carrier type from the p-type Te and Te-rich $Ag_xTe_{1-x}$ thin films to the n-type Ag-rich $Ag_{64}Te_{36}$ thin film.

### 3.1.6 References


[1] F. Li, C. Hu, Y. Xiong, B. Wan, W. Yan and M. Zhang, Phase-Transition-Dependent Conductivity and Thermoelectric Property of Silver Telluride Nanowires, *The Journal of Physical Chemistry C,* 2008. **112**: p. 16130-16133

[2] P. Gnanadurai, N. Soundararajan and C. E. Sooriamoorthi, Studies on the electrical conduction in silver telluride thin films, *physica status solidi (b),* 2003. **237**: p. 472-478

[3] A. K. Samal and T. Pradeep, Room-Temperature Chemical Synthesis of Silver Telluride Nanowires, *The Journal of Physical Chemistry C,* 2009. **113**: p. 13539-13544

[4] F. F. Aliev, Phase Transition of Ag-Enriched $Ag_2Te$, *Inorganic Materials,* 2002. **38**: p. 995-997

[5] H. S. Schnyders, M. L. Saboungi and T. F. Rosenbaum, Magnetoresistance in n- and p-type $Ag_2Te$: Mechanisms and applications, *Applied Physics Letters,* 2000. **76**: p. 1710-1712

[6] R. Xu, A. Husmann, T. F. Rosenbaum, M. L. Saboungi, J. E. Enderby and P. B. Littlewood, Large magnetoresistance in non-magnetic silver chalcogenides, *Nature,* 1997. **390**: p. 57-60

[7] I. S. Chuprakov and K. H. Dahmen, Large positive magnetoresistance in thin films of silver telluride, *Applied Physics Letters,* 1998. **72**: p. 2165-2167

[8] P. F. Taylor and C. Wood, Thermoelectric Properties of $Ag_2Te$, *Journal of Applied Physics,* 1961. **32**: p. 1-3

[9] P. Gnanadurai, N. Soundararajan and C. E. Sooriamoorthy, Investigation on the influence of thickness and temperature on the Seebeck coefficient of silver telluride thin films, *Vacuum,* 2002. **67**: p. 275-284

[10] V. D. Das and D. Karunakaran, Thermoelectric studies on semiconducting $Ag_2Te$ thin films: Temperature and dimensional effects, *Physical Review B,* 1984. **30**: p. 2036

[11] Y. Sun, M. B. Salamon, M. Lee and T. F. Rosenbaum, Giant magnetothermopower associated with large magnetoresistance in $Ag_{2-\delta}Te$, *Applied Physics Letters,* 2003. **82**: p. 1440-1442

[12] R. Chen, D. Xu, G. Guo and L. Gui, Silver telluride nanowires prepared by dc electrodeposition in porous anodic alumina templates, *Journal of Materials Chemistry,* 2002. **12**: p. 2435-2438

[13] M. Kobayashi, K. Ishikawa, F. Tachibana and H. Okazaki, Diffusion path and Haven's ratio of mobile ions in $\alpha$-$Ag_2Te$, *Physical Review B,* 1988. **38**: p. 3050

[14] D. Richard and G. Robert, Electrical Properties of $\beta$-$Ag_2Te$ and $\beta$-$Ag_2Se$ from $4.2^{o}$ to $300^{o}$K, *Journal of Applied Physics,* 1967. **38**: p. 753-756

[15] M. Fujikane, K. Kurosaki, H. Muta and S. Yamanaka, Thermoelectric properties of α- and β-Ag2Te, *Journal of Alloys and Compounds,* 2005. **393**: p. 299-301

[16] C. J. Warren, R. C. Haushalter and A. B. Bocarsly, The electrochemical synthesis of telluride Zintl anions, *Journal of Alloys and Compounds,* 1995. **229**: p. 175-205

[17] K. Sridhar and K. Chattopadhyay, Synthesis by mechanical alloying and thermoelectric properties of $Cu_2Te$, *Journal of Alloys and Compounds,* 1998. **264**: p. 293-298

[18] L. Zhang, Z. Ai, F. Jia, L. Liu, X. Hu and J. C. Yu, Controlled Hydrothermal Synthesis and Growth Mechanism of Various Nanostructured Films of Copper and Silver Tellurides, *Chemistry – A European Journal,* 2006. **12**: p. 4185-4190

[19] A. Qin, Y. Fang, P. Tao, J. Zhang and C. Su, Silver Telluride Nanotubes Prepared by the Hydrothermal Method, *Inorganic Chemistry,* 2007. **46**: p. 7403-7409

[20] P. Zuo, S. Zhang, B. Jin, Y. Tian and J. Yang, Rapid Synthesis and Electrochemical Property of $Ag_2Te$ Nanorods, *The Journal of Physical Chemistry C,* 2008. **112**: p. 14825-14829

[21] G. D. Moon, S. Ko, Y. Xia and U. Jeong, Chemical Transformations in Ultrathin Chalcogenide Nanowires, *ACS Nano,* 2010. **4**: p. 2307-2319

[22] I. Karakaya and W. T. Thompson, The Ag-Te (Silver-Tellurium) System, *Journal of Phase Equilibria,* 1991. **12**: p. 56-63

[23] D. Tsiulyanu, S. Marian, H. D. Liess and I. Eisele, Effect of annealing and temperature on the $NO_2$ sensing properties of tellurium based films, *Sensors and Actuators B: Chemical,* 2004. **100**: p. 380-386

[24] V. Jovovic and J. P. Heremans, Measurements of the energy band gap and valence band structure of $AgSbTe_2$, *Physical Review B,* 2008. **77**: p. 245204

[25] S. N. Zhang, T. J. Zhu, S. H. Yang, C. Yu and X. B. Zhao, Phase compositions, nanoscale microstructures and thermoelectric properties in $Ag_{2-y}Sb_yTe_{1+y}$ alloys with precipitated $Sb_2Te_3$ plates, *Acta Materialia,* 2010. **58**: p. 4160-4169

[26] D. M. Rowe, *CRC Handbook of Thermoelectrics,* Boca Raton, CRC Press, Inc., 1995.

[27] G. J. Snyder and E. S. Toberer, Complex thermoelectric materials, *Nature Materials,* 2008. **7**: p. 105-114

## 3.2 Silver Antimony Telluride by Cation Exchange Reaction of Antimony Telluride

### 3.2.1 Abstract

Ternary silver antimony telluride ($Ag_xSb_{1-x}Te_y$) thin films with tailored compositions were synthesized by a cationic exchange reaction, as a simple and cost-effective approach. Thermally evaporated antimony telluride thin films with a thickness of 180±32 nm on polished glass slides were transformed to $Ag_xSb_{1-x}Te_y$ thin films by a cationic exchange reaction. The composition of $Ag_xSb_{1-x}Te_y$ thin films was controlled by the reaction time. Temperature-dependent electrical properties of $Ag_xSb_{1-x}Te_y$ thin films demonstrated phase transition behavior from 323K to 343K. The composition-dependent thermoelectric properties (i.e., electrical resistivity (ρ), Seebeck coefficient (S) and power factor ($S^2\rho$)) of the as-deposited $Sb_{54}Te_{46}$, the transformed $Ag_xSb_{1-x}Te_y$ and the annealed $Ag_xSb_{1-x}Te_y$ thin films were investigated as a function of temperature.

### 3.2.2 Introduction

The ternary Ag-doped antimony telluride chalcogenides and their quaternary compounds have been extensively developed for application in thermoelectric and phase change memory devices, and remarkable experimental breakthroughs have been demonstrated. As a p-type thermoelectric material, the ternary $AgSbTe_2$ has shown high Seebeck coefficients of about 200 to 250μV/K at 500 to 600K and low thermal conductivities of 0.6 to 0.7W/mK. [1-8]. The quaternary $(AgSbTe_2)_{1-x}(PbTe)_x$ (LAST) and $(AgSbTe_2)_{1-x}(GeTe)_x$ (TAGS) chalcogenide materials have demonstrated the required

high thermoelectric figure-of-merit (ZT) for application in thermoelectric devices operable at high temperature: LAST with ZT~2 at 900K and TAGS with ZT~1.2 at 450K [9-12]. The enhanced thermoelectric properties of AgSbTe and its alloys were characterized by the embedded interfaces due to the phase separation between $Ag_2Te$ and $Sb_2Te_3$ [1, 8, 13]. Nanocomposite materials with the embedded phases can reduce the lattice thermal conductivity due to the increased phonon scattering and improve the Seebeck coefficient due to the charge carrier filtering [10, 14-17]. In addition, the ternary AgSbTe and its alloy AgInSbTe (AIST) have demonstrated high performance in optical and electrical phase change memory devices [18-23].

The synthesis of ternary AgSbTe chalcogenide compounds has been limited to direct fusion of stoichiometric amounts of elemental silver, antimony and tellurium at high temperatures in evacuated tubes [3, 5-8]. Recently, a cation exchange reaction has been receiving considerable attention as a powerful technique to synthesize various chalcogenide compounds, which provides a simple and cost-effective process to synthesize ternary alloys [24-27].

In this work, we synthesized $Ag_xSb_{1-x}Te_y$ thin films using the cation exchange reaction of thermally evaporated $Sb_{54}Te_{46}$ thin films. The composition of the $Ag_xSb_{1-x}Te_y$ thin films was tailored by the reaction time. The composition- and temperature-dependent thermoelectric power factors were determined by the measurements of the electrical resistivity and Seebeck coefficients of the as-deposited $Sb_{54}Te_{46}$, the cation exchanged $Ag_xSb_{1-x}Te_y$ and annealed $Ag_xSb_{1-x}Te_y$ thin films.

Additionally, the phase transition behavior of $Ag_xSb_{1-x}Te_y$ thin films was analyzed during the thermal cycle for electrical measurements.

### 3.2.3 Experimental

Antimony telluride thin films were thermally evaporated under a pressure of $8x10^{-6}$torr using $Sb_2Te_3$ source materials (Alfa Aesar, 99.999%) loaded in an evaporation unit (Dentor Vacuum, DV-502). Glass slides were employed as a substrate for the $Sb_{54}Te_{46}$ thin films, which were polished with an abrasive paper (Buehler, Grit 320/P400). The thermally evaporated $Sb_{54}Te_{46}$ thin films had the thickness of 180±32 nm measured by a profilometer (Veeco, Dektak 8). The cation exchange reaction of $Sb_{54}Te_{46}$ thin films was conducted in 50 mM $AgNO_3$ (Fisher Sci. >99.7%). The compositions of the $Ag_xSb_{1-x}Te_y$ thin films were tailored by varying the reaction time from 1 min to 720 min.

The in-situ open circuit potential variations of the films in the reaction were measured in a three-electrode configuration which consisted of the $Sb_{54}Te_{46}$ films as a working electrode and two platinum-coated titanium stripes as reference and counter electrodes. SEM (Philips, XL30-FEG) and energy dispersive spectroscopy (Phoenix, EDAX) were utilized to analyze the morphologies and composition of the films. The measurements of the in-plane electrical resistivity and Seebeck coefficients of the films were implemented using a custom-made apparatus as described in Chaper 2.2. The film temperature was controlled from 296K to 395K.

### 3.2.4 Results and Discussion

A cation exchange reaction is an attractive approach to synthesize a ternary chalocgenide and its alloys. Even though various binary compounds have been synthesized by cation exchange reaction, the systematic study of the synthesis of ternary and quaternary compounds using cation exchange reactions is limited [24-26]. As far as we know, the ternary AgSbTe chalcogenide compound synthesized by cation exchange reaction of SbTe has not been investigated. The synthesis of ternary $Ag_xSb_{1-x}Te_y$ chalcogenide thin films using a cation exchange reaction of $Sb_{54}Te_{46}$ thin films in $AgNO_3$ solution was demonstrated. Figure 3.7 describes the composition of $Ag_xSb_{1-x}Te_y$ thin films depending on the cation exchange reaction time (Figure 3.7 (a)) and the in-situ variation of the open circuit potential for the reaction as well as the Ag content of the $Ag_xSb_{1-x}Te_y$ thin films (Figure 3.7 (b)). The Ag content in the films abruptly increased with increasing reaction time up to 60 min accompanied by the abrupt decrease of the Sb content. After 60 min, the Ag and Sb contents in the films were slowly varied. The Te contents in the films were almost preserved during the cation exchange reaction. The variances in composition during the cation exchange reaction corresponded with the variations of the open circuit potential.

The cationic exchange reaction is governed by several critical factors such as the solubility of ionic solids between the reactant and product, the conformity of crystal structure and the tolerable mechanical stress due to volume expansion [24, 27]. Unlike the synthesis of binary materials by a cation exchange reaction from $Ag_2Te$ into CdTe, PbTe and ZnTe, the intermediate phase should be considered as a ternary system. The

typical cationic exchange reaction, including an intermediate state, is described in Equation 3.1. The intermediate phases in ternary systems can be expected to have relatively lower solubilities of ionic solids than those of the reactants and products, even though the solubility of an ionic solid or the hydration enthalpy cannot be confirmed. $Sb_2Te_3$, like $Bi_2Te_3$ and $Bi_2Se_3$, has a hexagonal conventional unit cell consisting of alternating quintuple layers of – ($Te^1$-Bi-$Te^2$-Bi-$Te^1$) – as illustrated in Figure 3.8 [28, 29]. The crystal structure of $AgSbTe_2$ is identified to be a rock-salt structure with Te atoms occupying lattice points in one face-centered crystal structure, and Sb and Ag atoms randomly distributed in the lattice points in the other face-centered crystal structure. For a cation exchange reaction without large structure changes, the structural conformity between $Sb_2Te_3$ with a hexagonal crystal structure and $AgSbTe_2$ with a rock-salt crystal structure is described in Figure 3.8. Moreover, the cation exchange reaction of $Sb_2Te_3$ to $Ag_xSb_{1-x}Te_y$ cannot be restricted by the negligible volume expansion due to the atomic exchange, based on the similar atomic radii of Sb (0.140 nm) and Ag (0.144 nm).

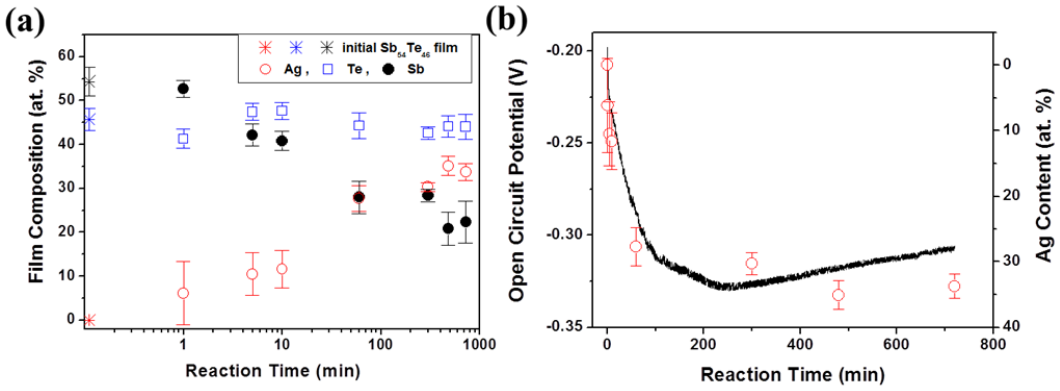


**Figure 3.7**: The composition of the $Ag_xSb_{1-x}Te_y$ films transformed by a cationic exchanged reaction of thermally evaporated $Sb_{54}Te_{46}$ films as a function of reaction time (a) and the variation of the open circuit potential and Ag content in the films depending on reaction time (b).

$$M^+X^-(s) + N^+(aq) \rightarrow \left[M^+_{1-x}N^+_xX^-\right] \rightarrow N^+X^-(s) + M^+(aq) \qquad \text{Equation 3.1}$$

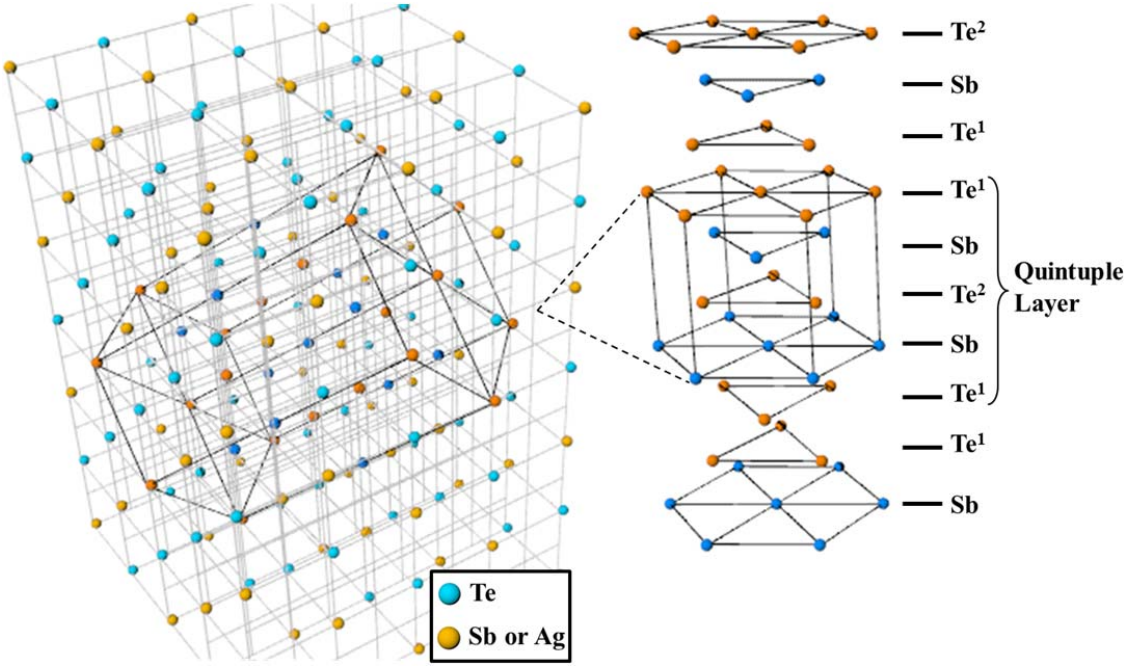


**Figure 3.8**: Schematic illustration of the crystal structures of $AgSbTe_2$ and $Sb_2Te_3$. A hexagonal crystal structure of $Sb_2Te_3$ was embedded in the rock-salt crystal structure of $AgSbTe_2$.

Figure 3.9 describes the morphologies of a thermally evaporated $Sb_{54}Te_{46}$ thin film and the cation exchanged $Ag_xSb_{1-x}Te_y$ thin films depending on reaction time. The as-deposited $Sb_{54}Te_{46}$ thin film on the polished glass slides shows rough and dense surface morphology. The roughness of the films was attributed to the rough surface of the polished substrates. The surface morphologies of cation exchanged $Ag_xSb_{1-x}Te_y$ thin films were analogous in the morphology of the primary $Sb_{54}Te_{46}$ thin film. The comparable surface morphologies of the transformed films can be expected, because the

even crystallinity of the transformed materials in the cation exchange reaction was preserved [24].

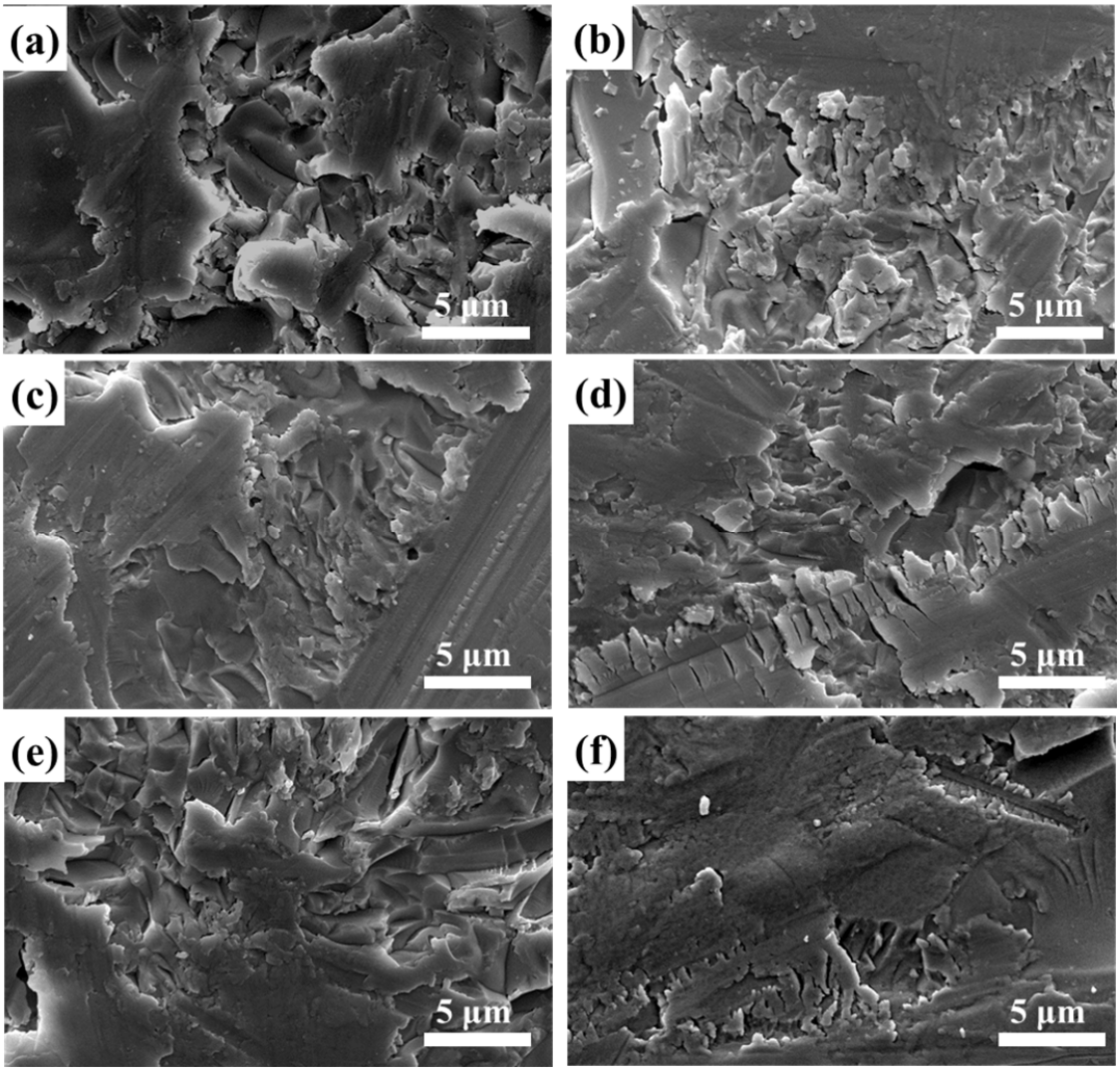


**Figure 3.9**: The surface morphologies of the films depending on the cationic exchange reaction time: As-deposited $Sb_{54}Te_{46}$ (a), $Ag_6Sb_{53}Te_{41}$ transformed for 1 min (b), $Ag_{11}Sb_{35}Te_{54}$ transformed for 5 min (c), $Ag_{12}Sb_{41}Te_{47}$ transformed for 10 min (d), $Ag_{28}Sb_{28}Te_{44}$ transformed for 60 min (e), $Ag_{34}Sb_{22}Te_{44}$ transformed for 720 min (f).

The temperature-dependent electrical properties of as-deposited $Sb_{54}Te_{46}$ and transformed $Ag_xSb_{1-x}Te_y$ thin films were analyzed. Each measurement was conducted in a thermal cycle of a heating step followed by a cooling step. Figure 3.10 describes the electrical resistivity, the Seebeck coefficients and the calculated thermoelectric power factors of the cation exchanged $Ag_6Sb_{53}Te_{41}$ and $Ag_{12}Sb_{41}Te_{47}$ thin films during a thermal cycle in which the temperature was varied from about 297K to 395K and vice versa. The electrical resistivity of the films displayed phase transition behavior due to the crystallization during the heating step. The electrical resistivity of the crystallized films in the cooling step decreased with increasing temperatures, a typical degenerated semiconducting behavior. The Seebeck coefficients with positive values indicated that the films possessed p-type transport behavior. In addition to the electrical resistivity, the Seebeck coefficients of the films showed a sharp reduction with the phase transition. The transition temperature ranged from 323K to 343K, which was corresponded with the listed transition temperature of 343K for $AgSbTe_2$ in another report [30]. The calculated thermoelectric power factors of the crystalized films with lower electrical resistivities and higher Seebeck coefficients after a heating step were higher than those of the as-transformed films with higher electrical resistivities and lower Seebeck coefficients, since the power factor was mainly determined by the reduction of electrical resistivity rather than the reduction of the Seebeck coefficient.

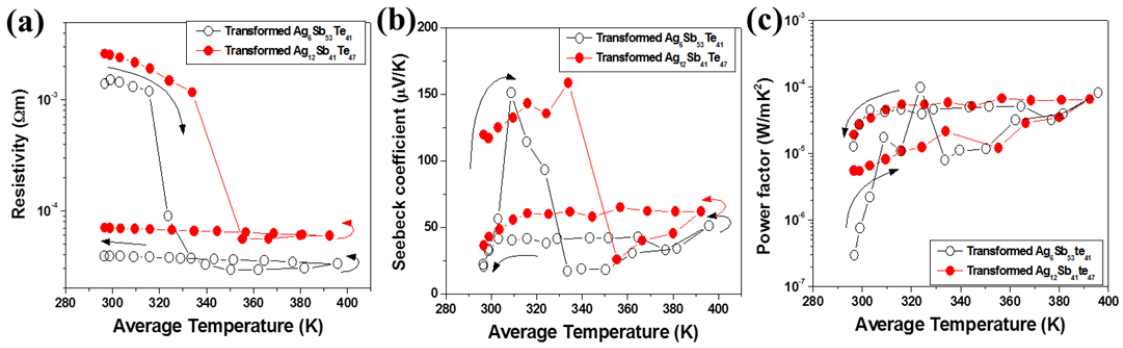


**Figure 3.10**: Temperature-dependent electrical properties of the $Ag_6Sb_{53}Te_{41}$ and $Ag_{12}Sb_{41}Te_{47}$ thin films transformed by the cation exchanged reaction: electrical resistivity (a), Seebeck coefficient (b) and thermoelectric power factors (c). The temperature was varied from 296K to 395K.

The composition-dependent electrical resistivity, Seebeck coefficient and thermoelectric power factor of an as-deposited $Sb_{54}Te_{46}$ film, as-transformed $Ag_xSb_{1-x}Te_y$ film and thermal cycled $Ag_xSb_{1-x}Te_y$ film are described in Figure 3.11. As the composition of the $Ag_xSb_{1-x}Te_y$ thin films deviated from the stoichiometric $AgSbTe_2$, the films showed enhanced electrical conductivity. Increased carrier concentrations in the films can enhance the electrical conductivity with the deviation from stoichiometry resistivity, since the Ag vacancy in p-type $AgSbTe_2$ materials contributes to the electrical transport as a major charge carrier [8, 31]. $Ag_6Sb_{53}Te_{41}$ and $Ag_{28}Sb_{28}Te_{44}$ thin films demonstrated an electrical resistivity of $1.52x10^{-3}\Omega m$ and $5.14x10^{-3}\Omega m$, respectively. The Seebeck coefficients increased with decrease in Ag vacancies (i.e., with increase in Ag contents), which agrees with the idea that the Seebeck coefficients are inversely proportional to the carrier concentration [11, 12]. The as-transformed $Ag_{28}Sb_{28}Te_{44}$ thin films with near-stoichiometric compositions displayed a high Seebeck coefficient of 108.6μV/K. Moreover, the electrical properties of the thermal cycled thin films were

analyzed. After a thermal cycle, the films were crystalized by atomic rearrangement as shown in the abrupt reduction of resistivity during the heating step (Figure 3.10 (a)). The trends of composition-dependent resistivities and Seebeck coefficients corresponded with those of the as-transformed films; the electrical resistivity and Seebeck coefficient increased with an increase in Ag content. However, the $Ag_6Sb_{53}Te_{41}$, $Ag_{11}Sb_{35}Te_{54}$, and $Ag_{12}Sb_{41}Te_{47}$ thin films with Ag vacancies demonstrated enhanced thermoelectric power factors due to the sharp reduction of the electrical resistivity. In the $Ag_6Sb_{53}Te_{41}$ thin film, the electrical resistivity varied from $1.52x10^{-3}\Omega m$ to $3.88x10^{-5}\Omega m$.

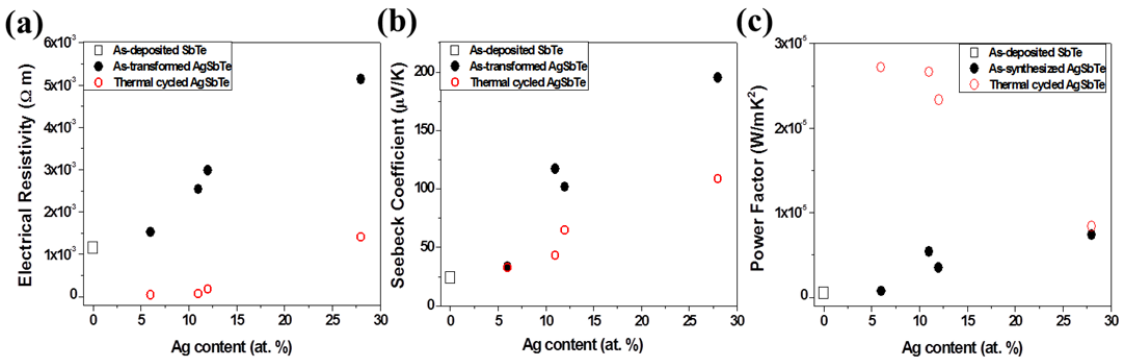


**Figure 3.11**: Composition-dependent electrical properties of the as-deposited $Sb_{54}Te_{46}$ thin film, the as-transformed $Ag_xSb_{1-x}Te_y$ thin films by the cation exchange reaction and the $Ag_xSb_{1-x}Te_y$ thin films crystalized by a thermal cycle: electrical resistivity (a), Seebeck coefficient (b) and thermoelectric power factor (c). The properties at room temperature are displayed.

In addition, the composition-dependent phase transition properties including phase transition temperature and the resistivity variation were analyzed as shown in Figure 3.12. For a non-volatile phase change memory application, the transition temperature and the resistivity variation are critical factors to reduce the power

consumption of the device [20-22]. Even though the near-stoichiometric $Ag_{28}Sb_{28}Te_{44}$ thin film displayed a higher transition temperature and a lower resistivity variation than the as-deposited $Sb_{54}Te_{46}$ thin film, the $Ag_6Sb_{53}Te_{41}$ film with an enhanced carrier concentration due to the increased Ag vacancies showed the low phase transition temperature of 323K and the high resistivity variation of 97%. The Ag-doped antimony telluride, not stoichiometric $AgSbTe_2$, demonstrated the most improved phase transition properties, which was comparable with the high performance demonstrated in the Ag-doped antimony telluride including $Ag_5In_5Sb_{60}Te_{30}$ (AIST) [18-20].

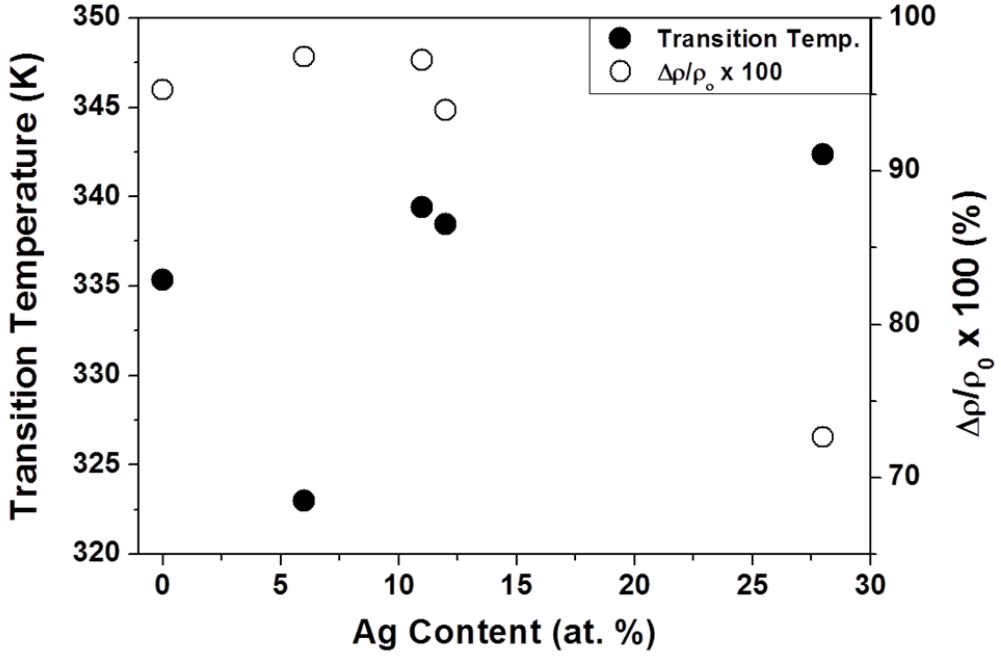


**Figure 3.12**: Transition temperature and resistivity variation due to the phase transition were analyzed as a function of the film composition.

### 3.2.5 Conclusions

In conclusion, the synthesis of ternary $Ag_xSb_{1-x}Te_y$ alloys was demonstrated by the cationic exchanged reaction of the thermally evaporated $Sb_{54}Te_{46}$ thin films. The cation exchange reaction for the synthesis of ternary $Ag_xSb_{1-x}Te_y$ alloys was estimated by the solubility of ionic solids, the conformity of crystal structure between a hexagonal structure of antimony telluride and a rock-salt structure of silver antimony telluride and the stress due to the volume expansion. The composition of the transformed $Ag_xSb_{1-x}Te_y$ thin films was controlled by the reaction time for the exchange between Ag and Sb cations. The temperature-dependent electrical properties (i.e., electrical resistivity, Seebeck coefficient and thermoelectric power factor) of the films showed a typical p-type degenerated semiconducting behavior with the phase transition behavior demonstrated at 323K to 343K. In addition, the electrical properties and phase transition properties were changed by the Ag vacancies as a p-type charge carrier. The electrical conductivity and Seebeck coefficients decreased with the increase of Ag vacancies, and the $Ag_6Sb_{53}Te_{41}$ thin film with high Ag vacancies demonstrated a low transition temperature and high resistivity variation.

### 3.2.6 References

[1] W. Heng, L. Jing-Feng, Z. Minmin and S. Tao, Synthesis and transport property of $AgSbTe_2$ as a promising thermoelectric compound, *Applied Physics Letters,* 2008. **93**: p. 202106

[2] E. F. Hockings, The thermal conductivity of silver antimony telluride, *Journal of Physics and Chemistry of Solids,* 1959. **10**: p. 341-342

[3] V. Jovovic and J. Heremans, Doping Effects on the Thermoelectric Properties of $AgSbTe_2$, *Journal of Electronic Materials,* 2009. **38**: p. 1504-1509

[4] D. T. Morelli, V. Jovovic and J. P. Heremans, Intrinsically Minimal Thermal Conductivity in Cubic I-V-$VI_2$ Semiconductors, *Physical Review Letters,* 2008. **101**: p. 035901

[5] T. Su, X. Jia, H. Ma, F. Yu, Y. Tian, G. Zuo, Y. Zheng, Y. Jiang, D. Dong, L. Deng, B. Qin and S. Zheng, Enhanced thermoelectric performance of $AgSbTe_2$ synthesized by high pressure and high temperature, *Journal of Applied Physics,* 2009. **105**: p. 073713-4

[6] T. Su, X. Jia, H. Ma, L. Zhou, J. Guo and N. Dong, Enhanced power factor of $Ag_{0.208}Sb_{0.275}Te_{0.517}$ prepared by HPHT, *Physics Letters A,* 2008. **372**: p. 515-518

[7] K. Wojciechowski, J. Tobola, M. Schmidt and R. Zybala, Crystal structure, electronic and transport properties of $AgSbSe_2$ and $AgSbTe_2$, *Journal of Physics and Chemistry of Solids,* 2008. **69**: p. 2748-2755

[8] S. N. Zhang, T. J. Zhu, S. H. Yang, C. Yu and X. B. Zhao, Phase compositions, nanoscale microstructures and thermoelectric properties in $Ag_{2-y}Sb_yTe_{1+y}$ alloys with precipitated $Sb_2Te_3$ plates, *Acta Materialia,* 2010. **58**: p. 4160-4169

[9] J. P. Heremans, V. Jovovic, E. S. Toberer, A. Saramat, K. Kurosaki, A. Charoenphakdee, S. Yamanaka and G. J. Snyder, Enhancement of Thermoelectric

Efficiency in PbTe by Distortion of the Electronic Density of States, *Science,* 2008. **321**: p. 554-557

[10] K. F. Hsu, S. Loo, F. Guo, W. Chen, J. S. Dyck, C. Uher, T. Hogan, E. K. Polychroniadis and M. G. Kanatzidis, Cubic $AgPb_mSbTe_{2+m}$: Bulk Thermoelectric Materials with High Figure of Merit, *Science,* 2004. **303**: p. 818-821

[11] G. J. Snyder and E. S. Toberer, Complex thermoelectric materials, *Nature Materials,* 2008. **7**: p. 105-114

[12] D. M. Rowe, *CRC Handbook of Thermoelectrics,* Boca Raton, CRC Press, Inc., 1995.

[13] J. D. Sugar and D. L. Medlin, Precipitation of $Ag_2Te$ in the thermoelectric material $AgSbTe_2$, *Journal of Alloys and Compounds,* 2009. **478**: p. 75-82

[14] B. Poudel, Q. Hao, Y. Ma, Y. Lan, A. Minnich, B. Yu, X. Yan, D. Wang, A. Muto, D. Vashaee, X. Chen, J. Liu, M. S. Dresselhaus, G. Chen and Z. Ren, High-Thermoelectric Performance of Nanostructured Bismuth Antimony Telluride Bulk Alloys, *Science,* 2008. **320**: p. 634-638

[15] J. M. O. Zide, D. Vashaee, Z. X. Bian, G. Zeng, J. E. Bowers, A. Shakouri and A. C. Gossard, Demonstration of electron filtering to increase the Seebeck coefficient in $In_{0.53}Ga_{0.47}As/In_{0.53}Ga_{0.28}Al_{0.19}As$ superlattices, *Physical Review B,* 2006. **74**: p. 205335

[16] J. Martin, L. Wang, L. Chen and G. S. Nolas, Enhanced Seebeck coefficient through energy-barrier scattering in PbTe nanocomposites, *Physical Review B,* 2009. **79**: p. 115311

[17] D. Vashaee and A. Shakouri, Improved Thermoelectric Power Factor in Metal-Based Superlattices, *Physical Review Letters,* 2004. **92**: p. 106103

[18] Y. S. Park, S. Y. Lee, S. M. Yoon, S. W. Jung, B. G. Yu, S. J. Lee and S. G. Yoon, Nonvolatile programmable metallization cell memory switching element based on Ag-doped SbTe solid electrolyte, *Applied Physics Letters,* 2007. **91**: p. 162107-3

[19] M. L. Lee, L. P. Shi, Y. T. Tian, C. L. Gan and X. S. Miao, Crystallization behavior of $Sb_{70}Te_{30}$ and $Ag_3In_5Sb_{60}Te_{32}$ chalcogenide materials for optical media applications, *physica status solidi (a),* 2008. **205**: p. 340-344

[20] M. Wuttig and N. Yamada, Phase-change materials for rewriteable data storage, *Nat Mater,* 2007. **6**: p. 824-832

[21] M. H. R. Lankhorst, B. W. S. M. M. Ketelaars and R. A. M. Wolters, Low-cost and nanoscale non-volatile memory concept for future silicon chips, *Nat Mater,* 2005. **4**: p. 347-352

[22] D. Yu, S. Brittman, J. S. Lee, A. L. Falk and H. Park, Minimum Voltage for Threshold Switching in Nanoscale Phase-Change Memory, *Nano Letters,* 2008. **8**: p. 3429-3433

[23] C. Frei, J. Schenzel, F. Waibel and D. Gunther, Stoichiometry of various Ag(In)SbTe phase change materials (PCMs) determined using LA-ICP-MS, *Journal of Analytical Atomic Spectrometry,* 2008. **23**: p. 217-222

[24] G. D. Moon, S. Ko, Y. Xia and U. Jeong, Chemical Transformations in Ultrathin Chalcogenide Nanowires, *ACS Nano,* 2010. **4**: p. 2307-2319

[25] U. Jeong, P. H. C. Camargo, Y. H. Lee and Y. Xia, Chemical transformation: a powerful route to metal chalcogenide nanowires, *Journal of Materials Chemistry,* 2006. **16**: p. 3893-3897

[26] B. Zhang, Y. Jung, H.-S. Chung, L. V. Vugt and R. Agarwal, Nanowire Transformation by Size-Dependent Cation Exchange Reactions, *Nano Letters,* 2009. **10**: p. 149-155

[27] S. E. Wark, C.-H. Hsia and D. H. Son, Effects of Ion Solvation and Volume Change of Reaction on the Equilibrium and Morphology in Cation-Exchange Reaction of Nanocrystals, *Journal of the American Chemical Society,* 2008. **130**: p. 9550-9555

[28] S. K. Mishra and et al., Electronic structure and thermoelectric properties of bismuth telluride and bismuth selenide, *Journal of Physics: Condensed Matter,* 1997. **9**: p. 461

[29] H. Zhang, C.-X. Liu, X.-L. Qi, X. Dai, Z. Fang and S.-C. Zhang, Topological insulators in $Bi_2Se_3$, $Bi_2Te_3$ and $Sb_2Te_3$ with a single Dirac cone on the surface, *Nat Phys,* 2009. **5**: p. 438-442

[30] R. Detemple, D. Wamwangi, M. Wuttig and G. Bihlmayer, Identification of Te alloys with suitable phase change characteristics, *Applied Physics Letters,* 2003. **83**: p. 2572-2574

[31] V. Jovovic and J. P. Heremans, Measurements of the energy band gap and valence band structure of $AgSbTe_2$, *Physical Review B,* 2008. **77**: p. 245204

# CHAPTER 4

# One Dimensional Chalcogenide Nanostructures

## 4.1 Lead Telluride Nanowires by Template-directed Method

### 4.1.1 Abstract

Single crystalline PbTe nanowires were potentiostatically electrodeposited by template directed method using track-etched polycarbonate membranes as scaffolds in acidic nitrate baths. They exhibited a face-centered cubic (FCC) structure with a preferred growth direction about 31° against [200] direction. By galvanic displacing the ends of PbTe nanowire with gold prior to electrode microfabrication, Schottky barrier (i.e. native PbTe oxide) at the interfaces between nanowire and electrodes was eliminated / reduced to form an ohmic contact between nanowire and electrodes. Field effect transistor (FET) transfer characteristics indicated that the electrodeposited single-crystalline PbTe nanowires are p-type semiconductors with the estimated field effect carrier mobility and concentration of 3.32 ± 0.15 $cm^2/Vs$ and 1.85 ±1.06 x $10^{18}$ $cm^{-3}$, respectively.

### 4.1.2 Introduction

Lead telluride (PbTe) is a narrow band-gap (~0.32 eV at 300K) semiconductor with a remarkably large Bohr exciton radius (~ 46 nm), excellent high quantum efficiencies, and a high thermoelectric figure-of-merit [1-4]. In addition, their electrical and optical properties of PbTe strongly depend on the composition which allows altering

peak wavelength and semiconducting characteristics [5]. Because of these unique properties, PbTe has attracted intense scientific interest with potential applications in infrared (IR) detectors, laser diodes, and thermophotovoltaics and thermoelectric devices [6-9].

One-dimensional nanostructures including nanowires and nanotubes have attracted a great attention to further enhance the thermoelectric performance compared to bulk counterparts because of greater phonon scattering at the interfaces with a minor reduction of electrical conduction [10-12]. A variety of physical and chemical techniques have been employed to synthesize PbTe nanowires in spite of the restriction of the cubic crystal structure favoring isotropic growth [13-15]. For example, the solution-based chemical synthesis (e.g. two-step hydrothermal and one-step solvothermal polyol processes) and chemical vapor deposition have been utilized to synthesize single-crystalline PbTe nanowires or nanocrystals. However, these methods typically lead to a broad size distribution in both diameter and length and require harsh operation conditions.[16-20] Template-directed electrodeposition is an efficient method to synthesize nanowires because it can precisely adjust composition, crystallographic structure, texture and grain size with controlled dimensions [5, 21-24]. Liu et al. demonstrated the ability to synthesize [111] preferred oriented PbTe single-crystalline nanowires using template directed electrodeposition using anodized alumina template as the scaffold [25]. Yang et al. synthesized polycrystalline PbTe nanowires using lithographically patterned nanowire electrodeposition (LPNE) method and demonstrated the ability to synthesize PbTe nanowires with controlled dimensions and composition [26, 27]. Our group also

systematically investigated electrodeposition of PbTe thin films in acidic nitrate baths utilizing various electrochemical and materials characterization techniques and demonstrated that crystal structures can be significantly altered by varying deposition potential and substrate [13, 21]. For example, single-crystalline PbTe cubes were electrodeposited on gold substrate by applying low overpotential [13].

In this paper, single-crystalline PbTe nanowires with [200] growth direction were potentiostatically electrodeposited in acidic nitrate baths and their morphology and crystallographic structure were investigated using SEM, TEM and HRTEM. To determine electrical properties of single nanowire, galvanic displacement process was added to conventional electrode fabrication processes to eliminate/reduce contact resistance between electrodes and nanowire. Using these single nanowire based devices, temperature dependent electrical resistance (TCR) and field effect transistor (FET) transport properties were performed to determine their electrical properties.

### 4.1.3 Experimental

PbTe nanowires were potentiostatically electrodeposited using track-etched polycarbonate (PC) membranes (a normal pore diameter of 30 nm from Whatman Inc.) as scaffolds in acidic nitric baths. To form a working electrode, gold was sputtered on the one side of a track-etched PC membrane to serve as a seed layer. The gold-sputtered PC membrane was attached to double-sided adhesive copper conducting tape, which was fixed on a glass slide.

PbTe electrolytes were prepared by dissolving $TeO_2$ (99.9995%, Alfa Aesar, Inc.) and $Pb(NO_3)_2$ (99.7%, Fisher Chemical) in concentrated $HNO_3$. Once oxide and salt were completely dissolved, deionized water was added to reach the final volume to make an electrolyte. The final concentration of $HTeO^{2+}$, $Pb^{2+}$ and $HNO_3$ in the electrolyte was 0.001, 0.05, and 1M, respectively. Ag/AgCl (in saturated KCl) was used as a reference electrode and a platinum-coated titanium strip was used as a counter electrode. The electrodeposition was carried out at an applied potential of -0.12 V vs Ag/AgCl with magnetic stirring (1 inch long magnetic bar and 300 rpm) at room temperature. After finishing the electrodeposition of PbTe, the track-etched PC membrane was detached from copper tape and dissolved in 1-methyl-2-pyrrolidinone (99.5%, Alfa Aesar, Inc.) at 50 $^{o}$C for a few hours to completely dissolve membrane. The suspended PbTe nanowires were centrifuged and then re-dispersed in isopropyl alcohol (IPA).

The chemical composition of PbTe nanowires was determined by an energy dispersive X-ray spectroscopy (EDS) (model: IncaX-Sight, Oxford Instrument). Scanning electron microscopy (SEM) (model: XLG-30FEG, Phillips) was used to observe surface morphology. The crystallography of nanowires was investigated using transmission electron microscopy (TEM) (model: JEM-2100F, JEOL) operated at 300 kV accelerating. High resolution transmission electron microscopy (HRTEM) image and selected area electron diffraction (SAED) pattern also were obtained for microstructural analysis.

Electrical properties of PbTe nanowire was measured using a source-measure unit (model: 2601A, Keithley) with cold-finger cryogenic system (model: CCS-350SH, Janis) by varying the temperature from 300 to 10 K. Back-gated FET measurement was

performed using a dual source-measure unit (model: 2636A, Keithley) at +0.5 V drain-source voltage (VDS) varying gate bias from -25 to 30 V.

### 4.1.4 Results and Discussion

The cathodic electrodeposition of PbTe thin film in acidic medium has been reported in the previous work [21], which consisted of two reaction steps as described in Equation 4.1.

$$HTeO_2^+(aq) + 3H^+(aq) + 4e^- \rightarrow Te(s) + 2H_2O$$
$$HTeO_2^+(aq) + Pb^{2+}(aq) + 3H^+(aq) + 6e^- \rightarrow PbTe(s) + 2H_2O \quad \text{Equation 4.1}$$

where PbTe were formed by the underpotential deposition (UPD) of $Pb^{2+}$ onto overpotential deposition of Te(s). Our prior work on the electrodeposition of PbTe thin films[13] indicated that deposition potentials greatly influenced crystallographic structure and morphology with a narrow deposition potential (E = -0.12 V vs. Ag/AgCl) which lead to the formation of single-crystalline cubes. Based on this work, the deposition potential was fixed at -0.12 V to form single-crystalline PbTe nanowires, even though the morphology, chemical composition and dimension of PbTe nanowires can be feasibly tailored by the applied potential and concentration of electrolytes [13, 21]. The electrodeposited PbTe nanowires had narrow size distribution of diameter of 73 ± 8.6 nm and length of 3.6 ± 0.34 μm and displayed the homogeneous morphologies. Figure 4.1 shows SEM and TEM images of electrodeposited PbTe nanowires. The PbTe nanowires

exhibit cigar shape which is pre-determined by the geometry of pores in a track-etched PC template. Obvious spot pattern from selected area electron diffraction (SAED) indicates that these nanowires were consisted of single-crystalline PbTe with face-entered cubic (FCC) structure with a lattice parameter of a=6.459 Å (inset at Figure 4.1 (b)). By comparing TEM image and the SAED pattern, it was determined that the growth direction of the nanowires has about 31° angle against [200] direction. It was also confirmed by HRTEM image of lattice fringes in figure 1c that PbTe nanowire exhibits a perfect order of crystalline lattice. The lattice spacing was measured to be approximately 0.321 nm which corresponded to the planes of FCC PbTe. The chemical composition of PbTe nanowires was measured to be approx. 42 at.% Pb which is somewhat off from the stoichiometric composition (50Pb50Te) with content variation of ±3 at.% along the longitudinal direction.

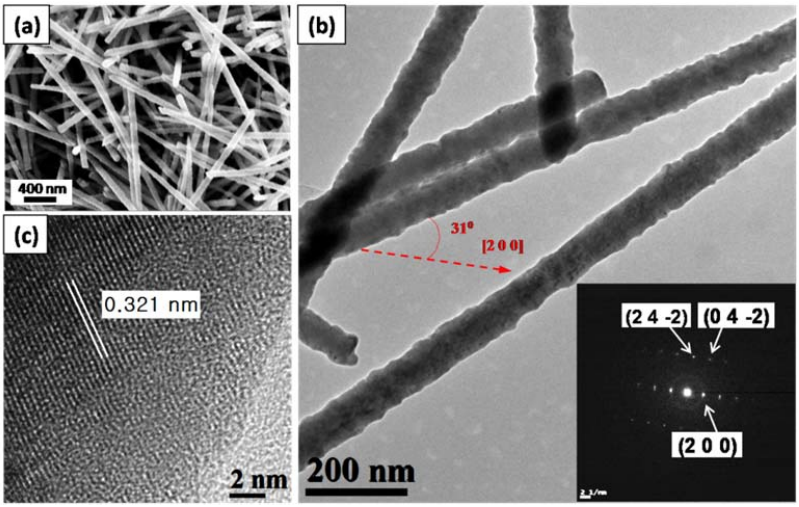


**Figure 4.1**: SEM and TEM images show electrodeposited PbTe nanowires at a potential of -0.12 V [vs. Ag/AgCl (sat. KCl)]: SEM (a), bright field TEM (with an inset of SAED pattern with zone axes of [0 1 2]) (b), and high resolution TEM image (c).

In order to improve device properties, it is critical to create an ohmic contact between nanowire and microfabricated electrodes [28]. It has been investigated to improve electrical contact issue, since device properties can be performed by material properties by themselves. Except noble nanostructures including gold, platinum, and palladium, it is difficult to form an ohmic contact to reactive nanostructures because of rapid formation of native oxide. The native oxide may result in an increase of contact resistance between nanowire and electrodes during the measurement of electrical property. Even though much more expensive procedure such as an e-beam lithography can include additional processes such as plasma etching to remove a native oxide layer or pattern four point probes to measure the resistance without contact resistance, a new cost-effective method to improve the contact was developed to measure "true" electrical property of single nanowire with minimum contact resistance, which is schematically illustrated in Figure 4.2. The newly developed contact method efficiently removed the local area of native oxide layer which minimize/eliminate of contact resistance. The fabrication processes are as following: Firstly, the PbTe nanowires were dispensed on a highly doped a p-type Si wafer with 300 nm thick $SiO_2$ layer, followed by patterning of electrode with exposing ends of PbTe nanowire (Figure 4.2 (a)). Prior to e-beam evaporation of electrode materials, the substrate was dipped into gold plating solution including 20 mM $Na_3Au(SO_3)_2$, ethylenediamine and potassium fluoride for 6 hours (Figure 4.2 (b)). During this process, the exposed sections of PbTe nanowire are galvanically displaced by gold ions which lead to the formation of gold nanoparticles on PbTe nanowire. Since galvanic displacement is an electrochemical process, gold

nanoparticles are directly formed on PbTe instead of native oxide (Figure 4.2 (c)). Galvanic displacement (sometimes referred to as immersion plating or cementation) is taking place because the reduction potential of a metal ion (i.e. gold ion) in solution is more positive than that of the sacrificial material (i.e. PbTe) [29, 30]. After galvanic displacement of PbTe nanowire ends, gold electrodes were formed by e-beam evaporation of Cr (20 nm thick) and Au (180 nm thick). Electrode was defined by lift-off techniques to form single nanowire based device (Figure 4.2 (d)). Figure 4.2 (e) and (f) show the surface morphologies of PbTe nanowire before and after galvanic displacement reaction, respectively. Formation of Au nanoparticles on the surface of PbTe nanowire was clearly observed (Figure 4.2 (f)).

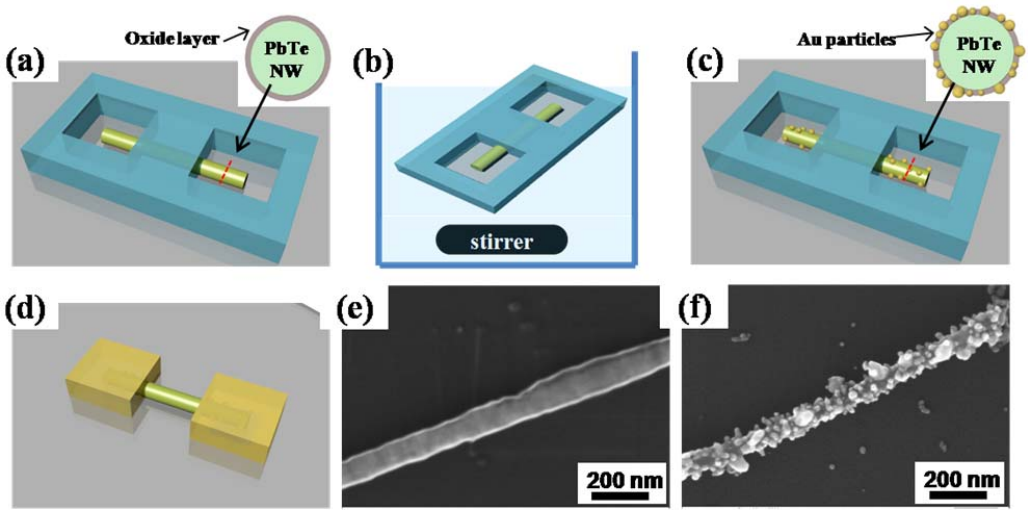


**Figure 4.2:** Schematic of a new contact method to minimize/eliminate a contact resistance between PbTe nanowire and Au electrode for measuring the electrical properties of PbTe nanowire; patterning of PR on a PbTe nanowire (a), dipping PbTe nanowire assembly into a electrolyte for galvanic displacement (b), formation of Au particles on ends of PbTe nanowire (c), formation of Au electrode at ends of PbTe nanowire (d), PbTe nanowire before galvanic displacement (e), and after galvanic displacement (f).

Figure 4.3 shows the I-V characteristics of PbTe nanowire with (a) and without (b) galvanic displacement process. The I-V curves of PbTe nanowire without galvanic displacement (Figure 3a) shows a non-linear behavior which indicates the presence of Schottky barrier at the interface between PbTe nanowire and gold electrodes. However, PbTe nanowire with galvanic displacement shows a linear I-V curve (Figure 4.3 (b)), which indicates that Schottky barrier which may be caused by native oxide layer on PbTe nanowire were eliminated/reduced by Au displacement process, and ohmic contacts were established.

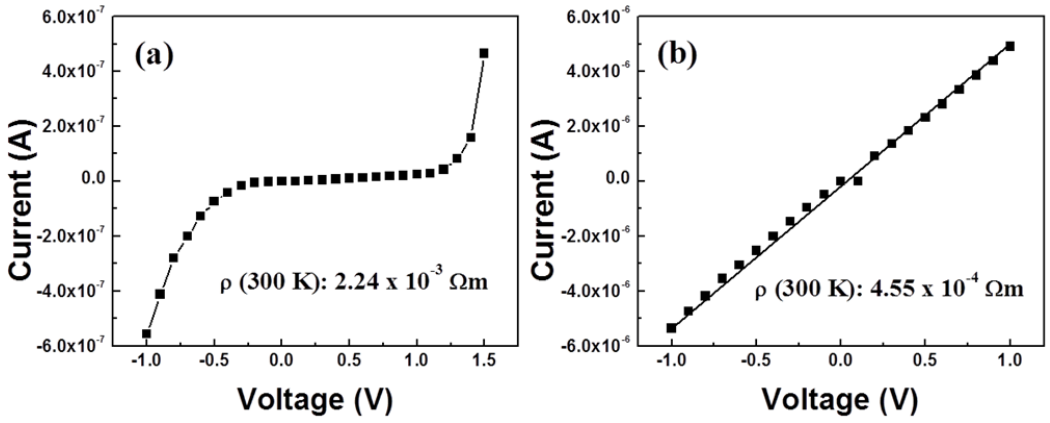


**Figure 4.3**: Comparison of I-V characteristics at the electrical contact between ends of PbTe nanowire and Au electrodes before (a) and after (b) galvanic displacement.

Figure 4.4 (a) shows temperature dependent I-V characteristics of single PbTe nanowire after galvanic displacement treatment at the temperature range of 10 to 300 K. The inset in figure 4a represents the electrode configuration of PbTe nanowire between two Au electrodes to measure electrical properties. Although the IV characteristic exhibited linear behavior at room temperature, the non-linear IV characteristic was

displayed at low temperature. Fermi level of p-type semiconductor at low temperature can be lower than acceptor energy level, even though materials have an ohmic contact at room temperature. As the results, the linear behavior of IV characteristics due to the ohmic contact can change to non-linear behavior. As expected, the resistance of PbTe nanowire decreased with increasing temperature as shown in Figure 4.4 (b), which indicates the semiconducting behavior of electron transport in the PbTe nanowire.

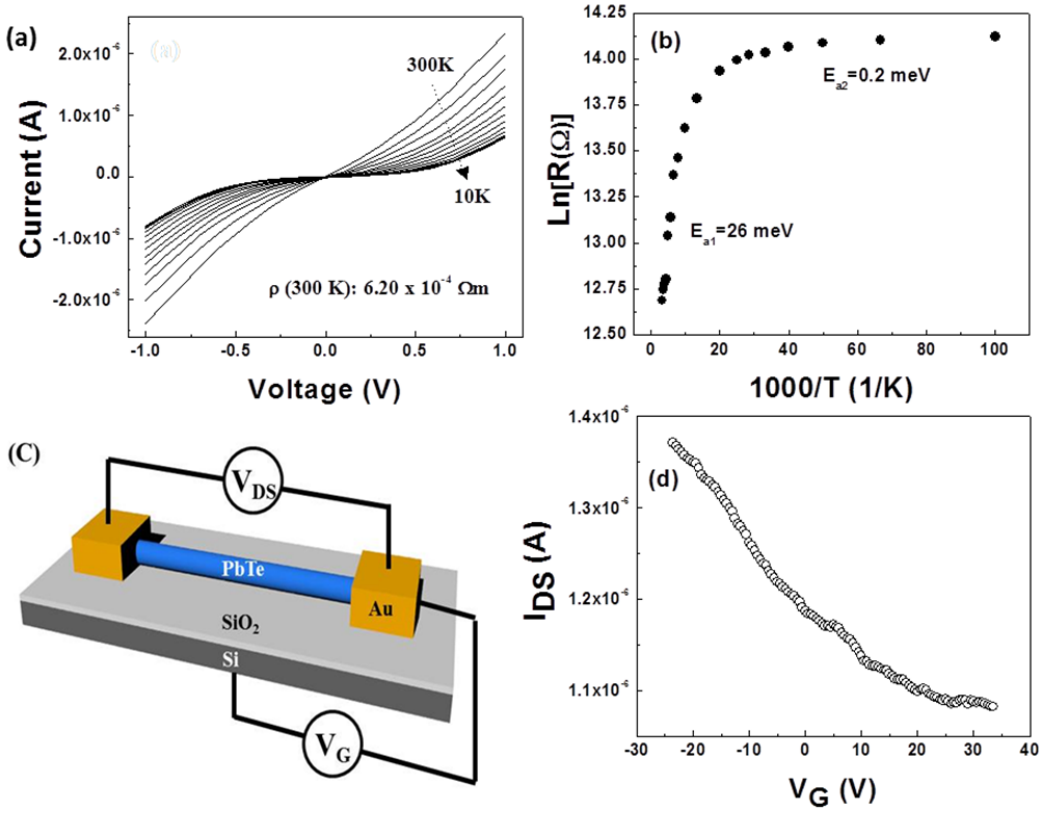


**Figure 4.4**: Electrical properties of single $Pb_{42}Te_{58}$ nanowire: I-V characteristics as a function of temperature (with the inset of single $Pb_{42}Te_{58}$ nanowire based device) (a), electrical resistance as a function of temperature with calculated activation energies (b), the schematic diagram of PbTe nanowire based device for back gate FET measurement (c) and FET transport properties with $V_{DS}$ of +0.5 V (d).

The thermal activation energy of PbTe nanowires, Ea, was estimated from Arrhenius equation, which can be expressed with the following Equation 4.1;

$$R = R_O \exp(-\frac{E_a}{2kT}) \qquad \text{Equation 4.1}$$

where $R_0$ is the resistance at T=∞, $E_a$ is the thermal activation energy for electrical conduction, k is Boltzmann's constant, and T is a temperature. From this relationship, $E_{a1}$ was calculated to be approx. 26 meV at the high temperature range of 100-300 K. However, the slope was significantly changed and leveled off at the low temperature range of below 40 K, and $E_{a2}$ was determined to be 0.2 meV in this temperature range. Compared to the intrinsic half energy band gap ($E_g$(300K)/2=160 meV), the small activation energy of about 26 meV at high temperature from 75 K to 300 K may be due to some acceptor-like energy levels of Te-rich PbTe with nonstoichiometric defects. The abnormal small activation energy at low temperature from 10 K to 50 K may be also attributed to excess Te (Pb vacancies) because highly doped PbTe can have acceptor levels with zero activation energy at 0 K [31, 32]. The transition behavior in the slope of resistance at the temperature range of 40 to 100 K strongly implies that the different electron transport mechanisms were existed at high and low temperatures region. Similar transitions of the slope at high temperature (~320K) were reported in PbTe [33] and CdSe [34] thin films. Abd El-Ati suggested that the transition of conductivity (from n-type to p-type) with temperature in PbTe thin films is attributable to the increase in the number of migrating Pb vacancies [34]. Also, it was reported that the predominant point defects are

Pb vacancies or Te interstitial acceptors in PbTe thin films. It is well-known that a PbTe thin film always has an excess of Te and the net hole concentration (p–n) can be altered by raising the temperature. Therefore, it is believed that the excess holes might be resulted from the ionization of acceptor defects due to the presence of an excess amount of Te [34]. According to Abd El-Ati, the increase of measuring temperature raises the number of ionized acceptor defects which migrate through the lattice to accumulate at the electrode surfaces. The transition point at high temperature (~320K) could not be observed in this study, because our measurement was carried out in the temperature range of 10 to 300K. However, such a transition of the slope at low temperature (~220K) in PbTe thin films was reported in other study [33, 36]. They also reported that the activation energy and transition point were measured to be ~0.106 eV and ~200 K, respectively. It is obvious that the carrier concentration increased with rising temperature as typical semiconducting behavior from the temperature dependence of electron transport in the PbTe nanowires. Therefore, it is believed that electrical conducting mechanism may be dominated by different impurity energy levels with increasing temperature.

Using a few single nanowire based FET devices, the electrical transport properties of single nanowire were characterized in two-terminal configuration with the underlying Si substrate as the back gate electrode on 100 nm thick $SiO_2$ dielectric layer as illustrated in the schematic diagram of figure 4c. The gate voltage was swept from -25 V to 35 V at fixed drain-source voltage of +0.5 V. Figure 4d shows a typical $I_{DS}$-$V_G$ curve with a fixed $V_{DS}$ of +0.5 V, the channel current, $I_{DS}$, continuously decreased with increasing gate

potential, $V_G$, which indicated that electrodeposited PbTe nanowires is a p-type semiconductor. Even though the charge transport mechanism from transistor characteristic analysis was not investigated in detail due to the limit of dielectric layer durability and instability of PbTe nanowire in air during the measurement, the field effect carrier concentration and mobility was determined using following Equation 4.2 and 4.3:

$$p = \frac{CV_{th}}{e\pi r^2 L} = \left(\frac{V_{th}}{e\pi r^2}\right) \times \left(\frac{2\pi\varepsilon\varepsilon_0}{\ln(2t/r)}\right) \qquad \text{Equation 4.2}$$

$$\mu = \frac{dI}{dV_G}\frac{L^2}{CV_{DS}} \qquad \text{Equation 4.3}$$

where C is nanowire capacitance, $V_{th}$ is threshold voltage, and r and L are the radius and length of nanowires, respectively. The capacitance of nanowire with respect to the back gate can be described with t being the thickness and the average dielectric constant of dielectric layer (300 nm thick $SiO_2$ with ε of 3.9). The mobility was determined by the measurement of transconductance ($dI/dV_G$). Based on the $I_{DS}$-$V_G$ curves, FET hole mobility and carrier concentration were determined to be 3.32±0.15 $cm^2/Vs$ and 1.8 ± 1.06 $x10^{18}$ $cm^{-3}$, respectively. Compared to CVD- and CVT-PbTe nanowires, electrodeposited PbTe nanowires show greater field effect mobility. Table 4.1 compared the electrical properties of PbTe nanowires [17-19, 26, 27, 37]. Electrical measurement in the literature was carried out with PbTe nanowires and PbTe nanowire films excluding

contact resistance which was produced by four point probe technique or post-etching process.

**Table 4.1**: Comparison of the electrical transport properties of PbTe nanowires

| Diameter (nm) | Synthesis Method | Carrier Type | Resistivity ($10^{-3}$ Ωm) | Field Effect Mobility ($cm^2/Vs$) | Carrier Concentration ($10^{18}$ $cm^{-3}$) | Ref |
|---|---|---|---|---|---|---|
| 50-70 | ED | P-type | 0.27±0.15 | 3.32±0.15 | 1.85±1.06 | This work |
| 20x84 | ED | N-type | 0.1 to 0.5 (no thermal treatment)<br>15.9 to 28.6 (thermal treatment) | ~ 40<br>3 to 7 | ---- | 26, 27 |
| 10-30 | Solvo-thermal | P-type | 2 | ---- | ---- | 18 |
| 83 | CVD | P-type | 1.2 | 0.71 | 84 | 19 |
| 60 | CVT | N-type | ~7 | 0.83 | 0.88 | 37 |
| 30 | Hydrothermal | P-type | 8.8 | ---- | ---- | 17 |

ED: Electrodeposition, CVD: Chemical vapor deposition, CVT: Chemical vapor transport method

### 4.1.5 Conclusions

In this paper, single crystalline PbTe nanowires with a preferred growth direction about 31° against [200] direction were synthesized by electrodeposition in acidic nitrate baths. Galvanic displacement reaction process was introduced to deposit gold nanoparticles on PbTe nanowires to minimize/eliminate contact resistance between PbTe nanowire and electrodes. Electron-transport properties of these nanowires indicated that

the electrodeposited PbTe nanowire is low doped p-type semiconductor with excellent field effect mobility.

### 4.1.6 References


[1] J. J. Urban, D. V. Talapin, E. V. Shevchenko and C. B. Murray, Self-Assembly of PbTe Quantum Dots into Nanocrystal Superlattices and Glassy Films, *Journal of the American Chemical Society,* 2006. **128**: p. 3248-3255

[2] J. E. Murphy, M. C. Beard, A. G. Norman, S. P. Ahrenkiel, J. C. Johnson, P. Yu, O. I. Micic, R. J. Ellingson and A. J. Nozik, PbTe Colloidal Nanocrystals:Synthesis, Characterization, and Multiple Exciton Generation, *Journal of the American Chemical Society,* 2006. **128**: p. 3241-3247

[3] T. M. Tritt, THERMOELECTRIC MATERIALS: Holey and Unholey Semiconductors, *Science,* 1999. **283**: p. 804-805

[4] Y. Gelbstein, Z. Dashevsky and M. P. Dariel, High performance n-type PbTe-based materials for thermoelectric applications, *Physica B: Condensed Matter,* 2005. **363**: p. 196-205

[5] F. Xiao, C. Hangarter, B. Yoo, Y. Rheem, K.-H. Lee and N. V. Myung, Recent progress in electrodeposition of thermoelectric thin films and nanostructures, *Electrochimica Acta,* 2008. **53**: p. 8103-8117

[6] B. A. Akimov and et al., Low-temperature switching in PbTe(Ga) at high electric fields, *Semiconductor Science and Technology,* 1993. **8**: p. S447

[7] Z. Feit, D. Kostyk, R. J. Woods and P. Mak, Single-mode molecular beam epitaxy grown PbEuSeTe/PbTe buried-heterostructure diode lasers for $CO_2$ high-resolution spectroscopy, *Applied Physics Letters,* 1991. **58**: p. 343-345

[8] T. C. Harman, P. J. Taylor, M. P. Walsh and B. E. LaForge, Quantum Dot Superlattice Thermoelectric Materials and Devices, *Science,* 2002. **297**: p. 2229-2232

[9] X. Li and I. S. Nandhakumar, Direct electrodeposition of PbTe thin films on n-type silicon, *Electrochemistry Communications,* 2008. **10**: p. 363-366

[10] L. D. Hicks and M. S. Dresselhaus, Thermoelectric figure of merit of a one-dimensional conductor, *Physical Review B,* 1993. **47**: p. 16631

[11] A. Majumdar, MATERIALS SCIENCE: Enhanced: Thermoelectricity in Semiconductor Nanostructures, *Science,* 2004. **303**: p. 777-778

[12] D. Natelson, Nanofabrication: Best of both worlds, *Nat Mater,* 2006. **5**: p. 853-854

[13] F. Xiao, B. Yoo, K. N. Bozhilov, K. H. Lee and N. V. Myung, Electrodeposition of Single-Crystal Cubes of Lead Telluride on Polycrystalline Gold Substrate, *The Journal of Physical Chemistry C,* 2007. **111**: p. 11397-11402

[14] B. Zhang, J. He and T. M. Tritt, Size-selective high-yield growth of lead telluride (PbTe) nanocrystals using a chemical vapor deposition technique, *Applied Physics Letters,* 2006. **88**: p. 043119-3

[15] G. Zhang, X. Lu, W. Wang and X. Li, Facile Synthesis of a Hierarchical PbTe Flower-like Nanostructure and Its Shape Evolution Process Guided by a Kinetically Controlled Regime, *Chemistry of Materials,* 2007. **19**: p. 5207-5209

[16] G. Tai, W. Guo and Z. Zhang, Hydrothermal Synthesis and Thermoelectric Transport Properties of Uniform Single-Crystalline Pearl-Necklace-Shaped PbTe Nanowires, *Crystal Growth & Design,* 2008. **8**: p. 2906-2911

[17] G. a. Tai, B. Zhou and W. Guo, Structural Characterization and Thermoelectric Transport Properties of Uniform Single-Crystalline Lead Telluride Nanowires, *The Journal of Physical Chemistry C,* 2008. **112**: p. 11314-11318

[18] Q. Yan, H. Chen, W. Zhou, H. H. Hng, F. Y. C. Boey and J. Ma, A Simple Chemical Approach for PbTe Nanowires with Enhanced Thermoelectric Properties, *Chemistry of Materials,* 2008. **20**: p. 6298-6300

[19] M. Fardy, A. I. Hochbaum, J. Goldberger, M. M. Zhang and P. Yang, Synthesis and Thermoelectrical Characterization of Lead Chalcogenide Nanowires, *Advanced Materials,* 2007. **19**: p. 3047-3051

[20] A. Purkayastha, Q. Yan, D. D. Gandhi, H. Li, G. Pattanaik, T. Borca-Tasciuc, N. Ravishankar and G. Ramanath, Sequential Organic-inorganic Templating and Thermoelectric Properties of High-Aspect-Ratio Single-Crystal Lead Telluride Nanorods, *Chemistry of Materials,* 2008. **20**: p. 4791-4793

[21] F. Xiao, B. Yoo, M. A. Ryan, K.-H. Lee and N. V. Myung, Electrodeposition of PbTe thin films from acidic nitrate baths, *Electrochimica Acta,* 2006. **52**: p. 1101-1107

[22] M. S. Sander, R. Gronsky, T. Sands and A. M. Stacy, Structure of Bismuth Telluride Nanowire Arrays Fabricated by Electrodeposition into Porous Anodic Alumina Templates, *Chemistry of Materials,* 2003. **15**: p. 335-339

[23] M. S. Sander, A. L. Prieto, R. Gronsky, T. Sands and A. M. Stacy, Fabrication of High-Density, High Aspect Ratio, Large-Area Bismuth Telluride Nanowire Arrays by Electrodeposition into Porous Anodic Alumina Templates, *Advanced Materials,* 2002. **14**: p. 665-667

[24] A. L. Prieto, M. S. Sander, M. S. Martin-Gonzalez, R. Gronsky, T. Sands and A. M. Stacy, Electrodeposition of Ordered $Bi_2Te_3$ Nanowire Arrays, *Journal of the American Chemical Society,* 2001. **123**: p. 7160-7161

[25] W. Liu, W. Cai and L. Yao, Electrochemical Deposition of Well-ordered Single-crystal PbTe Nanowire Arrays, *Chemistry Letters,* 2007. **36**: p. 1362-1363

[26] Y. Yang, S. C. Kung, D. K. Taggart, C. Xiang, F. Yang, M. A. Brown, A. G. G. ell, T. J. Kruse, J. C. Hemminger and R. M. Penner, Synthesis of PbTe Nanowire Arrays using Lithographically Patterned Nanowire Electrodeposition, *Nano Letters,* 2008. **8**: p. 2447-2451

[27] Y. Yang, D. K. Taggart, M. H. Cheng, J. C. Hemminger and R. M. Penner, High-Throughput Measurement of the Seebeck Coefficient and the Electrical Conductivity of Lithographically Patterned Polycrystalline PbTe Nanowires, *The Journal of Physical Chemistry Letters,* 2010. **1**: p. 3004-3011

[28] C. M. Hangarter, M. Bangar, S. C. Hernandez, W. Chen, M. A. Deshusses, A. Mulchandani and N. V. Myung, Maskless electrodeposited contact for conducting polymer nanowires, *Applied Physics Letters,* 2008. **92**: p. 073104-3

[29] C. Carraro, R. Maboudian and L. Magagnin, Metallization and nanostructuring of semiconductor surfaces by galvanic displacement processes, *Surface Science Reports,* 2007. **62**: p. 499-525

[30] F. Xiao, B. Yoo, K. H. Lee and N. V. Myung, Synthesis of $Bi_2Te_3$ Nanotubes by Galvanic Displacement, *Journal of the American Chemical Society,* 2007. **129**: p. 10068-10069

[31] Y. I. Ravich, B. A. Efimova and I. A. Smirnov, *Semiconducting Lead Chalcogenides,* New York, Plenum Press, 1970.

[32] M. P. Dariel, Z. Dashevsky, A. Jarashnely, S. Shusterman and A. Horowitz, Carrier concentration gradient generated in p-type PbTe crystals by unidirectional solidification, *Journal of Crystal Growth,* 2002. **234**: p. 164-170

[33] V. Sandomirsky, A. V. Butenko, I. G. Kolobov, A. Ronen, Y. Schlesinger, A. Y. Sipatov and V. V. Volubuev, Highly resistive p-PbTe films with carrier concentration as low as $10^{14}$ $cm^{-3}$, *Applied Physics Letters,* 2004. **84**: p. 3732-3734

[34] M. Abd El-Ati, Electrical conductivity of PbTe thin films, *Physics of the Solid State,* 1997. **39**: p. 68-71

[35] M. M. A. Sekkina, A. Tawfik and M. I. Abd El-Ati, Novel studies on the temperature-dependence of electric and photovoltaic properties of thin CdSe films

for solar cells, *Journal of Thermal Analysis and Calorimetry,* 1985. **30**: p. 753-761

[36] F. Terra and G. Mahmoud, Low temperature effects on the galvanomagnetic properties of thin PbTe films, *Journal of Materials Science: Materials in Electronics,* 1997. **8**: p. 43-46

[37] S. Y. Jang, H. S. Kim, J. Park, M. Jung, J. Kim, S. H. Lee, J. W. Roh and W. Lee, Transport properties of single-crystalline n-type semiconducting PbTe nanowires, *Nanotechnology,* 2009. **20**: p. 415204

## 4.2 Tellurium Nanoribbons by Lithographically Patterned Nanowires Electrodeposition

### 4.2.1 Abstract

We investigated sensing properties of single tellurium nanoribbon based nano-devices aligned at well-defined locations using a lithographically patterned nanowire electrodeposition (LPNE) technique. Electrical resistivity and FET properties were characterized as a function of the tailored width of Te nanoribbons, which described different morphology/crystallinity of nanoribbons depending on their width. Sensor performance on detecting $NO_x$ (g) as a function of the tailored width of Te nanoribbons was investigated by the modified conductive channel and crystallinity of the fabricated Te nanoribbons. A sensitivity of 24±3.5% on detecting $NO_x$ (g) at a concentration of 10 ppm was demonstrated by single Te nanoribbon based sensor with a width of 57±7 nm which had an ohmic contact between the nanoribbon and Au/Cr electrode. Sensing properties of Te nanoribbons with similar width were measured as a function of $NO_x$ (g) concentration in the sensor devices of different electrical contact types. Single Te nanoribbon based devices with Schottky contact demonstrated enhanced sensing performance. Analysis of the effects of annealing on sensing properties have shown that the annealed Te nanoribbons demonstrated the improved sensitivity, even though the electrical contact type was changed from Schottky to ohmic contact.

### 4.2.2 Introduction

Advancements in nanotechnology have greatly improved the performance of various electrical and optical devices. In recent years, nanostructured sensors have been developed to enhance sensing properties [1-11]. 1-Dimensional nanostructures are significantly attractive as sensor devices, since they can demonstrate high surface to volume ratio, adjustability of Debye length comparable to wire diameter, low power consumption and dual functionality as both devices and interconnectors. Even though the application of 1-dimensional nanostructures to sensors has demonstrated enhanced sensing properties such as high sensitivity and rapid response/recovery time, fabrication of 1-dimensional nanostructured device architectures has been restricted by the need for complex and expensive micro/nano-fabrication procedures. Penner, et al. reported a lithographically patterned nanowires electrodeposition (LPNE) technique as an effective technique for fabricating single nanowire based devices [5, 12-15]. The dimensions and geometries of LPNE-nanowires on a device can be easily controlled in a cost-effective and straightforward process, since photolithography and electrodeposition techniques were combined to synthesize complex high density nanowires to pre-determined locations.

Semiconductor gas sensors have attracted considerable attention because they can demonstrate low power consumable and compact devices with high sensing properties. Various semiconducting metal oxides such as $SnO_2$, ZnO, $WO_3$ and $In_2O_3$ have been developed for demonstration of high performance gas sensors [16-23]. However, the metal oxide gas sensors must be operated at a high temperature, which requires the

integration of heaters and thermo-sensors into the device in addition to gas sensing parts. The high temperature operation of the sensor devices invokes unavoidable problems, such as low durability and high power consumption. Even though carbon nanotube based gas sensor devices have demonstrated room temperature operation and high sensitivity, the sensors have revealed a lack of selectivity and long recovery time [1, 7, 8, 24-26].

Recently, Te thin film and dispersed 1-dimensional Te film based gas sensors have been reported as high performance gas sensor devices operable at room temperature [27-34]. Tellurium is a p-type semiconducting material with a narrow band gap of 0.35 eV at room temperature. Many methods such as solvothermal/hydrothermal methods, galvanic displacement reaction, electrodeposition, chemical vapor deposition, and microwave-assisted methods have been developed to synthesize 1-dimensional Te nanostructures. Despite the range of methods available, gas sensing properties of single 1-dimensional Te nanostructures have not been demonstrated due to the complex and difficult procedure for the construction of devices with aligned 1-dimensional Te nanostructures.

Various approaches have been developed to improve sensing properties of devices in mainly three aspects [10, 11]: i) Receptor function can be tuned by modification of surface morphology, chemical functional groups and decoration of catalytic metals [19, 30, 35-38], ii) Transducer function can be improved by tuned microstructures of materials [19, 38-40], and iii) Detection function in devices is also a critical factor to improve sensing properties, which can be tailored by devices (Schottky diodes) with modulated contacts between sensing materials and electrodes [9, 41-43].

In this paper, we electrodeposited Te nanoribbons on photo-lithographically patterned nickel substrate layers. The shape, composition, and dimension of nanoribbons were feasibly tailored by adjusting deposition conditions. Temperature dependent electrical properties and FET properties of single Te Nanoribbon based nano-device were investigated. Sensitivity of single Te nanoribbons on $NO_x$ (g) were estimated based on a width of the nanoribbon, type of the electrical contact (ohmic and Schottky), and annealing process.

### 4.2.3 Experimental

Single Te nanoribbon based sensor devices were fabricated by typical LPNE procedure as illustrated in Figure 4.5 [5, 14]. Thermally oxidized silicon dioxide with thickness of 300 nm on commercial p-type silicon wafer (Ultrasil Corperation) was employed as a substrate. Sacrificial nickel layer with thickness of 100 nm was deposited at a rate of 1.0 Å/s by e-beam evaporator (Tamescal BJD-1800) (Figure 4.5 (a)). A photoresist layer (PR) (Rohm and HAAS Electronic Material, S1813) was spin-coated with an adhesion promoter (Microelectronic Material, Primer P20) followed by UV exposure to make a pattern as described in a previous report (Figure 4.5 (b)) [5]. The exposed sacrificial Ni layer was etched by a Ni etchant (Transene Company Inc., TFB) (Figure 4.5 (c)). After chemical etching to remove the exposed Ni, the Ni layer was excessively etched by electrochemical etching to undercut a Ni layer, through application of a potential of 0.02 V (vs. SCE) with a Pt-coated Ti sheet as a counter electrode for 5 min in the electrolyte of 0.1 M KCl and 24 mM HCl, where the undercut depth was

10±1.2 μm (Figure 4.5 (d)). The undercut Ni nanoband was utilized as a working electrode for electrodeposition of Te. Te nanoribbons were electrodeposited by pulsed potential of -0.15 V (vs. Ag/AgCl (sat. NaCl)) with duty cycle of 0.083 ($T_{on}$ of 10 ms and $T_{off}$ of 110 ms) in the electrolyte of 10 mM $TeO_2$ and 1M $HNO_3$ (Figure 4.5 (e)). The widths of the Te nanoribbons were varied by controlling the deposition time from 5 to 30 sec. Electrodeposition was conducted with a potentiostat (Princeton Applied Research VMP-2). After the electrodeposition of Te, PR and sacrificial Ni residues were removed by acetone and 2 % (V/V) $HNO_3$ (Figure 4.5 (f)). To investigate electrical and sensing properties of a single Te nanoribbon, gold/chromium micro-electrodes with thicknesses of 180nm/20nm were subsequently e-beam evaporated on top of the nanoribbons patterned by typical lithographical procedure (Figure 4.5 (h)). The morphologies of Te nanoribbons were analyzed by scanning electron microscope (SEM) (XL30-FEG, Phillips) and atomic force microscope (AFM) (Veeco, Inova SPM).

Electrical resistivity and field effect transistor (FET) properties of single Te nanoribbon with different widths were measured with source meter (Kiethley, 2636A) in the gate voltage ($V_G$) being swept from -20 V to 20 V at a fixed drain-source voltage ($V_{DS}$) of 0.5 V, and the I-V curves being characterized at different $V_G$ ranging from -15 V to 15 V. Temperature dependent electron transport properties were measured by an custom-made cryogenic system linked with a temperature controller (Lakeshore, 331) and source-meter (Kiethley, 2636A). The gas sensing performance of single Te nanoribbon was investigated with $NO_x$ (g) whose concentrations were controlled by

Labview programmed mass flow controllers (MFC) (Alicat Sci., MC-50SCCM-D) with a source-measure unit (Kiethley, 236) in a custom-made sensing system.

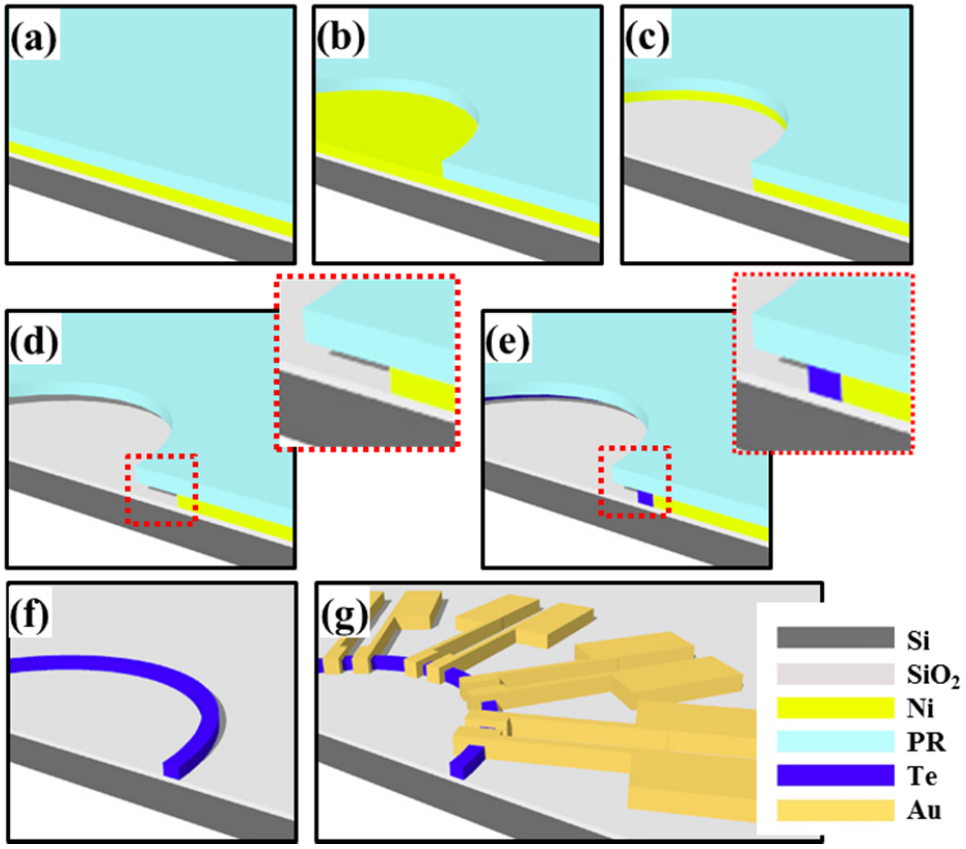


**Figure 4.5**: Schematic diagram of Te nanoribbon synthesis by Lithographical Patterned Nanowire Electrodeposition (LPNE); After thermal oxidation of Si wafer to $SiO_2$ layer followed by the photolithographic patterning of align marks and e-beam evaporated Ni layer (100 nm thickness), PR was spun on the sacrificial Ni layer (a). PR was patterned by UV exposure under photo-mask and development (b). The exposed sacrificial Ni layer was chemically etched (c). The sacrificial layer was electrochemically etched to create the undercut trench (d). Te nanoribbons were electrodeposited using the exposed Ni nanoband as a working electrode (e). The patterned Te nanoribbons on wafer were obtained after PR and Ni layers were removed by acetone and diluted nitric acid (f). Finally, Cr and Au were e-beam deposited by the photolithographic patterning to form electrical contacts (g).

### 4.2.4 Results and Discussion

Even though Te thin films have been demonstrated as high performance gas sensor devices operable at room temperature, sensing properties of single 1-dimensional Te nanostructured devices have not been studied due to intricate fabrication processes. LPNE can be utilized as an effective technique for fabrication of single nanoribbon based gas sensors. Single Te nanoribbon based chemiresistive gas sensors were fabricated as described in Figure 4.5. Electrodeposition of Te on the undercut Ni nanoband was conducted by applying pulsed potentials with a duty cycle of 0.083. Pulse plating can reduce internal stress and porosity of electrodeposits over dc plating because of the increased nucleation rate. Electrodeposition of Te on a sacrificial Ni layer can be depicted by following Equation 4.4. The geometry and thickness of Te nanoribbons can be determined by the designed lithographical pattern and the thickness of e-beam evaporated sacrificial layers, respectively.

$$HTeO_2^+(aq) + 3H^+(aq) + 2Ni^0(s) \rightarrow Te^0(s) + 2H_2O + 2Ni^{2+} \qquad \text{Equation 4.4}$$

Figure 4.6 describes SEM and AFM images of electrodeposited Te nanoribbons between Au/Cr electrodes, where each chip consists of 16 channels (Figure 4.6 (inset)). The widths of Te nanoribbons were tailored by duration of pulse plating. Te nanoribbons with different widths of 52±7 nm and 169±24 nm were electrodeposited at the duration time of 5 sec and 30 sec, respectively, as shown in Figure 4.6 (b) and 4.6 (c). A nanoribbon with a larger width of 169±24 nm displayed rough morphology (Ra = 41.2

nm), compared to the roughness of Te nanoribbon with a width of 52±7 nm (Ra = 17.9 nm).

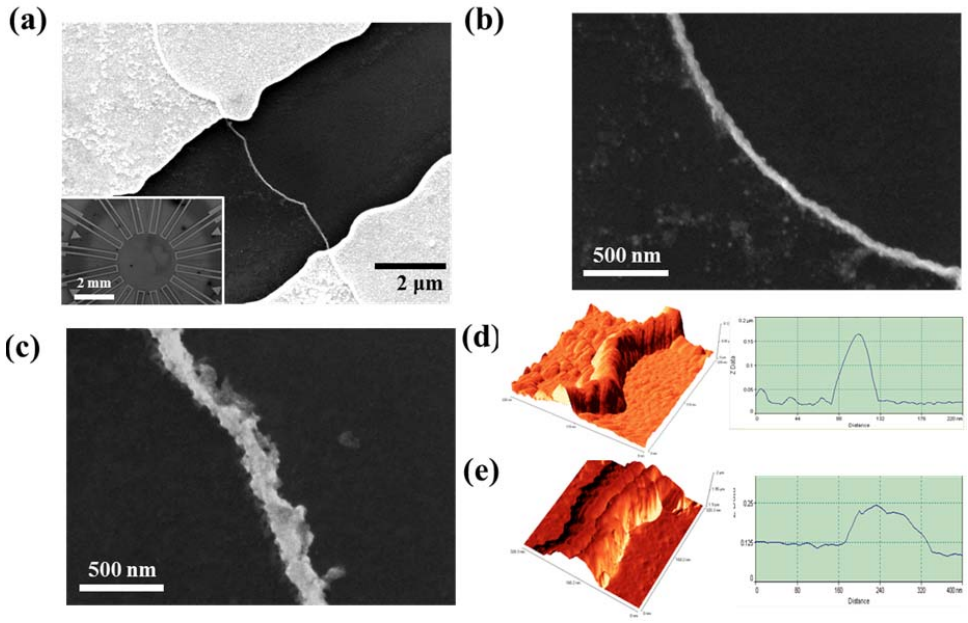


**Figure 4.6**: SEM image of single Te nanoribbon based device (inset: gas sensor device of aligned single Te nanoribbon in wafer batch) (a), Morphologies of Te naoribbon of 52±7 nm width (b) and 169±24 nm width (c), 3-D AFM images and profiles of Te nanoribbons of 52±7 nm width (d) and 169±24 nm width (e).

Electron transport properties of single Te nanoribbon with different width were investigated as shown in Figure 4.7. Back-gate FET properties were measured by sweeping $V_{DS}$ with the variation of fixed $V_G$ (Figure 4.7 (a)) and sweeping $V_G$ at fixed $V_{DS}$ (Figure 4.7 (a) (inset)), which shows a typical p-type semiconducting behavior. Electrical resistivity of Te nanoribbons increased with the increasing width of the nanoribbons, which may be attributed to their deteriorated morphology and crystallinity (Figure 4.7 (b)). The enhancement of FET mobility with decreased width of the

nanoribbons corresponds with the resistivity variation, which can be attributed to decreased scattering factors due to the improved crystallinity (Figure 4.7 (c)). However, the variation of FET carrier concentration did not correlate with changes in the width of Te nanoribbons (Figure 4.7 (d)).

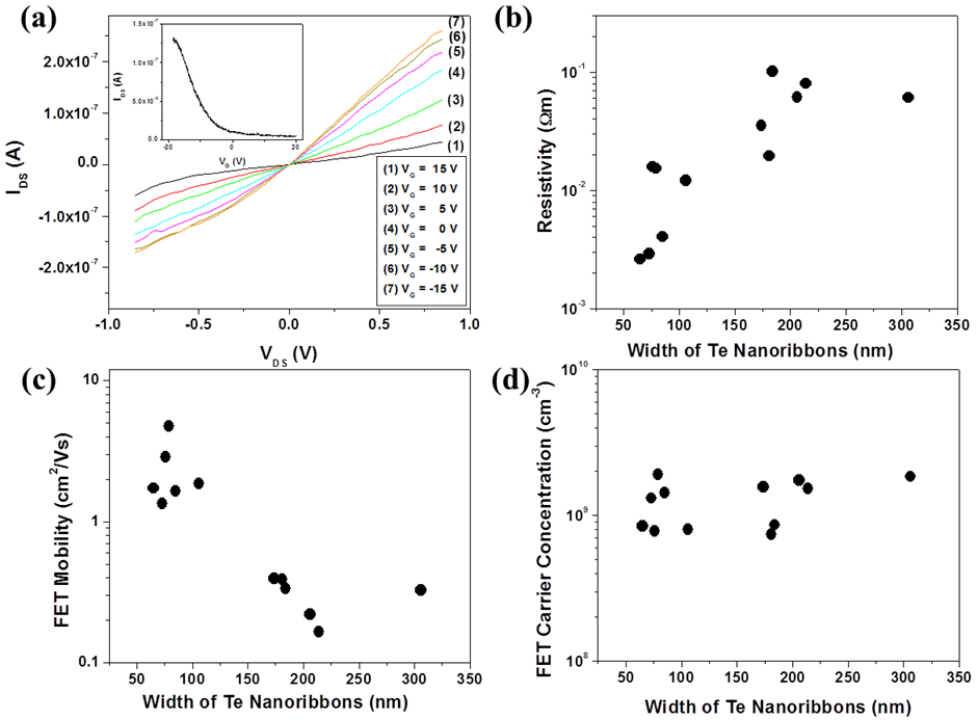


**Figure 4.7**: $I_{DS}$-$V_{DS}$ characteristics of Te nanoribbons with the width of 106±19 nm at different $V_G$ ranged from -15 V to 15 V (a) (inset: $I_{DS}$-$V_G$ curve at $V_{DS}$ of 0.5 V), and electrical resistivity (b), FET mobility (c) and FET carrier concentration (d) as a function of the width of Te nanoribbons.

Figure 4.8 shows gas sensing properties on $NO_x$ (g) of single Te nanoribbon based devices as a function of the width of the nanoribbons. Sensitivities on $NO_x$ (g) with controlled concentrations from 0.1 ppm to 10 ppm were described in sensor devices of single Te nanoribbons with the width of 95±12 nm (Figure 4.8 (a)) and of 57±7 nm

(Figure 4.8 (b)). The reduced resistance of Te nanoribbon on adsorbed $NO_x$ (g) displayed typical p-type sensing material behavior on electron withdrawing analyte gases. In order to exclude the effect of electrical contact types on sensitivity, the sensitivity of Te nanoribbons with ohmic contacts of linear $I_{DS}$-$V_{DS}$ characteristics was plotted on $NO_x$ (g) of 10 ppm as a function of the width of nanoribbons (Figure 4.8 (c)). Observation of the dependence of electrical properties on the dimension of nanoribbons showed that Te nanoribbons with reduced width demonstrated the improved sensitivity on $NO_x$ (g). Even though Debye length (δ) for the improvement of sensing performance has been typically tailored by carrier concentration of materials, the enhanced mobility of nanoribbons with reduced width can improve the conductivity of channel with respect to developing the transducer function of gas sensor device. Additionally, the reduced dimension of transducers can reduce conductive channel due to a relatively increased Debye length as described in Figure 4d, resulting in an enhancement of the sensitivity of sensor devices [10]. The sensitivity, $\Delta R' = (R' - R_0)/R$, of materials with smaller dimensions is higher than the sensitivity, $\Delta R = (R - R_0)/R$, of larger materials (Figure 4.8 (d)).

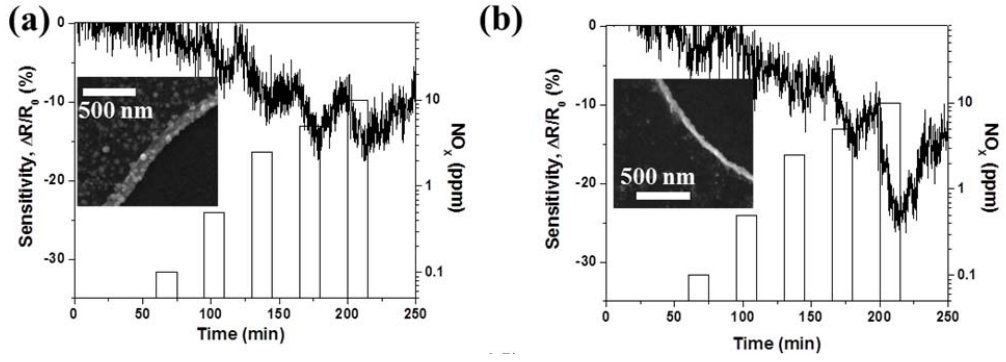

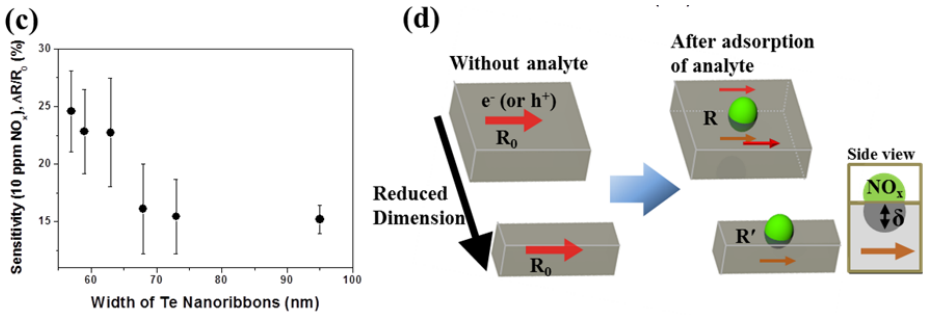


**Figure 4.8**: Sensitivity of Te nanoribbons (Ohmic contacts) with different width of 95±12 nm (a) and 57±7 nm (b) on $NO_X$ (g) (inset: SEM images of Te nanoribbons), sensitivity on $NO_X$ (g) of 10 ppm as a function of the width of Te nanoribbons (c) and schematic diagram to describe the variation of resistance depending on material dimension due to the changed conduction channel (d).

Electrical contact types between a nanoribbon and an Au/Cr electrode as a device function should be considered as a possible way to enhance sensor performance. Sensor devices with Schottky contact such as Schottky diode devices have demonstrated improved sensing performances [11, 41], since energy band diagrams of devices with Schottky contacts can be locally changed after the adsorption of gas analytes at the junction region as shown in Figure 4.9. The energy band diagram of the junction between metal and p-type Te semiconductor with a Schottky contact on electron withdrawing $NO_x$ (g) shows that after adsorption of electron withdrawing $NO_x$ (g) at the junction region, the Schottky energy barrier, $\phi$, was reduced to $\phi'$ by $\Delta eV$. Consequently, the modified Schottky energy barrier ($\phi'=\phi-\Delta eV$) can increase sensitivity, because the additionally reduced resistance of devices with the adsorbed analytes will have larger resistance variation ($\Delta R$). $I_{DS}$-$V_{DS}$ characteristics of Te nanoribbons with similar width indicated the existence of pseudo-ohmic and pseudo-Schottky contacts due to the defects between Au/Cr electrodes and Te nanoribons (Figure 4.10 (a)). Sensing properties of single Te

nanoribbon based devices with ohmic electrical contact (Figure 4.10 (b)) and Schottky contact (Figure 4.10 (c)) were analyzed on $NO_x$ (g) of the controlled mass flow. Sensing properties of those devices as a function of $NO_x$ (g) concentration also showed that a sensor device with a Schottky electrical contact demonstrated higher sensitivity over ohmic contact, as illustrated in Figure 4.10 (d).

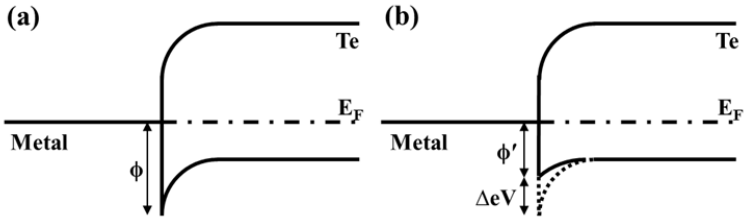


**Figure 4.9**: Energy band diagrams of devices with Schottky contact at the junction region between a metal and a p-type Te semiconducting material: without analytes (a) and after adsorption of electron withdrawing analytes (b).

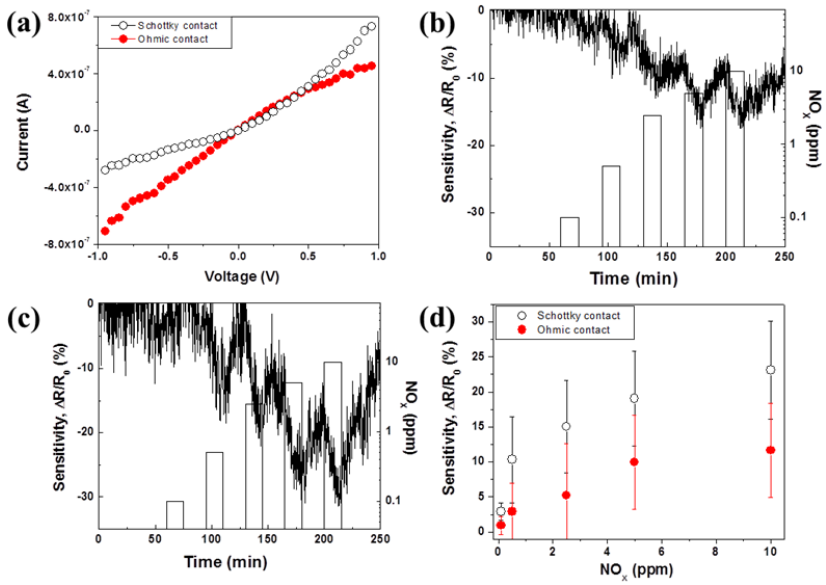


**Figure 4.10**: $I_{DS}$-$V_{DS}$ characteristics with ohmic and Schottky electrical contacts (The width of Te nanoribbons is 95±12 nm and 97±16 nm, respectively.) (a). Sensitivity on 10 ppm $NO_X$ of Te nanoribbon (95 nm width) with ohmic contact (b) and of Te nanoribbon (97 nm width) with Schottky contact (c), and sensitivity of Te nanoribbons as a function of $NO_X$ concentration at different electrical contacts (d).

$I_{DS}$-$V_{DS}$ characteristics of Te nanoribbons with similar width indicated the existence of pseudo-ohmic and pseudo-Schottky contacts due to the defects between Au/Cr electrodes and Te nanoribons (Figure 4.10 (a)). Sensing properties of single Te nanoribbon based devices with ohmic electrical contact (Figure 4.10 (b)) and Schottky contact (Figure 4.10 (c)) were analyzed on $NO_x$ (g) of the controlled mass flow. Sensing properties of those devices as a function of $NO_x$ (g) concentration also showed that a sensor device with a Schottky electrical contact demonstrated higher sensitivity over ohmic contact, as illustrated in Figure 4.10 (d).

A single Te nanoribbon based sensor device with a Schottky electrical contact was annealed at 200$^{o}$C for 1 hour in 5 % $H_2/N_2$ (g) to investigate effects of annealed Te transducers on their sensing properties. The Schottky electrical contact of the device was changed to an ohmic electrical contact as shown in Figure 4.11 (a), since the pseudo-Schottky contact due to defects distributed between an Au/Cr electrode and Te nanoribbon was improved by heat treatment. Temperature dependent electrical properties of the annealed Te nanoribbon were measured at the temperatures ranging from 15K to 300K. Temperature dependent resistivity displayed a typical semiconducting behavior of a Te nanoribbon as shown in Figure 4.11 (b). Thermal activation energy was founded to be 18 meV at near room temperature as seen in the Arrhenius plot. Compared to the thermal activation energy of 87 meV in our previously fabricated Te nanotubes [44], the reduced thermal activation energy may be attributed to the enhanced dopant level due to the increased crystallographic defects. Temperature dependent electrical conductivity of tellurium has been typically determined by mobility variation, not carrier concentration,

which can be associated with hopping transport of carriers. The linear plot of mobility at near room temperature can be described by the characteristic equation of temperature dependent mobility, $\mu = \mu_0 \exp(-E/kT)$, which is governed by crystalline defects within the grains [45, 46]. In this equation, $\mu_0$ is a constant, and E and $k$ are the activation energy and the Boltzmann constant, respectively. The thermal activation of 16 meV at near room temperature was also obtained from the temperature dependent mobility, which can be corresponded to the thermal activation energy of 18 meV from the Arrhenius plot of electrical resistance. Even though the electrical contact type of the sensor device was changed to an ohmic contact, the sensitivity of the single Te nanoribbon based device on $NO_x$ (g) was improved (Figure 4.11 (d)). The enhanced sensitivity of the annealed device can be attributed to the improved crystallinity of a Te nanoribbon. The reduced defects for the annealing process can improve the mobility in the conducting channel as a transducer function, as described in the effects of the reduced dimension of nanoribbons on sensitivity of the sensor devices.

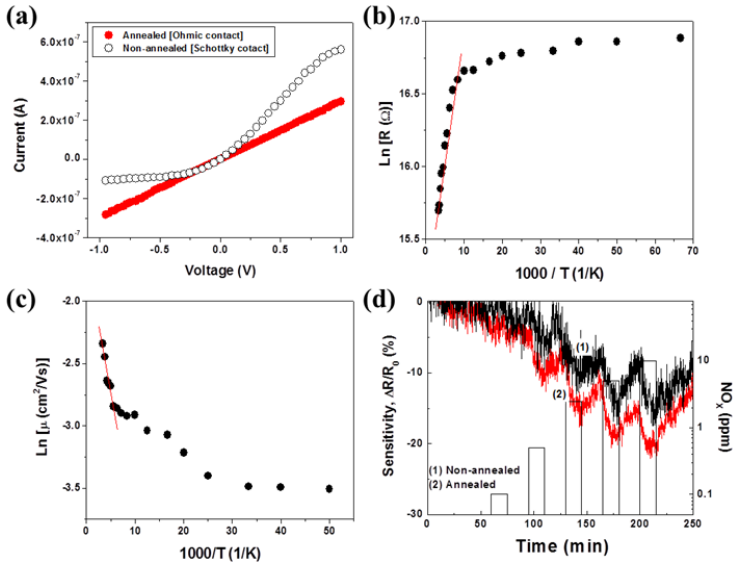

**Figure 4.11:** Annealing effects on electrical and sensing properties of Te nanoribbon with the width of 73 nm: $I_{DS}$-$V_{DS}$ characteristic before and after annealing (a), temperature dependent electrical resistivity (b) and FET mobility (c) of the annealed Te nanoribbon, and its sensitivity to different $NO_x$ (g) concentrations (d) before and after annealing. The annealing was carried out at 200$^{o}$C for 1 hour in 5 % $H_2/N_2$ (g). The linear plot of resistivity at the temperature ranged from 160 K to 300 K depicted the thermal activation energy of 18 meV and 16 meV from Arrhenius equation of electrical resistance and mobility, respectively.

### 4.2.5 Conclusions

In conclusion, single tellurium nanoribbon based nano-devices with well-controlled geometries and dimensions were fabricated by the LPNE technique, which has been expressing a significant potential for the fabrication of various electronic devices. The electrical properties of the fabricated single tellurium nanoribbon based devices showed decreased amount of defects in Te nanoribbons with the reduced dimensions, based on the variation of FET mobility. Among various electronic devices, the sensor performance was demonstrated as a function of the width of Te nanoribbons. The enhanced sensitivity with the decreased width can be attributed to reduction of the conducting channel and the improved conductivity of Te nanoribbon. Furthermore, measurement of sensing properties versus electrical contact types demonstrated that single Te nanoribbon based sensor devices with Schottky contact displayed enhanced sensitivity over the devices with ohmic contact, because of the additionally changed Schottky energy barrier at the junction region after the adsorption of analytes. Temperature dependent electrical properties of an annealed Te nanoribbon show that the conduction due to hopping transport of carriers, since the comparable thermal activation energies of 16 meV and 18 meV were obtained from Arrhenius plot of electrical

resistivity and FET mobility of the annealed Te nanoribbon. Moreover, the linear Arrhenius plot of mobility at near room temperature shows that the electrical conduction was determined by the variation of mobility due to the changed defects. The effects on sensing properties by annealing of Te nanoribbon were investigated by the comparison of sensitivity on $NO_x$ (g) before and after annealing process. Despite the change of contact type from Schottky to ohmic contact, the sensitivity of the annealed Te nanoribbon was enhanced by the improved crystallinity of Te nanoribbons.

### 4.2.6 References


[1] J. Kong, N. R. Franklin, C. Zhou, M. G. Chapline, S. Peng, K. Cho and H. Dai, Nanotube Molecular Wires as Chemical Sensors, *Science,* 2000. **287**: p. 622-625

[2] Y. Cui, Q. Wei, H. Park and C. M. Lieber, Nanowire Nanosensors for Highly Sensitive and Selective Detection of Biological and Chemical Species, *Science,* 2001. **293**: p. 1289-1292

[3] G. Zheng, F. Patolsky, Y. Cui, W. U. Wang and C. M. Lieber, Multiplexed electrical detection of cancer markers with nanowire sensor arrays, *Nat Biotech,* 2005. **23**: p. 1294-1301

[4] Y. Chen, X. Wang, S. Erramilli, P. Mohanty and A. Kalinowski, Silicon-based nanoelectronic field-effect pH sensor with local gate control, *Applied Physics Letters,* 2006. **89**: p. 223512-3

[5] N. Chartuprayoon, C. M. Hangarter, Y. Rheem, H. Jung and N. V. Myung, Wafer-Scale Fabrication of Single Polypyrrole Nanoribbon-Based Ammonia Sensor, *The Journal of Physical Chemistry C,* 2010. **114**: p. 11103-11108

[6] S. C. Hernandez, D. Chaudhuri, W. Chen, N. V. Myung and A. Mulchandani, Single Polypyrrole Nanowire Ammonia Gas Sensor, *Electroanalysis,* 2007. **19**: p. 2125-2130

[7] T. Zhang, M. B. Nix, B.-Y. Yoo, M. A. Deshusses and N. V. Myung, Electrochemically Functionalized Single-Walled Carbon Nanotube Gas Sensor, *Electroanalysis,* 2006. **18**: p. 1153-1158

[8] Z. Ting and et al., Recent progress in carbon nanotube-based gas sensors, *Nanotechnology,* 2008. **19**: p. 332001

[9] I. Heller, A. M. Janssens, J. Mannik, E. D. Minot, S. G. Lemay and C. Dekker, Identifying the Mechanism of Biosensing with Carbon Nanotube Transistors, *Nano Letters,* 2007. **8**: p. 591-595

[10] A. Tricoli, M. Righettoni and A. Teleki, Semiconductor Gas Sensors: Dry Synthesis and Application, *Angewandte Chemie International Edition,* 2010. **49**: p. 7632-7659

[11] M. E. Franke, T. J. Koplin and U. Simon, Metal and Metal Oxide Nanoparticles in Chemiresistors: Does the Nanoscale Matter?, *Small,* 2006. **2**: p. 36-50

[12] E. J. Menke, M. A. Thompson, C. Xiang, L. C. Yang and R. M. Penner, Lithographically patterned nanowire electrodeposition, *Nat Mater,* 2006. **5**: p. 914-919

[13] F. Yang, D. K. Taggart and R. M. Penner, Joule Heating a Palladium Nanowire Sensor for Accelerated Response and Recovery to Hydrogen Gas, *Small,* 2010. **6**: p. 1422-1429

[14] H. Jung, Y. Rheem, N. Chartuprayoon, J.-H. Lim, K.-H. Lee, B. Yoo, K.-J. Lee, Y.-H. Choa, P. Wei, J. Shi and N. V. Myung, Ultra-long bismuth telluride nanoribbons synthesis by lithographically patterned galvanic displacement, *Journal of Materials Chemistry,* 2010. **20**: p. 9982-9987

[15] C. Xiang, S.-C. Kung, D. K. Taggart, F. Yang, M. A. Thompson, A. G. Gu?ell, Y. Yang and R. M. Penner, Lithographically Patterned Nanowire Electrodeposition: A Method for Patterning Electrically Continuous Metal Nanowires on Dielectrics, *ACS Nano,* 2008. **2**: p. 1939-1949

[16] W. Gopel and K. D. Schierbaum, $SnO_2$ sensors: current status and future prospects, *Sensors and Actuators B: Chemical,* 1995. **26**: p. 1-12

[17] J. Santos, P. Serrini, B. O'Beirn and L. Manes, A thin film $SnO_2$ gas sensor selective to ultra-low $NO_2$ concentrations in air, *Sensors and Actuators B: Chemical,* 1997. **43**: p. 154-160

[18] A. Kolmakov, Y. Zhang, G. Cheng and M. Moskovits, Detection of CO and O2 Using Tin Oxide Nanowire Sensors, *Advanced Materials,* 2003. **15**: p. 997-1000

[19] Y. J. Chen, L. Nie, X. Y. Xue, Y. G. Wang and T. H. Wang, Linear ethanol sensing of SnO2 nanorods with extremely high sensitivity, *Applied Physics Letters,* 2006. **88**: p. 083105-3

[20] Y. S. Kim, S.-C. Ha, K. Kim, H. Yang, S.-Y. Choi, Y. T. Kim, J. T. Park, C. H. Lee, J. Choi, J. Paek and K. Lee, Room-temperature semiconductor gas sensor based on nonstoichiometric tungsten oxide nanorod film, *Applied Physics Letters,* 2005. **86**: p. 213105-213105-3

[21] X. Zhidong and et al., Fabrication and structural characterization of porous tungsten oxide nanowires, *Nanotechnology,* 2005. **16**: p. 2647

[22] D. Zhang, Z. Liu, C. Li, T. Tang, X. Liu, S. Han, B. Lei and C. Zhou, Detection of NO2 down to ppb Levels Using Individual and Multiple In2O3 Nanowire Devices, *Nano Letters,* 2004. **4**: p. 1919-1924

[23] Q. Wan, Q. H. Li, Y. J. Chen, T. H. Wang, X. L. He, J. P. Li and C. L. Lin, Fabrication and ethanol sensing characteristics of ZnO nanowire gas sensors, *Applied Physics Letters,* 2004. **84**: p. 3654-3656

[24] J. Li, Y. Lu, Q. Ye, M. Cinke, J. Han and M. Meyyappan, Carbon Nanotube Sensors for Gas and Organic Vapor Detection, *Nano Letters,* 2003. **3**: p. 929-933

[25] P. Qi, O. Vermesh, M. Grecu, A. Javey, Q. Wang, H. Dai, S. Peng and K. J. Cho, Toward Large Arrays of Multiplex Functionalized Carbon Nanotube Sensors for Highly Sensitive and Selective Molecular Detection, *Nano Letters,* 2003. **3**: p. 347-351

[26] O. K. Varghese, P. D. Kichambre, D. Gong, K. G. Ong, E. C. Dickey and C. A. Grimes, Gas sensing characteristics of multi-wall carbon nanotubes, *Sensors and Actuators B: Chemical,* 2001. **81**: p. 32-41

[27] T. Siciliano, E. Filippo, A. Genga, G. Micocci, M. Siciliano and A. Tepore, Single-crystalline Te microtubes: Synthesis and $NO_2$ gas sensor application, *Sensors and Actuators B: Chemical,* 2009. **142**: p. 185-190

[28] S. Sen, M. Sharma, V. Kumar, K. P. Muthe, P. V. Satyam, U. M. Bhatta, M. Roy, N. K. Gaur, S. K. Gupta and J. V. Yakhmi, Chlorine gas sensors using one-dimensional tellurium nanostructures, *Talanta,* 2009. **77**: p. 1567-1572

[29] D. Tsiulyanu, I. Stratan, A. Tsiulyanu, H. D. Liess and I. Eisele, Investigation of the oxygen, nitrogen and water vapour cross-sensitivity to NO2 of tellurium-based thin films, *Sensors and Actuators B: Chemical,* 2007. **121**: p. 406-413

[30] V. Bhandarkar, S. Sen, K. P. Muthe, M. Kaur, M. S. Kumar, S. K. Deshpande, S. K. Gupta, J. V. Yakhmi and V. C. Sahni, Effect of deposition conditions on the microstructure and gas-sensing characteristics of Te thin films, *Materials Science and Engineering: B,* 2006. **131**: p. 156-161

[31] S. Sen, K. P. Muthe, N. Joshi, S. C. Gadkari, S. K. Gupta, Jagannath, M. Roy, S. K. Deshpande and J. V. Yakhmi, Room temperature operating ammonia sensor based on tellurium thin films, *Sensors and Actuators B: Chemical,* 2004. **98**: p. 154-159

[32] D. Tsiulyanu, S. Marian, H. D. Liess and I. Eisele, Effect of annealing and temperature on the NO2 sensing properties of tellurium based films, *Sensors and Actuators B: Chemical,* 2004. **100**: p. 380-386

[33] D. Tsiulyanu, S. Marian, V. Miron and H. D. Liess, High sensitive tellurium based NO2 gas sensor, *Sensors and Actuators B: Chemical,* 2001. **73**: p. 35-39

[34] Z. Wang, L. Wang, J. Huang, H. Wang, L. Pan and X. Wei, Formation of single-crystal tellurium nanowires and nanotubes via hydrothermal recrystallization and their gas sensing properties at room temperature, *Journal of Materials Chemistry,* 2010. **20**: p. 2457-2463

[35] J. Kong, M. G. Chapline and H. Dai, Functionalized Carbon Nanotubes for Molecular Hydrogen Sensors, *Advanced Materials,* 2001. **13**: p. 1384-1386

[36] H. C. Choi, M. Shim, S. Bangsaruntip and H. Dai, Spontaneous Reduction of Metal Ions on the Sidewalls of Carbon Nanotubes, *Journal of the American Chemical Society,* 2002. **124**: p. 9058-9059

[37] A. Kolmakov, D. O. Klenov, Y. Lilach, S. Stemmer and M. Moskovits, Enhanced Gas Sensing by Individual SnO2 Nanowires and Nanobelts Functionalized with Pd Catalyst Particles, *Nano Letters,* 2005. **5**: p. 667-673

[38] L. G. Teoh, Y. M. Hon, J. Shieh, W. H. Lai and M. H. Hon, Sensitivity properties of a novel $NO_2$ gas sensor based on mesoporous $WO_3$ thin film, *Sensors and Actuators B: Chemical,* 2003. **96**: p. 219-225

[39] J. Xu, Q. Pan, Y. a. Shun and Z. Tian, Grain size control and gas sensing properties of ZnO gas sensor, *Sensors and Actuators B: Chemical,* 2000. **66**: p. 277-279

[40] C. Cantalini, H. T. Sun, M. Faccio, M. Pelino, S. Santucci, L. Lozzi and M. Passacantando, $NO_2$ sensitivity of $WO_3$ thin film obtained by high vacuum thermal evaporation, *Sensors and Actuators B: Chemical,* 1996. **31**: p. 81-87

[41] P.-H. Yeh, Z. Li and Z. L. Wang, Schottky-Gated Probe-Free ZnO Nanowire Biosensor, *Advanced Materials,* 2009. **21**: p. 4975-4978

[42] L. King Wai Chiu, X. Ning, C. Fung and C. Hongzhi, Optical response time for carbon nanotube based infrared detectors*, Proc. Nanotechnology, 2009. IEEE-NANO 2009. 9th IEEE Conference on,* 2009.

[43] Y. M. Wong, W. P. Kang, J. L. Davidson, A. Wisitsora-at and K. L. Soh, A novel microelectronic gas sensor utilizing carbon nanotubes for hydrogen gas detection, *Sensors and Actuators B: Chemical,* 2003. **93**: p. 327-332

[44] Y. Rheem, C. H. Chang, C. M. Hangarter, D.-Y. Park, K.-H. Lee, Y.-S. Jeong and N. V. Myung, Synthesis of tellurium nanotubes by galvanic displacement, *Electrochimica Acta,* 2010. **55**: p. 2472-2476

[45] M. J. Capers and M. White, The electrical properties of vacuum deposited tellurium films, *Thin Solid Films,* 1973. **15**: p. 5-14

[46] A. M. Phahle, Electrical properties of thermally evaporated tellurium films, *Thin Solid Films,* 1977. **41**: p. 235-241

## 4.3 Bismuth Tellurde Nanoribbons by Lithographically Patterned Galvanic Displacement Reaction

### 4.3.1 Abstract

We demonstrated the wafer level batch synthesis and fabrication of single semiconducting thermoelectric nanoribbon based devices by Lithographically Patterned Galvanic Displacement (LPGD). The shape, composition, and dimension of nanoribbons were tailored by adjusting deposition conditions. High resolution TEM images with fast Fourier transform (FFT)-converted selected area electron diffraction (SAED) patterns confirmed the formation of polycrystalline $Bi_2Te_3$ intermetallic compound with a rhombohedral structure. The precipitated elemental Te and Bi due to the supersaturation of $Bi_xTe_y$ alloy with high content Te were not observed in the analysis. The size dependent electrical resistivity of $Bi_xTe_y$ nanoribbons with different thickness shows a classic size effect because of the increase of surface boundary scattering. The as-synthesized nanoribbons were n-type semiconductors with no clear trend between field effect carrier mobility and composition, which might be attributed to the trapped charges at the interface between the channel and dielectric layer. The preliminary results on some theremoelectric properties (i.e. Seebeck coefficient and power factor) show that the Seebeck coefficient of as-synthesized 0.1 μm thick $Bi_{30}Te_{70}$ nanoribbon are comparable with bulk counterparts, however the power factor were much lower because of poor crystallinity which leads to higher resistivity.

### 4.3.2 Introduction

One dimensional nanostructures are extremely attractive for many applications including electronics, optoelectronics, data storages, sensors, and thermoelectrics, because they can function as both devices and the wires that access them [1-10]. While many reports have demonstrated the power of nanoengineered materials as high performance low-density devices, the fabrication methods employed are seriously limited in terms of high-density complex nanodevices. 1 dimensional nanostructures are usually synthesized using either the "top-down" or the "bottom-up" approaches. "Top-down" approaches usually utilize planar lithographic techniques to transfer pre-designed patterns to a substrate, which can form complex high density microstructures in well-defined positions on substrates. However, achieving dimension much less than readily available optical wavelengths often requires slow, expensive, serial processes such as electron-beam, focus ion beam, and scanning-probe lithography[11, 12]. "Bottom-up" approaches can mitigate this difficulty by confining the dimension of nanostructures within a scaffold/template [13]. However, bottom-up approaches are limited in the types of templates, and thus wire geometries, that may be produced. In addition, "bottom-up" template synthesized nanowires need post positioning and assembling to create devices.

The success of nanodevices depends on new nanofabrication methods which can massively synthesize nanostructures in a cost-effective manner and reproducible position nanostructures between closely-spaced microelectrodes. Lithographically Patterned Nanowire Electrodeposition (LPNE) which was reported by Penner *et al* [14, 15]. overcomes the obstacles by combining the advantages of "top-down" photolithography

and “bottom-up” electrodeposition to synthesize complex high density nanowires to pre-determined locations. They demonstrated the concept by synthesizing noble metallic (e.g. Au, Pd, and Pt) and semiconducting PbTe nanowires on comparatively large areas (> 1 $cm^2$), which show a high level of dimensional uniformity.

Galvanic displacement reaction is an electrochemical process induced by the difference in electronegativity (i.e. redox potential) between materials. Unlike electrodeposition, galvanic displacement does not require electrodes to connect with an external power supply. Thus, more complex shaped nanostructures can be synthesized.

Thermoelectric (TE) energy converters are solid-state devices that can generate electricity by harvesting waste thermal energy, thereby improving the efficiency of a system. The many advantages of TE devices include solid-state operation, zero-emissions, vast scalability, no maintenance and a long operating lifetime. Nonetheless, due to their limited energy conversion efficiencies, thermoelectric devices currently have a rather limited set of applications. However, there is a reinvigorated interest in the field of thermoelectrics by identifying classical and quantum mechanical size effects, which provide additional ways to enhance energy conversion efficiencies in nanostructured materials including one-dimensional nanostructures, which are predict to exceed a ZT of 5 [16-18].

### 4.3.3 Experimental

Highly doped Si (p-type) wafers with atomic layer epitaxially grown $SiO_2$ (0.3 μm) were used as substrates (Figure 4.12 (a)). Nickel and the photoresist layer (S1813 from

Rohm and HAAS Electronic Materials, Inc.) were e-beam evaporated and spin-coated, respectively, followed by patterning the photoresist using standard photolithography technique (Figure 4.12 (b-c)). Two different thicknesses (0.025 μm and 0.1 μm) of nickel layers were utilized to demonstrate control over the thickness of the nanoribbons. To ensure the complete removal of the exposed Ni films with smooth undercut profiles, a two step etching process was adopted with chemically etching by a commercial Ni etchant [Type TFB, Transene company Inc.] prior to electrochemically etching to ensure complete removal of the exposed Ni film and produce smooth undercut profiles. The electrochemical etching electrolyte was composed of KCl (0.1 M) and HCl (0.024 M). Although the chemical etch step did impose a slight recess on the Ni nanoband, the trench formation was very uneven and relatively insensitive to time, with nm to < 1 μm undercuts after 5 minutes. The first step was necessary to prevent island formation due to the large open areas typical of our custom patterns. While the islands were not completely detrimental to our process they were subject to non-preferential $Bi_xTe_y$ deposition due to the nature of galvanic deposition and were therefore deemed undesirable. The formation of various trench depths was achieved by controlling the electrochemical etching duration, with a nearly constant etch rate displayed for both 0.025 and 0.1 μm thick sacrificial layers for all time periods < 10 min. $Bi_xTe_y$ nanoribbons were synthesized by galvanically displacing the exposed nickel (Figure 4.12 (e)) at room temperature. The displacement time was adjusted to control the width of the nanoribbons. After synthesis of the nanoribbons, the photoresist and nickel were selectively etched using acetone and 2% (v/v) nitric acid, respectively (Figure 4.12 (g)).

Gold/chromium micro electrodes were subsequently fabricated on top of the nanoribbons using a lift-off technique to investigate composition and temperature dependent electron transport properties (Figure 4.12 (h)).

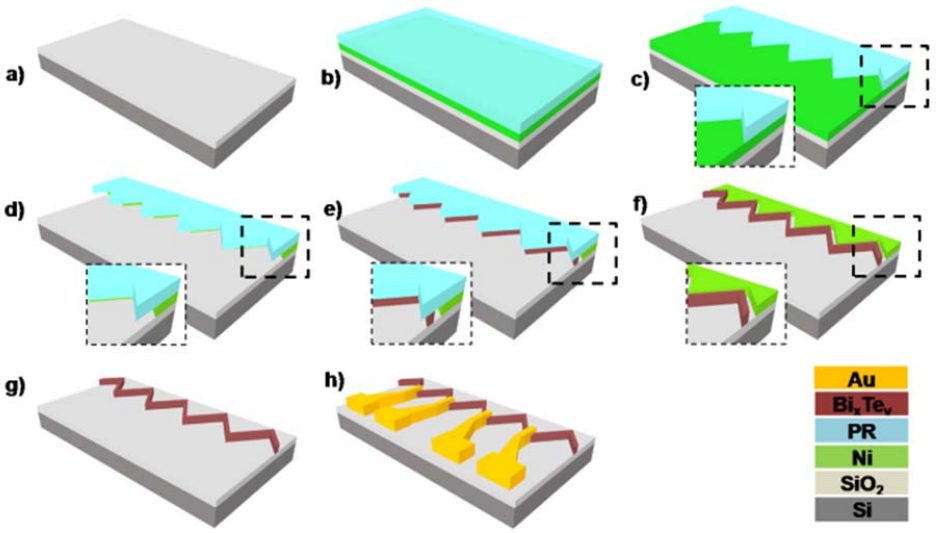


**Figure 4.12:** Schematic illustrations of $Bi_xTe_y$ nanoribbon synthesis by Lithographic Patterned Galvanic Displacement (LPGD); $SiO_2$ layer ($t_{ox}$ =0.3 µm) was deposited by atomic layer epitaxy followed by the photolithographic patterning of align marks (a). The sacrificial layer was e-beam evaporated on substrate followed by spin-coating of PR (b), PR was developed (c). The sacrificial layer was chemically or electrochemically etched to create the undercut trench (d). The nanoribbons were glavanically displaced using the vertical exposed layer as an electrode (e), followed by removal of PR and (f) and the sacrificial layer (g). Cr and Au were e-beam deposited by the photolithographic patterning to form electrical contacts (h).

For TEM analysis, focused ion beam (FIB) (NOVA 600 Nanolab, FEI) milling technique was utilized for dice small sections the samples, followed by platinum deposition onto FIB-milled specimen in order to shield it from high energy associated with ion beam in Figure 4.13 (a). The cross-sectional images of the FIB-milled $Bi_xTe_y$ nanoribbons show the variation of nanoribbon thickness depending on the locations

which might be attributed to reduced of trench gap due to bowing of photoresist (Figure 4.13 (c,d)). Additionally, for the measurement of Seebeck coefficients, e-beam lithographical patterning technique was utilized to create gold microheater and electrical contacts to as-synthesized 0.1 μm thick $Bi_{30}Te_{70}$ nanoribbons (Figure 4.23 (a)).

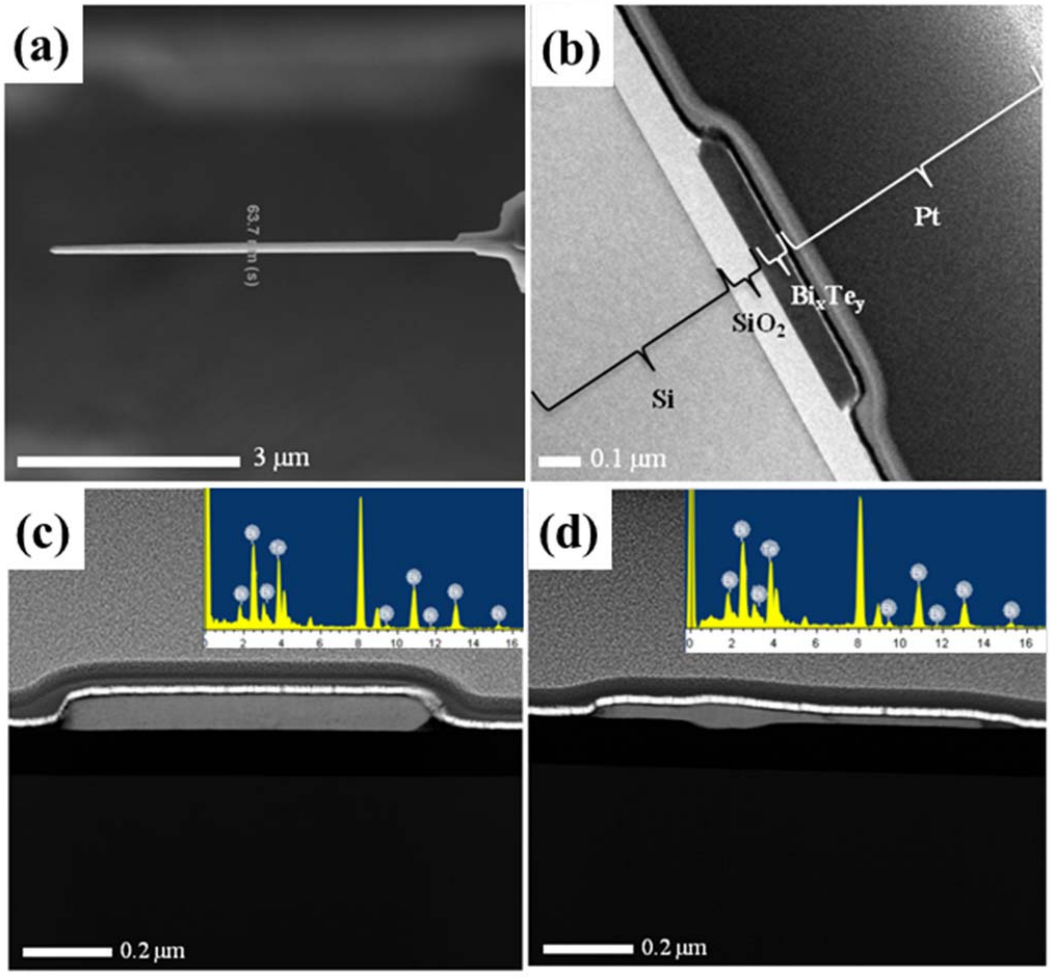


**Figure 4.13**: SEM images of FIB-milled specimens; $Bi_xTe_y$ nanoribbons were protected from an ion beam by Pt deposition (a, b). The cross-sectional images of approx. 0.1 μm (c) and 0.025 μm (b) $Bi_xTe_y$ nanoribbons. The thickness of 0.1 μm thick nanoribbon was more uniform (0.079 to 0.084 μm) compared to 0.025 μm thick nanoribbon (0.021 to 0.047 μm). Inset illustrates EDS analysis of each sample.

### 4.3.4 Results and Discussion

Figure 4.12 illustrates the detailed experimental procedure. The nickel sacrificial layers deposited on a silicon substrate were utilized to demonstrate control over the thickness of the nanoribbons. Lithographical patterned nickel layer was etched to impose a slight recess on the nickel nanoband. The exposed nickel in the trench is galvanically displaced by bismuth and tellurium ions in electrolytes, where the width of the nanoribbons depends on the displacement time. The electrolytes with different concentration of $HTeO_2^+$ and $Bi^{3+}$ were used to investigate the effect of solution composition on nanoribbon content [19-21]. The difference in the redox potentials (i.e. $Ni^{2+}/Ni^0$ ($E^O$ = -0.257 V vs. SHE) is more cathodic than $Bi^{3+}/Bi^0$ ($E^O$ = 0.308 V vs. SHE), and $HTeO_2^+/Te^0$ ($E^O$ = 0.551 V vs. NHE)) [22, 23]. Since the Gibbs free energy of $Bi_2Te_3$ formation is negative (i.e. $\Delta G_f^0$= - 899.088 $kJmol^{-1}$), the direct deposition of $Bi_2Te_3$ compound is thermodynamically more favorable over the codeposition of $Bi^0$ and $Te^0$ metals [24], which leads to the following reaction (Equation 4. 5).

$$2Bi^{3+}(aq) + 3HTeO_2^+(aq) + 9Ni^0(s) + 9H^+(aq) \rightarrow Bi_2Te_3(s) + 9Ni_2^+(aq) + 6H_2O(l) \quad \text{Equation 4.5}$$

Figure 4.14 shows the complex shapes of the as-synthesized $Bi_xTe_y$ nanoribbons (i.e. 0.1 μm thickness by 3 to 15.3 mm long). The geometrical layout and length of $Bi_xTe_y$ nanowires were predetermined by the photolithographic mask. The thickness of $Bi_xTe_y$ nanoribbons was dependent on the thickness of sacrificial nickel layer. The width

of synthesized $Bi_xTe_y$ nanowires was monotonically increased with galvanic displacement reaction time at a fixed trenched depth (Figure 4.15).

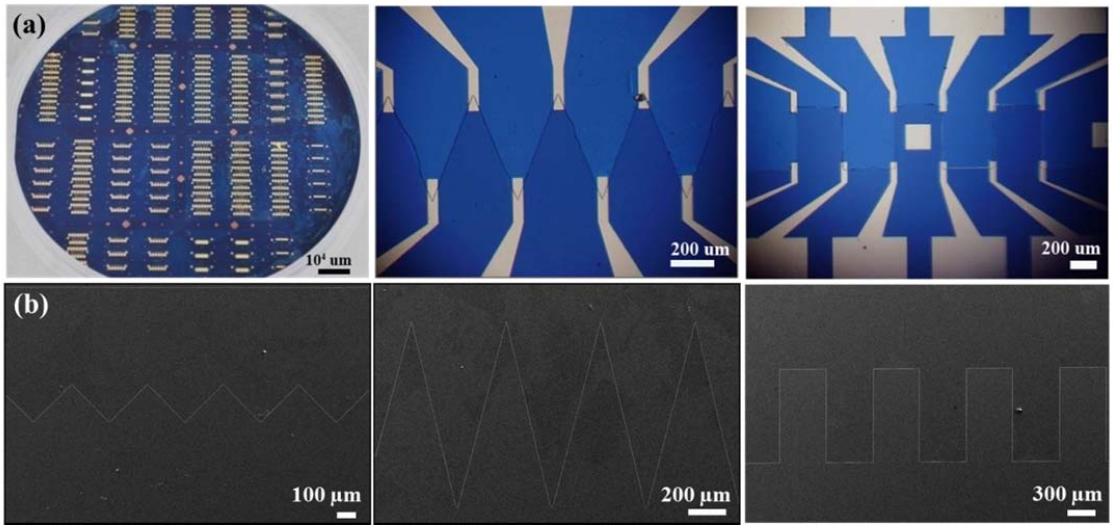


**Figure 4.14:** Images of LPGA synthesized $Bi_xTe_y$ nanoribbons in wafer-scale with different shapes: optical images (a) and SEM images (b).

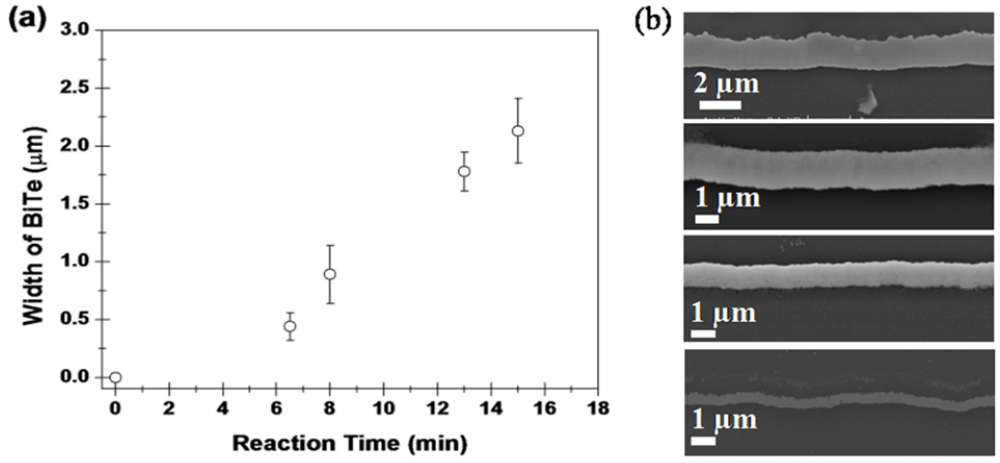


**Figure 4.15:** Width of $Bi_xTe_y$ as a function of the deposition time (a) and SEM images of $Bi_xTe_y$ nanoribbons with different width (b). The electrolyte consisted of 4 mM $Bi^{3+}$ and 10 mM $HTeO^+$ in 1 M $HNO_3$ at room temperature. The thickness of nickel was fixed at 0.1 µm. The trench depths were 13.6 ± 0.4 µm.

The effects of trench dimensions (i.e. trench depth (up to 22 μm) and height (0.025 and 0.1 μm)) on the nanoribbon composition and deposition rate are shown in Figure 4.16, where the nanoribbon compositions were measured using energy dispersive x-ray spectroscopy (EDS). As expected, the composition and deposition rate were strongly dependent on the trench depth with the deposited Te content increasing and the deposition rate decreasing with increasing trench depth. Low deposition rates at greater trench depths might be attributed to slower diffusion rates of the metal ions within the trench. The nanoribbon composition was also dependent on the trench height resulting in a higher deposited Te content for the 0.025 μm thick trench than the 0.1 μm thick trench at a given trench depth. Higher Te content for deeper trenches with shorter height might be attributed to a faster deposition rate of Te(s) (Equation 4.6) compared to UPD deposition of Bi to form $Bi_2Te_3$ (Equation 4.7).

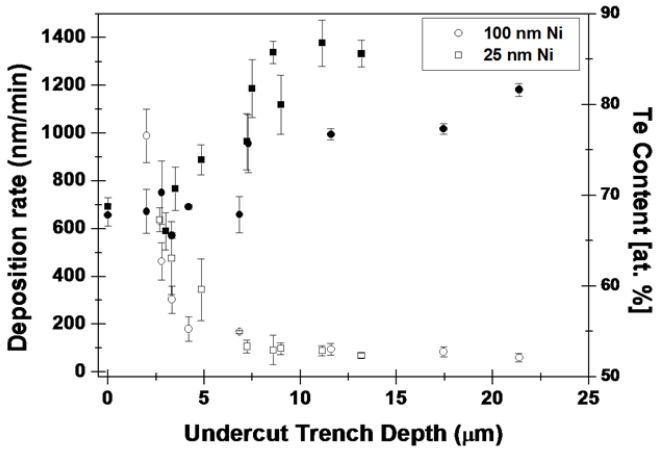


**Figure 4.16:** The composition of $Bi_xTe_y$ nanoribbons (A) and deposition rate (B) as a function of the trench depth. Squares and circles and represent 25 and 100 nm thick nickel layer respectively. The electrolyte consisted of 4 mM $Bi^{3+}$ and 10 mM $HTeO^+$ in 1 M $HNO_3$ at room temperature.

$$HTeO_2^+(aq) + 3H^+(aq) + 4e^- \rightarrow Te(s) + 2H_2O \quad E^o = +0.551V \; vs. \; NHE \qquad \text{Equation 4.6}$$

$$3Te(s) + 2Bi^{3+}(aq) + 6e^- \rightarrow Bi_2Te_3(s) \qquad \text{Equation 4.7}$$

The effect of solution composition on the nanoribbons composition was investigated by varying $Bi^{3+}$ concentration from 2 to 20 mM at fixed concentration of $HTeO^+$ at 10 mM and trench depths of 5 and 9 μm (Figure 4.17). Increasing the $Bi^{3+}$ concentration enhanced the UPD deposition of $Bi^{3+}$ on Te to form $Bi_2Te_3$ compounds (Equation 4.7), which resulted in decreased Te content in the deposit. In addition, the deposition rate increased with increasing $Bi^{3+}$ concentration. These findings indicate that the dimension, composition, and deposition rate of $Bi_xTe_y$ nanoribbons can be readily controlled by adjusting the deposition conditions.

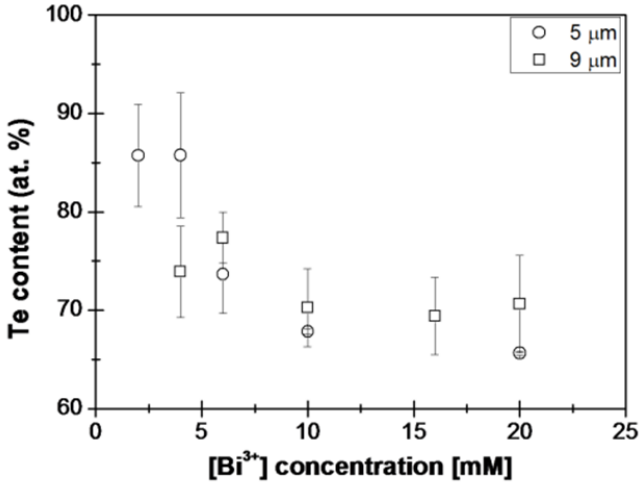


**Figure 4.17**: Effect of the solution composition of deposited Te content. The $Bi^{+3}$ concentration was varied from 2 mM to 20 mM while fixing the $HTeO^+$ concentration at 10 mM. The trench depth was varied from 5 to 9 μm. The thickness of nickel layer was fixed at 0.025 μm.

To confirm the formation of $Bi_2Te_3$ intermetallic compound without the formation of metallic Bi and Te elements, HR-TEM analysis with FFE-converted SAED patterns were performed. Prior to TEM analysis, approx. 0.025 μm thick $Bi_{31}Te_{69}$ and 0.1 μm thick $Bi_{29}Te_{71}$ nanoribbons were annealed at $200^{O}C$ for 8 hours in 5 % $H_2/N_2$ environments to improve the crystallinity and reduce the defect sites. Focused ion beam (FIB) (NOVA 600 Nanolab, FEI) milling technique was utilized to dice small sections of the sample, followed by platinum deposition onto FIB-milled specimens in order to shield it from high energy associated with ion beam in Figure 4.13 (a). The cross-sectional images of the FIB-milled $Bi_xTe_y$ nanoribbons show the variation of nanoribbon thickness depending on the locations which might be attributed to a reduced trench gap due to bowing of the photoresist (Figure 4.13 (c,d)). Figure 4.18 shows the high resolution TEM images with FFT-converted SAED patterns. Similar to the X-ray diffraction patterns of galvanically displaced $Bi_XTe_{1-X}$ thin films from the sacrificial nickel thin films [25], FFT-converted SAED patterns confirmed the formation of polycrystalline $Bi_2Te_3$ intermetallic compounds with a rhombohedral structure. The diffraction patterns from the elemental Te or Bi peaks due to the precipitation of excess elements were not observed (Figure 4.18), which is corresponding with the previous XRD analysis of galvanic displaced $Bi_xTe_y$ thin films.[25] The XRD analysis described that elemental Te was precipitated in $Bi_xTe_y$ thin films with more than ~80 at. % Te contents. The lattice parameters of polycrystalline $Bi_xTe_y$ nanoribbons differed by the converted location where the average lattice parameters of 0.1 μm thick $Bi_{31}Te_{69}$ nanoribbon were a = 4.377 (± 0.22) Å and c = 30.59 (± 0.39) Å and the average lattice parameters of 0.025

μm thick $Bi_{29}Te_{71}$ nanoribbon were a = 4.360 (± 0.29) Å and c = 30.70 (± 0.47) Å). Compared to bulk $Bi_2Te_3$ (a = 4.359 Å and c = 30.44 Å), they show a larger c-axis lattice parameter [26-28]. Since Te atoms are larger than the interstitial sites (i.e. octahedral or tetragonal site) of $Bi_2Te_3$ compound and have high solubility [29-31], it is expected that the excess Te atoms will occupy Bi lattice sites in $Bi_2Te_3$ crystal structure which will alter the lattice parameters and will act as a n-type dopants.

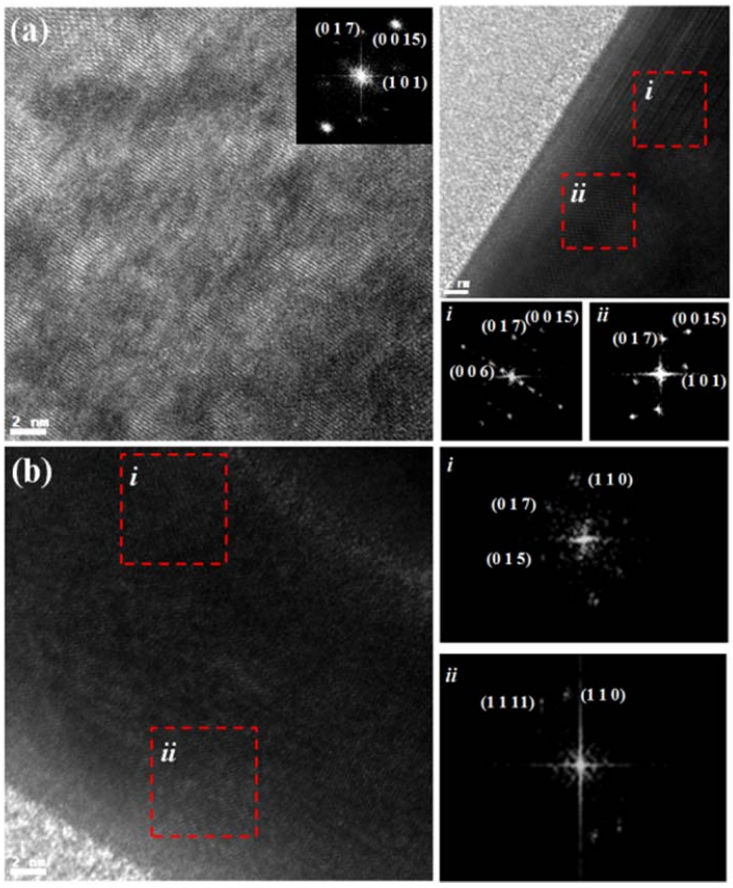


**Figure 4.18**: High resolution TEM images and FFT-converted SAED patterns: $Bi_{31}Te_{69}$ nanoribbon with the cross-sectional area of 0.1 μm thickness/0.77 μm width (a) and $Bi_{29}Te_{71}$ nanoribbon with the cross-sectional area of 0.025 μm thickness/0.89 μm width (b) annealed at $200^{O}C$ for 8 hr in 5 % $H_2/N_2$ environment.

The electrical resistivity of single $Bi_xTe_y$ nanoribbons was measured using a 4-point probe contact method to eliminate the contact resistance (Table 4.2). Other results of bulk/nanowire and the synthesized nanoribbon cannot be directly compared because of the different crystallinity. The resistivity of polycrystal $Bi_xTe_y$ nanoribbons for similar compositions was higher than that of its single crystal bulk/nanowire counterparts because of the increase of defect scattering. Therefore, the electrical resistivities of as-synthesized $Bi_xTe_y$ nanoribbons were one or two orders magnitude greater than bulk counterparts, which cause the lower power factor of $Bi_xTe_y$ nanoribbons than that of bulk. However, the classical size effects of electrical properties were obviously described by the comparison of polycrystal $Bi_xTe_y$ nanoribbons with different thickness: 0.1 μm thick and 0.025 μm thick $Bi_xTe_y$ nanoribbons with 0.7 to 1 μm width (Figure 4.19). 0.025 μm thick $Bi_xTe_y$ nanoribbons have higher resistivity than those of 0.1 μm thick due to the increased surface boundary scattering. Additionally, we investigated the composition dependent electrical resistivity of $Bi_xTe_y$ nanoribbons and compared them with bulk counterparts. Two distinct trends were observed where the electrical resistivity slightly decreased with increased Te content at the composition of 62 to 72 at.% Te. When the deposited Te content is greater than 72 at.%, the electrical resistivity increased with increased Te content. $Bi_xTe_y$ has a rhombohedral crystal structure that belongs to the space group $D^5_{3d}(R\bar{3}m)$ having a unit cell with lattice constants a=4.38 Å, c=30.45 Å in a hexagonal representation. Excess Te in semiconducting $Bi_xTe_y$ nanoribbons acts as a n-type dopant as well as defect for charge carrier scattering because the excess Te occupies Bi lattice sites in the crystal structure [27]. At Te content from 62 to 72 at.%, excess Te

may increase carrier concentration which resulted in decrease in electrical resistivity. When the composition of $Bi_xTe_y$ nanoribbons deviated greatly from the stoichiometric $Bi_2Te_3$ compound, crystalline defects and a rough, porous microstructure may play a more critical role than dopant level. As shown in AFM images (Figure 4.20), $Bi_xTe_y$ nanoribbons with higher Te contents (77.83 at.% Te) show a more rough, porous morphology compared to nearly stoichiometric $Bi_XTe_y$ nanoribbons (67.8 at.% of Te). Nearly stoichiometric $Bi_xTe_y$ nanowire (63.7 at.% Te) showed that the arithmetic average of absolute roughness ($R_a$) was $2.5x10^{-3}$ μm. In contrast, the $Bi_xTe_y$ nanoribbons with higher Te content (82.0 at.% Te) had greater $R_a$ of $5.5x10^{-3}$ μm (Figure 4.20).

Table 4.2: Comparison of electrical resistivity (ρ), Seebeck coefficient (S), and power factor between nanoribbon, nanowire, and bulk counterpart

| Stucture | Composition | Temp. [K] | Resistivity [$10^{-6}$ Ωm] | S [$\mu VK^{-1}$] | Power Factor [$\mu Wm^{-1}K^{-2}$] |
|---|---|---|---|---|---|
| Bulk [30] | $Bi_{29.5}Te_{70.5}$ | 300 | 2.6 | -115 | $5x10^3$ |
| Nanowire [31] | Te-rich BiTe | 300 | 14.2 | -30 | 63 |
| Nanowire [32] | Bi-rich Single crystalline $Bi_{74}Te_{26}$ | 300 | 4.6 | -52 | 581 |
| This work [LPGD] | $Bi_{31}Te_{69}$ | 270 | 289 | -180 | 110 |

LPGD-synthesized $Bi_{31}Te_{69}$ nanoribbon with the cross-sectional area of 0.1x0.77 $\mu m^2$

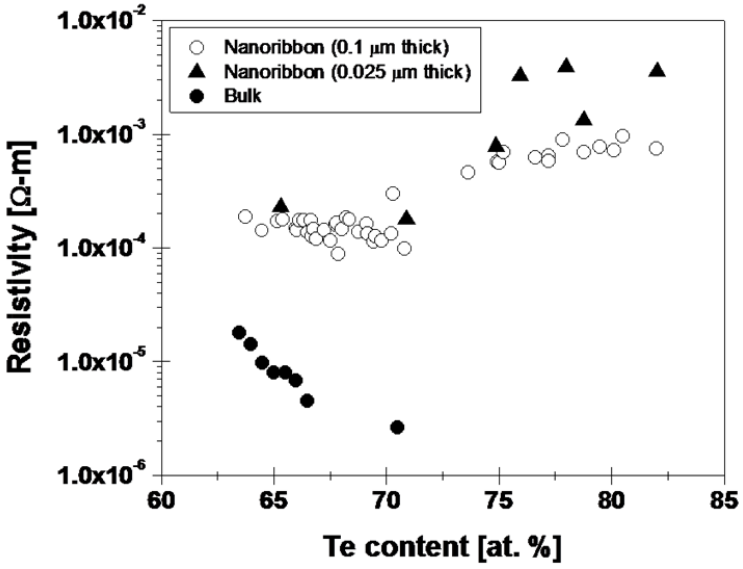


**Figure 4.19**: Effect of the composition on the resistivity of the $Bi_xTe_y$ nanoribbons: ρ vs. Te contents curve.

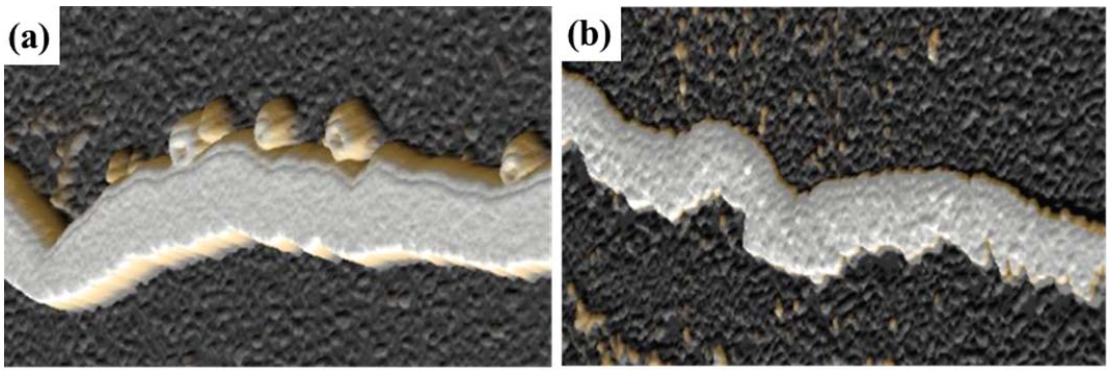


**Figure 4.20**: AFM images of nanoribbons with different compositions: 36 at. % Bi and 64 at. % Te (a), 18 at. % Bi and 82 at. % Te (b) nanoribbons.

Field effect transistor (FET) properties, such as the field effect carrier mobility, were measured to investigate the electronic transport of single $Bi_xTe_y$ nanoribbons. The inset of Figure 4.21 (a) shows the FET schematic diagram. Figure S.4a shows typical transfer characteristics ($I_{ds}$-$V_{gs}$) of a $Bi_xTe_y$ nanowire (69.5 at.% of Te) at $V_{ds}$ = +1 V with

the width of 0.89 μm and length of 385 μm. $I_{ds}$ versus $V_{gs}$ curve displayed n-type semiconductor behavior. According to previous studies of bulk $Bi_xTe_y$ materials, these n-type characteristics could arise from the presence of Bi vacancies [33]. The field-effect carrier mobilities of $Bi_xTe_y$ nanowires ranged from 10-60 $cm^2/Vs$ independent of composition, which might be attributed to the trapped charges at the interface between a channel and dielectric layer (Figure 4.21 (b)) [30].

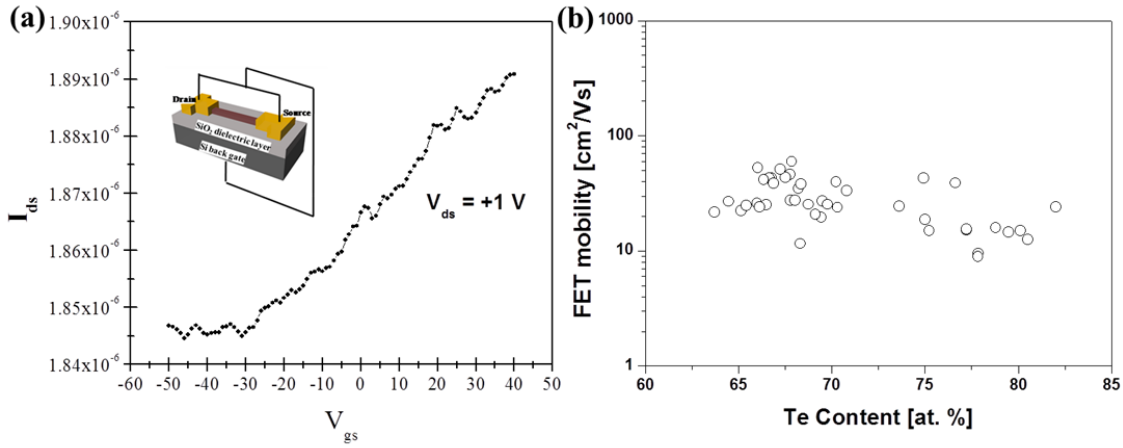


**Figure 4.21**: Back gated $Bi_xTe_y$ nanoribbons FET with 0.3 μm thick $SiO_2$ as the dielectric layer: (a) a typical $I_{ds}$ vs. $V_{gs}$ characteristic at $V_{ds}$ = +1 V and (b) FET mobility as a function of Te content at room temperature.

The temperature dependent electrical resistivity of as-deposited and annealed $Bi_xTe_y$ nanoribbons was investigated from 400 to 25 K (S.5). The annealing was performed in a reducing environment (5% $H_2$ + 95 %$N_2$) at 473 K with an annealing time from 2 to 8 hours (Figure 4.22). The resistivity of n-type $Bi_xTe_y$ decreased at high temperature due to a drastic increase in carrier concentration compared to the slow decrease of mobility with rising temperature. The annealing effects of $Bi_xTe_y$ on

resistivity showed that the carrier density decreased with increasing annealing time corresponding to that of a $Bi_xTe_y$ thin film [21, 34]. The thermal activation energies of the synthesized $Bi_xTe_y$ nanoribbon before and after the annealing were calculated from the temperature dependence of resistivity. The activation energies for the $Bi_xTe_y$ nanowire before and after the annealing process were 9.42 meV and 13.4 meV, respectively, which might be attributed to decreases in the defect level of $Bi_xTe_y$ nanoribbons due to the improvement in crystallinity.

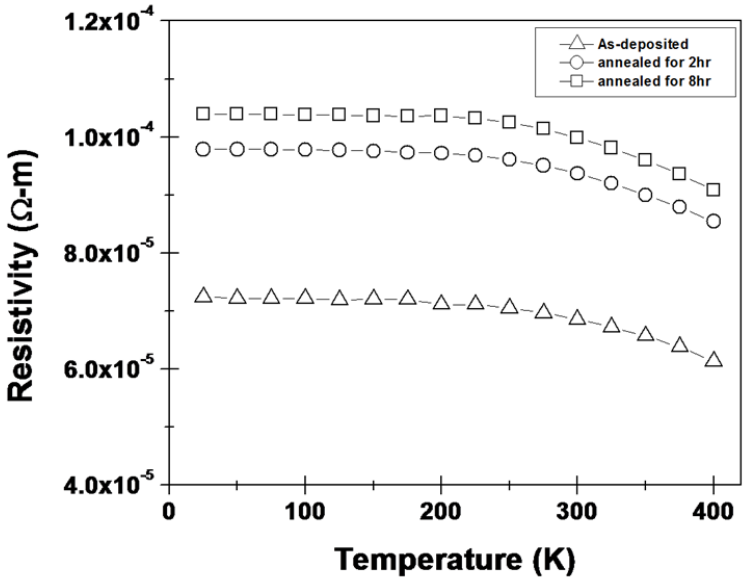


**Figure 4.22**: Temperature dependence of the resistivity of the annealed $Bi_xTe_y$ nanoribbons. The nanoribbons were annealed at 200 $^oC$ in 5% $H_2$ (g) /$N_2$ (g) for zero, 2 and 8 hour.

To determine some thermoelectric properties including electrical resistivity and Seebeck coefficient, e-beam lithographical patterning was utilized to create gold microheater and electrical contacts to as-synthesized 0.1 μm thick $Bi_{30}Te_{70}$ nanoribbons

(Figure 4.23 (a)). Temperature gradient within the specimens was created by introducing electrical pulses on the microheaters. Figure 4.23 (b-d) shows the temperature dependent electrical resistivity, Seebeck coefficient, and power factor, respectively. Compared to its bulk counterpart, the Seebeck coefficient of the nanoribbon was slightly higher (Table 4.2). However, the power factor was one order of magnitude lower than bulks and comparable with reported nanowires data [31, 32, 35]. By annealing the nanoribbons, we anticipate that the thermoelectric properties can be further improved similar to thin films [21].

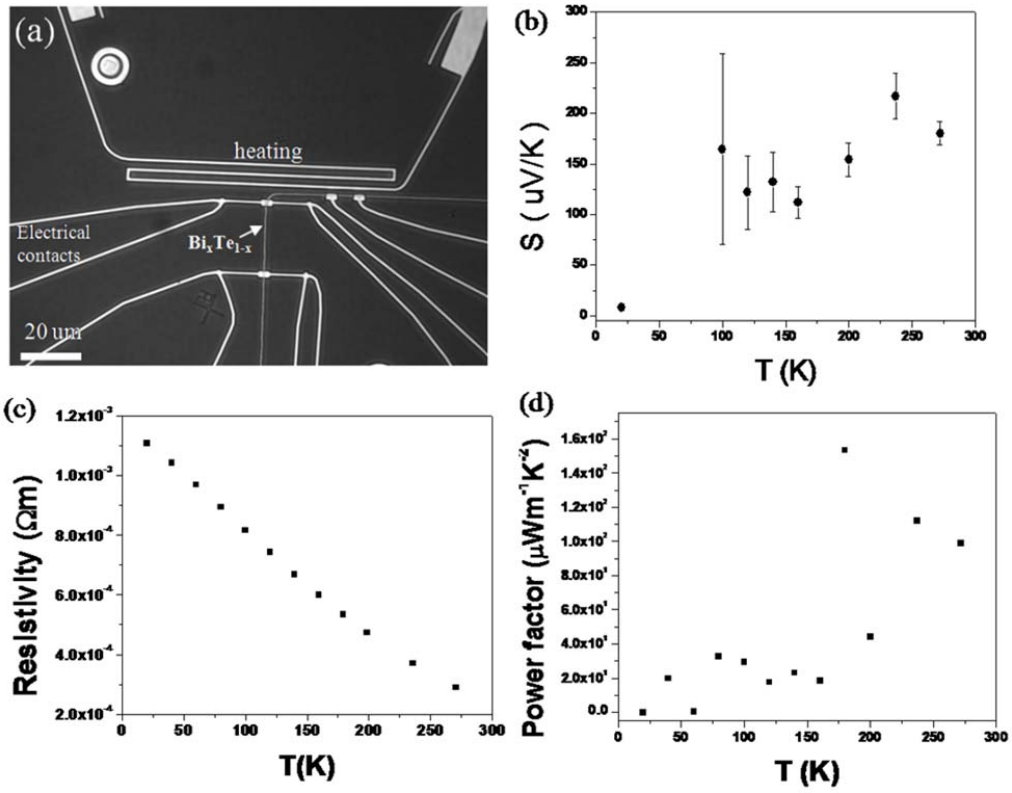


**Figure 4.23**: SEM image of electrically connected $Bi_{31}Te_{69}$ nanoribbon (cross-sectional area of 0.1 x 0.77 $\mu m^2$) (a) and temperature dependent Seebeck coefficient (b), electrical resistivity (c), and power factor (d).

### 4.3.5 Conclusions

The wafer level batch synthesis and fabrication of single semiconducting nanoribbon based devices were demonstrated. The shape, dimension, and composition of nanoribbons were controlled by adjusting the electrolyte composition, deposition conditions, and thickness of the sacrificial layer. Composition dependent electrical resistivity show two distinct regions, where $Bi_xTe_y$ nanoribbons with Te content between 62 and 72 at.% show increased electrical resistivity with increase in Te content and where excess Te may increase carrier concentration to reduce electrical resistivity. When the composition of $Bi_xTe_y$ nanoribbons deviated greatly from the stoichiometric $Bi_2Te_3$ compound ( >72 at.%) crystalline defects and a porous microstructure play a more critical role than dopant level, which resulted in increased electrical resistivity with increase in Te content. The as-synthesized $Bi_xTe_y$ nanoribbons were n-type semiconductors. There were no clear trend between the field effect carrier mobilities and composition and dimensions which might be attributed to the trapped charges at interface between a channel and dielectric layer.

LPGD is a precise, reliable, and IC-compatible method to fabricate nanoscale electronic devices because it allows batch synthesis of high density complex shaped nanostructures with controlled dimensions and composition to predetermined location in a cost effective manner.

### 4.3.6 References


[1] Y. Cui and C. M. Lieber, Functional Nanoscale Electronic Devices Assembled Using Silicon Nanowire Building Blocks, *Science,* 2001. **291**: p. 851-853

[2] Y. Cui, Q. Wei, H. Park and C. M. Lieber, Nanowire Nanosensors for Highly Sensitive and Selective Detection of Biological and Chemical Species, *Science,* 2001. **293**: p. 1289-1292

[3] M. S. Gudiksen, L. J. Lauhon, J. Wang, D. C. Smith and C. M. Lieber, Growth of nanowire superlattice structures for nanoscale photonics and electronics, *Nature,* 2002. **415**: p. 617-620

[4] J.-i. Hahm and C. M. Lieber, Direct Ultrasensitive Electrical Detection of DNA and DNA Sequence Variations Using Nanowire Nanosensors, *Nano Letters,* 2004. **4**: p. 51-54

[5] Y. Huang, X. Duan, Y. Cui, L. J. Lauhon, K.-H. Kim and C. M. Lieber, Logic Gates and Computation from Assembled Nanowire Building Blocks, *Science,* 2001. **294**: p. 1313-1317

[6] M. H. R. Lankhorst, B. W. S. M. M. Ketelaars and R. A. M. Wolters, Low-cost and nanoscale non-volatile memory concept for future silicon chips, *Nat Mater,* 2005. **4**: p. 347-352

[7] L. J. Lauhon, M. S. Gudiksen, D. Wang and C. M. Lieber, Epitaxial core-shell and core-multishell nanowire heterostructures, *Nature,* 2002. **420**: p. 57-61

[8] B. Y. Yoo, F. Xiao, K. N. Bozhilov, J. Herman, M. A. Ryan and N. V. Myung, Electrodeposition of Thermoelectric Superlattice Nanowires, *Advanced Materials,* 2007. **19**: p. 296-299

[9] D. Yu, S. Brittman, J. S. Lee, A. L. Falk and H. Park, Minimum Voltage for Threshold Switching in Nanoscale Phase-Change Memory, *Nano Letters,* 2008. **8**: p. 3429-3433

[10] T. Zhang, S. Mubeen, N. V. Myung and M. A. Deshusses, Recent progress in carbon nanotube-based gas sensors, *Nanotechnology,* 2008. **19**: p. 332001

[11] S. Donthu, Z. Pan, B. Myers, G. Shekhawat, N. Wu and V. Dravid, Facile Scheme for Fabricating Solid-State Nanostructures Using E-Beam Lithography and Solution Precursors, *Nano Letters,* 2005. **5**: p. 1710-1715

[12] K. Salaita, Y. Wang and C. A. Mirkin, Applications of dip-pen nanolithography, *Nat Nano,* 2007. **2**: p. 145-155

[13] D. Natelson, Nanofabrication: Best of both worlds, *Nat Mater,* 2006. **5**: p. 853-854

[14] E. J. Menke, M. A. Thompson, C. Xiang, L. C. Yang and R. M. Penner, Lithographically patterned nanowire electrodeposition, *Nat Mater,* 2006. **5**: p. 914-919

[15] Y. Yang, S. C. Kung, D. K. Taggart, C. Xiang, F. Yang, M. A. Brown, A. G. G. ell, T. J. Kruse, J. C. Hemminger and R. M. Penner, Synthesis of PbTe Nanowire Arrays using Lithographically Patterned Nanowire Electrodeposition, *Nano Letters,* 2008. **8**: p. 2447-2451

[16] E. J. Menke, M. A. Brown, Q. Li, J. C. Hemminger and R. M. Penner, Bismuth Telluride ($Bi_2Te_3$) Nanowires: Synthesis by Cyclic Electrodeposition/Stripping, Thinning by Electrooxidation, and Electrical Power Generation, *Langmuir,* 2006. **22**: p. 10564-10574

[17] R. Venkatasubramanian, T. Colpitts, E. Watko, M. Lamvik and N. El-Masry, MOCVD of $Bi_2Te_3$, $Sb_2Te_3$ and their superlattice structures for thin-film thermoelectric applications, *Journal of Crystal Growth,* 1997. **170**: p. 817-821

[18] R. Venkatasubramanian, E. Siivola, T. Colpitts and B. O'Quinn, Thin-film thermoelectric devices with high room-temperature figures of merit, *Nature,* 2001. **413**: p. 597-602

[19] F. Xiao, B. Yoo, K. H. Lee and N. V. Myung, Synthesis of $Bi_2Te_3$ Nanotubes by Galvanic Displacement, *Journal of the American Chemical Society,* 2007. **129**: p. 10068-10069

[20] F. Xiao, B. Yoo, K.-H. Lee and N. V. Myung, Electro-transport studies of electrodeposited $(Bi_{1-x}Sb_x)_2Te_3$ nanowires, *Nanotechnology,* 2007. **18**: p. 335203

[21] B. Y. Yoo, C. K. Huang, J. R. Lim, J. Herman, M. A. Ryan, J. P. Fleurial and N. V. Myung, Electrochemically deposited thermoelectric n-type $Bi_2Te_3$ thin films, *Electrochimica Acta,* 2005. **50**: p. 4371-4377

[22] D. R. Lide, *CRC Handbook of Chemistry & Physics,* Cleveland, CRC Press, 2007-8.

[23] F. Xiao, B. Yoo, M. A. Ryan, K.-H. Lee and N. V. Myung, Electrodeposition of PbTe thin films from acidic nitrate baths, *Electrochimica Acta,* 2006. **52**: p. 1101-1107

[24] M. S. Martin-Gonzalez, A. L. Prieto, R. Gronsky, T. Sands and A. M. Stacy, Insights into the Electrodeposition of $Bi_2Te_3$, *Journal of The Electrochemical Society,* 2002. **149**: p. C546-C554

[25] Y. R. Chong Hyun Chang, Yong-Ho Choa, Deok-Yong Park, N.V. Myung, Galvanic displacement of $Bi_xTe_y$ thin films from sacrificial iron group thin films, *Electrochimica Acta,* 2009. **55**: p. 1072-1080

[26] J. O. Barnes, J. A. Rayne and R. W. Ure, Lattice parameters of n-and p-type $Bi_2Te_3$, *Physics Letters A,* 1973. **44**: p. 215-216

[27] S. Cho, Y. Kim, A. DiVenere, G. K. Wong, J. B. Ketterson and J. R. Meyer, Antisite defects of $Bi_2Te_3$ thin films, *Applied Physics Letters,* 1999. **75**: p. 1401-1403

[28] Y. Kim, S. Cho, A. DiVenere, G. K. L. Wong and J. B. Ketterson, Composition-dependent layered structure and transport properties in BiTe thin films, *Physical Review B,* 2001. **63**: p. 155306

[29] H. Baker, *ASM handbook,* Materials Park, ASM International, 2005.

[30] A. Emrani, G. Ghibaudo, F. Balestra, B. Piot, V. Thirion and A. Straboni, Low temperature electrical characterization of metal-nitrided oxide-silicon field effect transistors, *Journal of Applied Physics,* 1993. **73**: p. 5241-5253

[31] J. Zhou, C. Jin, J. H. Seol, X. Li and L. Shi, Thermoelectric properties of individual electrodeposited bismuth telluride nanowires, *Applied Physics Letters,* 2005. **87**: p. 133109-133109-3

[32] A. Mavrokefalos, A. L. Moore, M. T. Pettes, L. Shi, W. Wang and X. Li, Thermoelectric and structural characterizations of individual electrodeposited bismuth telluride nanowires, *Journal of Applied Physics,* 2009. **105**: p. 104318-8

[33] J. P. Fleurial, L. Gailliard, R. Triboulet, H. Scherrer and S. Scherrer, Thermal properties of high quality single crystals of bismuth telluride--Part I: Experimental characterization, *Journal of Physics and Chemistry of Solids,* 1988. **49**: p. 1237-1247

[34] C. B. Satterthwaite and R. W. Ure, Electrical and Thermal Properties of $Bi_2$ $Te_3$, *Physical Review,* 1957. **108**: p. 1164

[35] D. M. Rowe, *CRC Handbook of Thermoelectrics,* Boca Raton, CRC Press, Inc., 1995.

# CHAPTER 5

# Conclusions

The relentless advance of technologies has generated some serious issues pertaining to the energy crisis and pollution. Further advanced technologies are ironically required to solve the issues. In addition, the overwhelming data due to the rapid growth of computer and multimedia fields demand more advanced technologies. Recently, nanotechnology has shown the potential to find out the ultimate solution, because the ultra-small dimension of materials at the nano-scaled level have demonstrated unique and desirable properties. Especially, the development of the nanostructured chalcogenide materials is currently geared for the applications of thermoelectric and phase change memory devices with high performance.

The dissertation is based on the development of cost-effective and scalable fabrication techniques of the nanostructured chalcogenide materials. The dimension, size, composition, morphology as well as crystallinity of chalcogenide materials were controlled by various deposition parameters. The thermoelectric and phase transition properties depending on the tailored material properties were systematically investigated.

Chapter 1 begins with the fundamental backgrounds of thermoelectric and phase change memory including research trends, operating concepts, materials, device structure and state-of-the arts. The approaches to the enhancement of the device performance were conceived through the review of the extensive trial-and-errors and the remarkable breakthroughs.

Chapter 2 described the electrochemical analysis and thermoelectric characterization of 3-dimensional antimony telluride ($Sb_xTe_{1-x}$) electrodeposits. Various electroanaltyical techniques were utilized to determine the deposition mechanism of $Sb_xTe_{1-x}$ electrodeposits at different deposition conditions. The underpotential deposition of Sb at low cathodic potential (-0.17V to -0.3V (vs. Ag/AgCl)) was analyzed. The electrodeposition of Sb at more cathodic potential (< -0.3V (vs. Ag/AgCl)) was carried out by both underpotential and overpotential process. The current efficiency and partial current densities of elements were investigated depending on applied potential, agitation and temperature. Moreover, the morphologies and crystal structures of the electrodeposits were analyzed. Thermoelectric characterization was conducted with the $Sb_xTe_{1-x}$ electrodeposits on the thermally evaporated $Sb_2Te_3$ seed layers. Temperature dependent thermoelectric properties of $Sb_xTe_{1-x}$ electrodeposits with tailored morphology and composition were investigated. Improved thermoelectric properties were demonstrated in $Sb_xTe_{1-x}$ films with smooth and dense morphologies rather than films with nodular/granular morphologies. Phase transition properties from amorphism to polycrystallinity were corresponded with electrical properties in a thermal cycle for measurement. Significantly, the crystallinity of $Sb_xTe_{1-x}$ electrodeposits was controlled by annealing temperature. The $Sb_xTe_{1-x}$ electrodeposits annealed at 330 K and 351 K indicated a nanocomposite structure with inclusions of γ-SbTe phase in the $Sb_xTe_{1-x}$ matrix, and demonstrated drastically enhanced Seebeck coefficients.

In Chapter 3, 2-dimensional binary $Ag_xTe_{1-x}$ and ternary $Ag_xSb_{1-x}Te_y$ thin films were synthesized by topochemical reaction of Te and cation exchange reaction of SbTe,

respectively, as simple wet-chemical methods. The film compositions were controlled by the reaction time. The temperature-dependent electrical properties including the electrical resistivity, Seebeck coefficient and power factor of the prepared films were systematically measured for the thermal cycle of heating/cooling steps, where $Ag_xSb_{1-x}Te_y$ thin films showed a phase transition behavior in the heating steps. In topochemically transformed $Ag_xTe_{1-x}$ thin films, the composition-dependent thermoelectric properties demonstrated distinctive properties. The Seebeck coefficients of the films demonstrated the transition of the charge carrier type from the p-type Te and Te-rich $Ag_xTe_{1-x}$ thin films to the n-type Ag-rich $Ag_{64}Te_{36}$ thin film. In the cation exchanged $Ag_xSb_{1-x}Te_y$ thin films, the electrical conductivity and Seebeck coefficients decreased with the increase of Ag vacancies, and the $Ag_6Sb_{53}Te_{41}$ thin film with high Ag vacancies demonstrated a low transition temperature and high resistivity variation.

1-Dimensional chalcogenide nanostructures were fabricated in Chapter 4. Single crystalline PbTe nanowires with a preferred growth direction about 31° against [200] direction were synthesized by electrodeposition in acidic nitrate baths. Galvanic displacement reaction process was introduced to deposit gold nanoparticles on PbTe nanowires to minimize/eliminate contact resistance between PbTe nanowire and electrodes. Electron-transport properties of these nanowires indicated that the electrodeposited PbTe nanowire is low doped p-type semiconductor with excellent field effect mobility. Additionally, single tellurium nanoribbon based nano-devices with well-controlled geometries and dimensions were fabricated by the LPNE technique. The electrical properties of the fabricated single tellurium nanoribbon based devices showed

decreased amount of defects in Te nanoribbons with the reduced dimensions, based on the variation of FET mobility. The sensor performance was demonstrated as a function of the width of Te nanoribbons. The enhanced sensitivity with the decreased width can be attributed to reduction of the conducting channel and the improved conductivity of Te nanoribbon. Furthermore, measurement of sensing properties versus electrical contact types demonstrated that single Te nanoribbon based sensor devices with Schottky contact displayed enhanced sensitivity over the devices with ohmic contact. The annealing effects of Te nanoribbon on sensing properties were investigated by the comparison of sensitivity on $NO_x$ (g) before and after annealing process. Despite the change of contact type from Schottky to ohmic contact, the sensitivity of the annealed Te nanoribbon was enhanced by the improved crystallinity of Te nanoribbons. Finally, aligned $Bi_xTe_y$ nanoribbons with tailored dimension and composition were synthesized by the LPGD technique. Composition dependent electrical resistivity showed two distinct regions, where $Bi_xTe_y$ nanoribbons with Te content between 62 and 72 at.% show the increased electrical resistivity with increase in Te content, and where excess Te may increase carrier concentration to reduce electrical resistivity. When the composition of $Bi_xTe_y$ nanoribbons deviated greatly from the stoichiometric $Bi_2Te_3$ compound ( >72 at.%) crystalline defects and a porous microstructure play a more critical role than dopant level, which resulted in increased electrical resistivity with increase in Te content.

# APPENDIX

# Antimony Telluride Nanoribbons by Lithographically Patterned Nanowires Electrodeposition

## A.1 Abstract

In addition to the fabrication of n-type $Bi_xTe_{1-x}$ nanoribbons, the aligned $Sb_xTe_{1-x}$ nanoribbons as a p-type 1-dimensional nanostructure were fabricated by a LPNE technique. Based on the previous electrochemical study of $Sb_xTe_{1-x}$ electrodeposits, the composition of $Sb_xTe_{1-x}$ nanoribbons was controlled by varying the applied potential. Composition-dependent electrical properties were mainly dependent on the poor morphologies and increased defects due to deviation from stoichiometry, which is similar with the report of $Bi_xTe_{1-x}$ nanoribbons. The improvement of morphology and the reduction of size of the nanoribbons were confined. Cetyl trimethyl ammonium bromide (CTAB) as a cationic surfactant was added to improve the morphology and a pulse plating technique was utilized to reduce the size of electrodeposited $Sb_xTe_{1-x}$ nanoribbons. Size-dependent electrical properties of $Sb_xTe_{1-x}$ nanoribbons were investigated.

## A.2 Experimental

$Sb_xTe_{1-x}$ nanoribbons were fabricated by typical LPNE procedure as previous chapters. Sacrificial nickel layers with thickness of 50nm and 100nm were deposited by e-beam evaporator. $Sb_xTe_{1-x}$ nanoribbons were electrodeposited at the applied potential from -0.12V to -0.4V (vs. SCE) in the electrolyte of 0.01M $TeO_2$, 0.02M $Sb_2O_3$, 0.5M L-

tartaric acid and 1M $HNO_3$. 0.001M Cetyl trimethyl ammonium bromide (CTAB) as a cationic surfactant was added to improve the morphology. And, a pulse plating technique was employed with a potential of -0.15 V (vs. SCE) with duty cycle of 0.083 ($T_{on}$ of 10 ms and $T_{off}$ of 110 ms) to fabricate $Sb_xTe_{1-x}$ nanoribbons with the reduced size without chops.

Electrical resistivity and field effect transistor (FET) properties of single $Sb_xTe_{1-x}$ nanoribbon with different composition and widths were measured with source meter (Kiethley, 2636A) in the gate voltage ($V_G$) being swept from -20 V to 20 V at a fixed drain-source voltage ($V_{DS}$) of 0.1 V, and the I-V curves being characterized at different $V_G$ ranging from -20 V to 20 V. Temperature dependent electron transport properties were measured by an custom-made cryogenic system linked with a temperature controller (Lakeshore, 331) and source-meter (Kiethley, 2636A).The morphologies of Te nanoribbons were analyzed by scanning electron microscope (SEM) (XL30-FEG, Phillips).

## A.3 Composition-dependent electrical properties of the potentiostatically deposited $Sb_xTe_{1-x}$ nanoribbons

Figure A.1 shows SEM images of $Sb_xTe_{1-x}$ nanoribbons with different compositions. The nanoribbons have the height of 100 nm which was determined by the thickness of a sacrificial nickel layer. Even though the width of nanoribbons was controlled by deposition time, the nanoribbons with the width of less than 100 nm were discontinuous. The length of the nanoribbons was determined by a lithographical pattern.

The composition of $Sb_xTe_{1-x}$ nanoribbons was controlled by the applied potentials ranging from -0.12V to -0.4V (vs. SCE). The composition-dependent electrical resistivity was shown in Figure A.2. As Te content of $Sb_xTe_{1-x}$ increased, the resistivity of nanoribbons increased. The increase of electrical resistivity may be attributed to the rough morphologies and the increased defects due to excess Te. FET properties of $Sb_xTe_{1-x}$ nanoribbons in Figure A.3 described a typical p-type semiconducting behavior and confirmed the increased defects in the nanoribbons with excess Te. The deposited $Sb_xTe_{1-x}$ nanoribbons were annealed at 473K for 6 hour in 5 % $H_2/N_2$ (g). The annealed nanoribbons demonstrated reduced resistivity and enhanced FET mobility (Figure A.4). Temperature-dependent electrical resistivity and FET mobility of Sb41Te59 nanoribbons with the thickness of 900 nm was described in Figure A.5, which indicated the hopping transport of carriers.

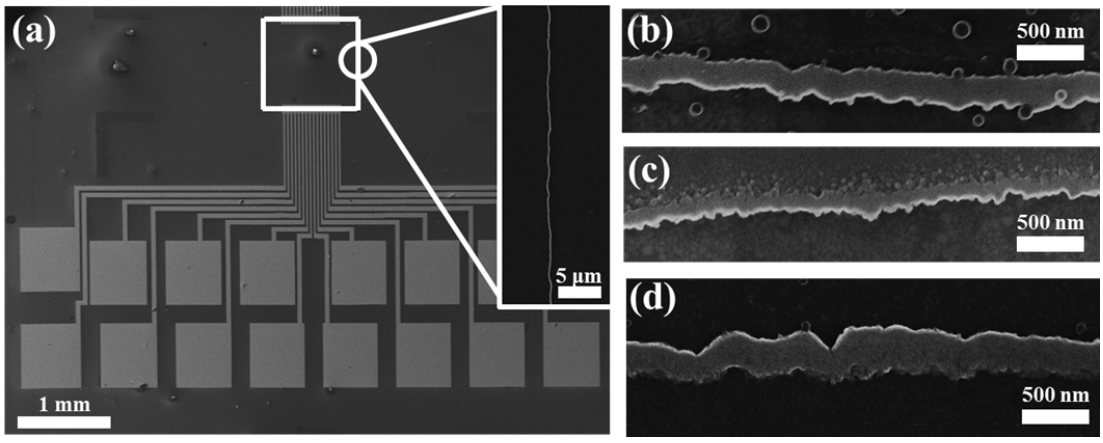


**Figure A.1**: SEM images of SbxTe1-x nanoribbons: Patterned Au electrodes on $Sb_xTe_{1-x}$ nanoribbon (inset: magnified image) (a), $Sb_{46}Te_{54}$ deposited at -0.15 V (vs. SCE) (b), $Sb_{60}Te_{40}$ deposited at -0.2 V (vs. SCE) (c) and $Sb_{72}Te_{28}$ deposited at -0.25 V (vs. SCE) (d).

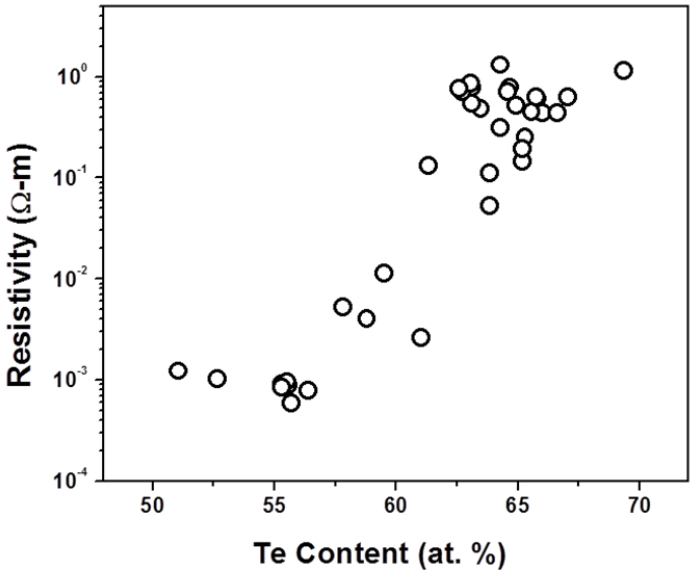


**Figure A.2**: Composition-dependent electrical resistivity of $Sb_xTe_{1-x}$ nanoribbons with the width of 700 ± 220 nm

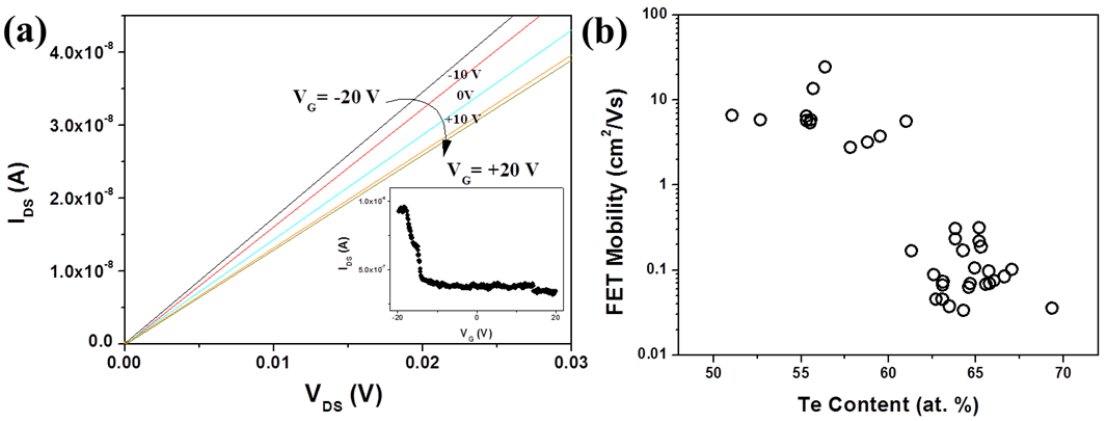


**Figure A.3**: Back-gated FET properties of $Sb_xTe_{1-x}$ nanoribbons: $I_{DS}$ vs. $V_{DS}$ of a $Sb_{45}Te_{55}$ nanoribbon with a width of 900 nm (inset: $I_{DS}$ vs. $V_G$ at the fixed $V_{DS}$ of +0.1 V) (a) and composition-dependent FET mobility of $Sb_xTe_{1-x}$ nanoribbons (b)

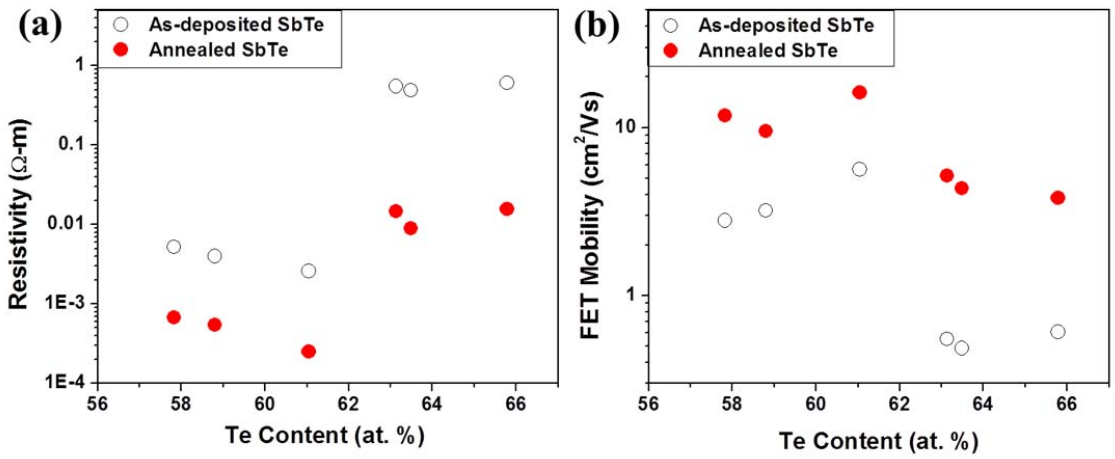


**Figure A.4**: Annealing effects on the electrical properties of $Sb_xTe_{1-x}$ nanoribbons with different compositions. The nanoribbons were annealed at 474K for 6 hour in 5% $H_2/N_2$ (g): electrical resistivity (a) and FET mobility (b)

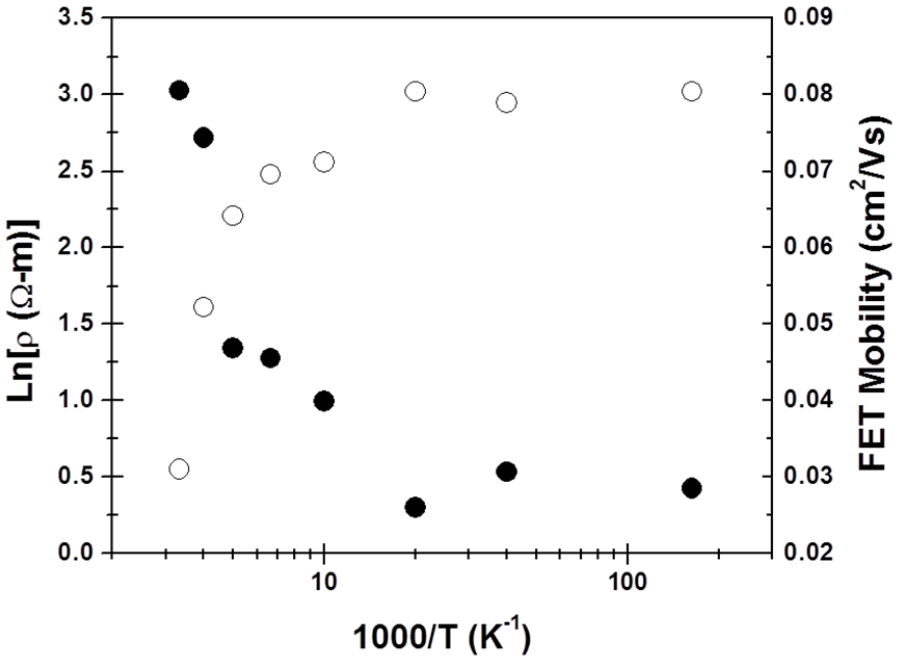


**Figure A.5**: Temperature-dependent electrical properties of Sb41Te59 nanoribbons with the thickness of 900 nm.

## A.4 Effects of a surfactant on the morphologies of the electrodeposited $Sb_xTe_{1-x}$ nanoribbons

Cetyl trimethyl ammonium bromide (CTAB) is a typical cationic surfactant. CTAB has shown the strong adsorbed ability for colloidal synthesis of Au rods. Moreover, CTAB has been used as a corrosion inhibitor and has decreased the adhesion of hydrogen bubbles in the electrodeposition. CTAB was added to improve the morphology of $Sb_xTe_{1-x}$ nanoribbons. Figure A.6 described a linear sweep voltammetry before and after addition of 0.001M CTAB in the electrolyte of 0.01M $TeO_2$, 0.02M $Sb_2O_3$, 0.5M L-tartaric acid and 1M $HNO_3$. The reduction potential was shifted to -0.05V and the current density was increased after addition of CTAB. $Sb_xTe_{1-x}$ thin film was electrodeposited at -0.17V (vs. SCE) on e-beam evaporated Au layers to investigate the effects of CTAB on their morphology. The morphologies of $Sb_{43}Te_{57}$ thin films and nanoribbons were compared after the addition of CTAB (Figure A.7). Addition of CTAB surfactants demonstrated the dense and smooth morphologies of the $Sb_{43}Te_{57}$ film/nanoribbon, compared to the rough and nodular/granular morphologies of the film/nanoribbon electrodeposited without CTAB. The resistivity of $Sb_{43}Te_{57}$ nanoribbons was decreased from $5.25 \times 10^{-3}$ Ωm to $8.89 \times 10^{-4}$ Ωm after the addition of CTAB.

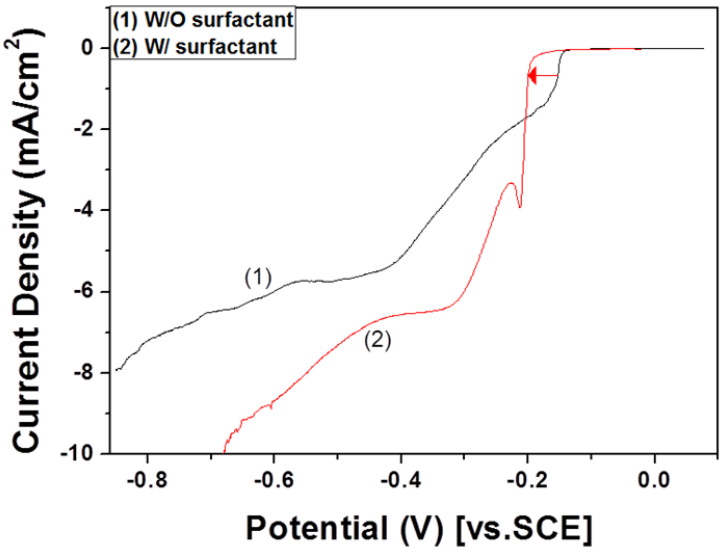


**Figure A.6**: Linear sweep voltammetry with scan rate of 1mV/sec: 0.01M $TeO_2$, 0.02M $Sb_2O_3$, 0.5M L-tartaric acid and 1M $HNO_3$ (1) and 0.01M $TeO_2$, 0.02M $Sb_2O_3$, 0.5M L-tartaric acid, 1M $HNO_3$ and 0.001M CTAB (2)

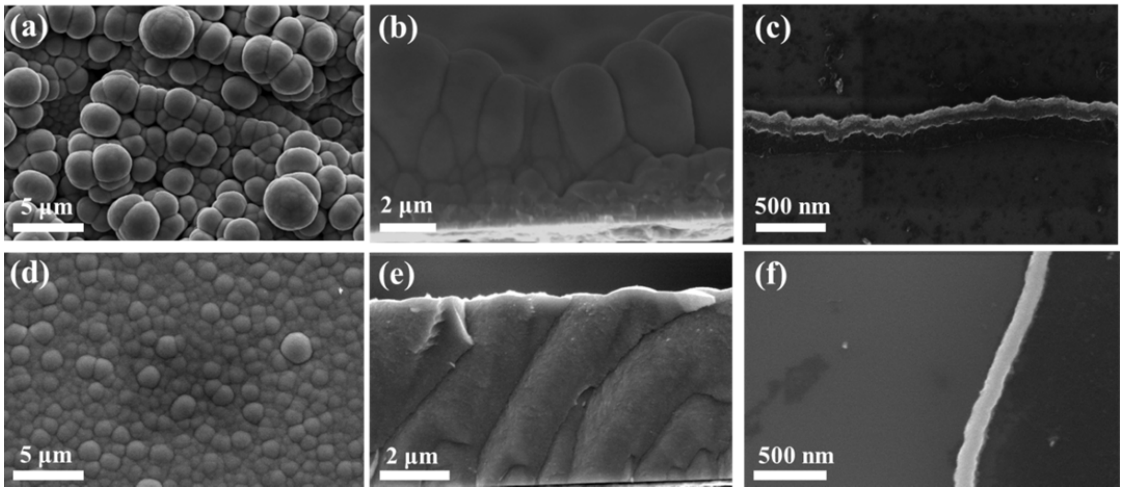


Figure A.7: SEM images of $Sb_{43}Te_{57}$ electrodeposited in the electrolyte without CTAB and with CTAB: top-view (a), cross-sectional view (b) of a thin film and a nanoribbon (c) electrodeposited without CTAB, and top-view (d), cross-sectional view (e) of a thin film and a nanoribbon (f) electrodeposited with CTAB.

## A.5 Size reduction of $Sb_xTe_{1-x}$ nanoribbons electrodeposited by a pulse plating technique

The width of $Sb_xTe_{1-x}$ nanoribbons fabricated by a potentiostatic deposition technique was limited to minimum 100 nm. The size reduction of $Sb_xTe_{1-x}$ nanoribbons can be achieved by applying a pulse plating technique, because the pulsed potentials can improve the nucleation rate. The $Sb_{43}Te_{57}$ nanoribbons were electrodeposited at a potential of -0.15 V (vs. SCE) with duty cycle of 0.083 ($T_{on}$ of 10 ms and $T_{off}$ of 110 ms) on the sacrificial nickel layer of 50 nm thickness. Figure A.8 described the morphologies of $Sb_{43}Te_{57}$ nanoribbons with different width tailored by deposition times. Additionally, the size-dependent electrical properties of $Sb_{43}Te_{57}$ nanoribbons were shown in Figure A.9. The increased surface boundary scattering in the nanoribbons with smaller size showed the increased resistivity.

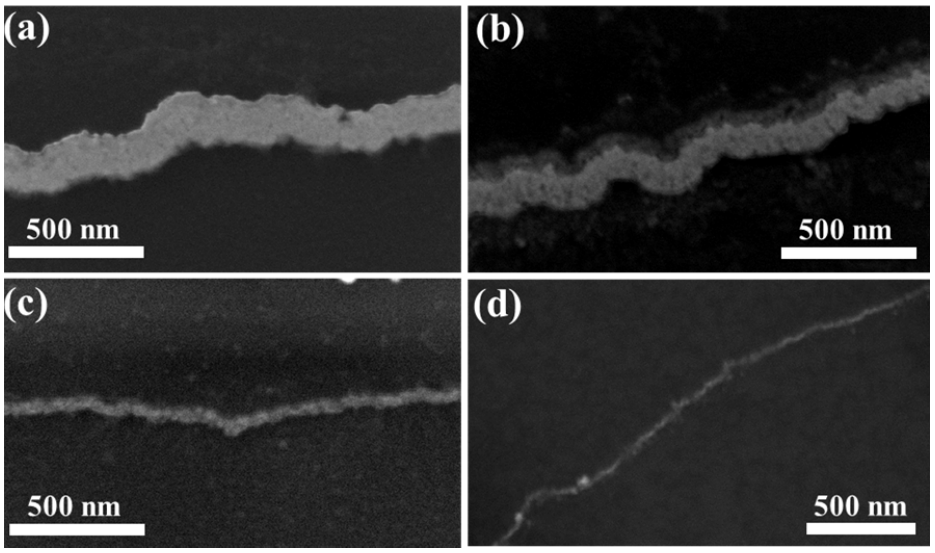


**Figure A.8**: Pulse plated $Sb_{43}Te_{57}$ nanoribbons at different deposition times: 30 sec (a), 10 sec (b), 5 sec (c) and 3sec (d).

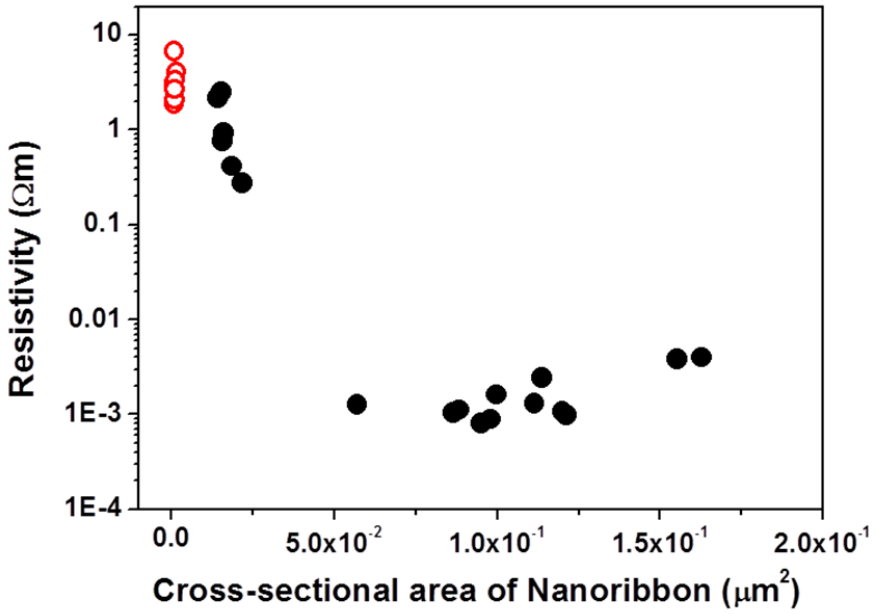


**Figure A.9**: Size-dependent electrical resistivity of $Sb_{43}Te_{57}$ nanoribbons; the nanoribbons with the width of less than 100 nm were pulse plated (red open circles).